Nanocomposites of Carbon Nanosphere and Graphene Oxide with Iron Oxide as High-Performance Adsorbents for Arsenic Removal

By

Hui Su

A thesis submitted in partial fulfillment
of the requirements for the degree of
Master of Applied Science (MASc)
in Natural Resources Engineering

The Faculty of Graduate Studies
Laurentian University
Sudbury, Ontario, Canada

THESIS DEFENCE COMMITTEE/COMITÉ DE SOUTENANCE DE THÈSE
Laurentian Université/Université Laurentienne

Faculty of Graduate Studies/Faculté des études supérieures

Title of Thesis
Titre de la thèse Nanocomposites of Carbon Nanosphere and Graphene Oxide with Iron Oxide as High-Performance Adsorbents for Arsenic Removal

Name of Candidate
Nom du candidat Su, Hui

Degree
Diplôme Master of Applied Science

Department/Program
Département/Programme Natural Resources Engineering

Date of Defence
Date de la soutenance November 17th, 2016

APPROVED/APPROUVÉ

Thesis Examiners/Examinateurs de thèse:

Dr. Zhibin Ye
(Supervisor/Directeur de thèse)

Dr. Ramesh Subramanian
(Committee member/Membre du comité)

Dr. Brahim Chebbi
(Committee member/Membre du comité)

Dr. Mladen Eic
(External Examiner/Examinateur externe)

Approved for the Faculty of Graduate Studies
Approuvé pour la Faculté des études supérieures
Dr. David Lesbarrères
M. David Lesbarrères
Acting Dean, Faculty of Graduate Studies
Doyen intérimaire, Faculté des etudes supérieures

ACCESSIBILITY CLAUSE AND PERMISSION TO USE

ABSTRACT

Arsenic is a widely distributed element in the Earth's crust with an average terrestrial concentration of about 5 g ton^{-1}. Arsenic is a persistent, bio-accumulative, toxic element. The United States Environmental Protection Agency (EPA) has implemented the discharge criterion of 10 μg L^{-1} for arsenic as the maximum acceptable level for ground water. During the past decades, several techniques have been developed for the removal of arsenic from the wastewater, including chemical precipitation, adsorption and ion exchange, membrane and biological removal processes, and so on. Because of the good arsenic removal efficiency and the low cost, adsorption is a more popular method. In this thesis research, two ranges of iron oxide nanocomposite adsorbents have been developed and studied for their performance properties towards arsenic removal.

Novel iron oxide encapsulated carbon nanospheres (FeO_x-CNS) with excellent arsenic adsorption performance has been successfully synthesized. CO_2 activated carbon nanospheres material (A-CNS) with high surface area (2271 m^2 g^{-1}) and high pore volume (5.18 cm^3 g^{-1}) was selected as the porous matrix. After surface oxidation by ammonium persulfate (APS), iron oxide was loaded into the carbon nanospheres as the effective arsenic adsorbent. Transmission electron microscopy (TEM) and Braunauer–Emmett–Teller (BET) results indicate that iron oxide nanoparticles (7−60 wt%) are well-dispersed within the mesopores. In particular, FeO_x-CNS-13 composite shows most optimum

performance properties, with high arsenic adsorption capacities achieved for both As(III) (416 mg g^{-1}) and As(V) (201 mg g^{-1}).

Another range of amorphous iron oxide-graphene oxide (FeO_x-GO) nanocomposites having different graphene oxide (GO) content (36-80 wt%) was prepared by coprecipitation of ferrous sulfate heptahydrate and ferric sulfate hydrate on GO sheets. The composites have been thoroughly characterized and investigated for their performance towards arsenic removal. The optimum composite, FeO_x-GO-80 having the highest iron oxide content of 80 wt% shows excellent arsenic adsorption capacities for both As(III) (147 mg g^{-1}) and As(V) (113 mg g^{-1}), which are highest among iron oxide-GO composites reported to date for arsenic removal. The high performance along with low cost and convenience in synthesis makes this range of amorphous iron oxide-GO nanocomposites promising for applications.

Keywords: carbon nanosphere, arsenic removal, iron oxide, CO_2 activation, graphene oxide, arsenic adsorption.

ACKNOWLEDGEMENTS

First and foremost, I would like to offer my sincerest gratitude to my supervisor, Dr. Zhibin Ye for his ever-present guidance, patience, knowledge, and encouragement throughout my thesis.

I would like to thank external examiner Dr. Mladen Eic, committee Dr. Ramesh Subramanian and Dr. Brahim Chebbi for reviewing my thesis and providing me with their expert knowledge, which helped me greatly.

I would like to thank GoldCorp Red Lake Gold Mines for the funding and supply of wastewater samples.

I would also like to thank my group mates Linqi Huang, Zhe Chen, Junbin Liao, Mark Grundy, Peng Xiang and Zhongmin Dong, who provided both friendship and expertise during my research.

Lastly, and most importantly, I would like to thank my family for their constant love and support in my entire life. Without their support and guidance, I would not have been able to achieve so much as I have so far.

Table of Contents

THESIS DEFENCE COMMITTEE/COMITÉ DE SOUTENANCE DE THÈSE·····ii

ABSTRACT·····iii

ACKNOWLEDGEMENTS·····v

Table of Contents·····vi

List of Schemes and Figures·····x

List of Tables·····xvii

Chapter 1: Introduction·····1

1.1 Background·····1

1.2 Arsenic removal methods·····3

1.2.1 Chemical precipitation method·····4

1.2.2 New arsenic removal processes classification·····7

1.2.3 Adsorption method·····8

1.2.3.1 Arsenic adsorption by iron oxide ·····9

1.2.3.2 Arsenic adsorption by Fe/metal binary oxides·····16

1.2.3.3 Arsenic adsorption by Fe/Organic composites……18

1.2.3.4 Arsenic adsorption by Fe/Carbon composites……19

1.2.3.4.1 Arsenic adsorption by Fe/Graphene composites……19

1.2.3.4.2 Arsenic adsorption by Fe/ porous carbon composites……22

1.2.3.5 Arsenic adsorption by Fe/Silica composites……35

1.3 Summary……37

1.4 Objective and Organization of Thesis……38

1.5 References……39

Chapter 2: Carbon Nanosphere-Iron Oxide Nanocomposites as High-Capacity Adsorbents for Arsenic Removal ……43

2.1 Introduction……45

2.2 Experimental Section……46

2.2.1 Materials……46

2.2.2 Synthesis of carbon nanospheres (CNS) and CO_2 activated carbon nanospheres (A-CNS) ……47

2.2.3 Synthesis of iron oxide-CNS composites (FeO_x-CNS) ……51

2.2.4 Characterizations and Measurements……52

2.2.5 Arsenic Adsorption……54

2.3 Results and Discussion·····55

2.3.1 Synthesis and Characterization of Carbon Nanosphere Matrix·····55

2.3.2 Synthesis and Characterization of FeO_x-CNS Nanocomposites·····62

2.3.3 Arsenic Adsorption with FeO_x-CNS Composites ·····69

2.4 Conclusion·····77

2.5 References·····78

2.6 Supporting Information·····83

Chapter 3: Porous Iron Oxide-Graphene Oxide Composites with Excellent Arsenic Removal Performance·····91

3.1 Introduction·····92

3.2 Experimental Section·····95

3.2.1 Materials·····95

3.2.2 Synthesis of graphene oxide (GO) ·····96

3.2.3 Preparation of amorphous iron oxide-GO nanocomposites (FeO_x-GOs) ·····97

3.2.4 Characterizations and Measurements·····98

3.2.5 Arsenic Adsorption·····99

3.3 Results and Discussion·····101

3.3.1 Synthesis and Characterization of FeO_x-GOs Nanocomposites ……101

3.3.2 Arsenic adsorption with FeO_x-GO Nanocomposites……116

3.4 Conclusion……124

3.5 References……125

3.6 Supporting Information……130

Chapter 4: Conclusions and Outlooks……136

List of Schemes and Figures

Figure 1.1. Eh-pH diagram for aqueous As species in the system As-O_2-H_2O at 25 ^oC and 1 bar total pressure (adapted from ref. 2) ……2

Figure 1.2. Dissociation of As(V) (adapted from ref. 3) ……2

Figure 1.3.Wastewater treatment system flow sheet (adapted from ref. 4) ……5

Figure 1.4. Arsenic removal processes (adapted from ref. 5) ……7

Figure 1.5. Schematic for arsenic removal using adsorbent media (adapted from ref. 5) ……8

Figure 1.6. A schematic of an oleic acid coated magnetite NC (adapted from ref. 6) ……10

Figure 1.7. Arsenic adsorption studies with nanocrystalline (12 nm) and commercially available (20 and 300 nm) Fe_3O_4. (A) As(V) adsorption; (B) As(III) adsorption (adapted from ref. 6) ……10

Figure 1.8. A schematic illustration of the formation process of the Fe_2O_3 CAHNs: (1) the formation of iron by decomposing $Fe(CO)_5$; (2) oxidation of iron into amorphous iron oxide nanoparticles; (3) aggregation of iron oxide nanoparticles into a porous sphere; (4) tip-growth of maghemite nanorods on the surface of the amorphous iron oxide sphere and finally (5) the growth into Fe_2O_3 CAHNs (adapted from ref. 7) ……11

Figure 1.9. The equilibrium isotherm data of As(V) adsorption at pH 4 and room temperature, as well as the non-linear isotherm analysis using both the Langmuir and Freundlich adsorption equations (adapted from ref. 7) …… ……12

Figure 1.10. Adsorption isotherms of As(V) and Cr (VI) using flowerlike α-Fe_2O_3 nanostructures (adapted from ref. 8) ……13

Figure 1.11. Schematic illustration of the formation mechanism of a hollow nestlike α-Fe_2O_3 nanostructure (adapted from ref. 9) ……13

Figure 1.12. Adsorption isotherms of As(V) and Cr (VI) using the hollow nestlike α-Fe_2O_3 nanostructures (adapted from ref. 9) ……14

Figure 1.13. Flame synthesis set-up. The magnified area shows different phases of iron oxide nanoparticles formation in different flame heights (adapted from ref. 10) ….15

Figure 1.14. Room temperature equilibrium isotherm data of As(V) adsorption on the γ-Fe_2O_3 nanochains at pH 7 (adapted from ref. 10) ……16

Figure 1.15. Adsorption isotherms of (a) As(V) fitted by the Langmuir model and (b) As(III) by the Freundlich model, respectively, on IA and NH-ICAs. The initial arsenic concentration ranged from 1 to 100 mg L^{-1}. The dosage of adsorbents and the initial pH value were 0.2 g L^{-1} and 6, respectively. NH-ICA08, NH-ICA05, NH-ICA03, and NH-ICA01, respectively, corresponding to the molar ratio (adapted from ref. 15) ……18

Figure 1.16. Scheme showing the reaction steps for preparation of a graphene/iron oxide hybrid where the two components are linked via hydroxyl groups (adapted from ref. 20) ……20

Figure 1.17. Synthesis and application of Fe_3O_4-RGO composites (adapted from ref. 21) ……21

Figure 1.18. Adsorption isotherms of As(III) and As(V) on the Fe_3O_4-RGO composite (temperature 20 °C, pH 7) (adapted from ref. 21) ……21

Figure 1.19. Schematic preparation process of microporous monodisperse carbon nanospheres (adapted from ref. 24) ·····24

Figure 1.20. A schematic diagram showing the preparation of microporous carbon particles via selective pyrolysis of PS-PMMA spheres (adapted from ref. 25) ·····25

Figure 1.21. Schematic illustrations of preparing mesostructured meso-Fe/C composites via direct synthesis approach. (adapted from ref. 27) ····· ·····26

Figure 1.22. Schematic illustrations of preparing mesostructured meso-Fe/C composites via post loading method. (adapted from ref. 28) ·····27

Figure 1.23. Illustration of the synthesis and arsenic capture processes for the ordered mesoporous Fe_2O_3@C encapsulates. (adapted from ref. 29) ·····28

Figure 1.24. Adsorption isotherms at 25 °C (A) of As(III) (a–c) and As(V) (d–f) on the mesoporous carbon matrix (a, d), encapsulates Fe_2O_3@C-300 (c, f), and Fe_2O_3@C-500 (b, e). Time-dependent capture of As(III) (B) by the mesoporous encapsulates Fe_2O_3@C-500 with a sorbent loading of 1 mg mL^{-1} and an initial arsenic concentration of 5 (g, h) and 25 mg L^{-1} (i, j) (adapted from ref. 29)···· ·····30

Figure 1.25. Arsenic adsorption of MI/CNTs (adapted from ref. 30) ·····31

Figure 1.26. Schematic representation of the preparation of CF-CNTs via a surfactant assisted method (adapted from ref. 33) ·····32

Figure 1.27. Adsorption isotherms of As(V) (a) and As(III) (b) on CF-CNTs at 298 K. The initial concentration ranged from 1 to 20 mg L^{-1}, the dosage of adsorbents was 0.2 g L^{-1}, and the initial pH values for the solutions were 4 and 7.5 for As(V) and As(III), respectively (adapted from ref. 33)·· ·····33

Figure 1.28. The scheme of the preparation of Fe_3O_4/CAs and Fe/CAs mesoporous structures using hydrothermal process (adapted from ref. 34) ·····34

Figure 1.29. Plot of the arsenic adsorption capacity versus the arsenic equilibrium concentration (adapted from ref. 34) ····· ·····34

Figure 1.30. a) As(V) and b) As(III) adsorption isotherms of FexMOSF composites (adapted from ref. 36) ·····36

Scheme 2.1. Schematic synthesis of carbon nanosphere matrix and the FeO_x-CNS nanocomposites·····56

Figure 2.1. TEM of CNS (a), A-CNS (b), and S-CNS (c) ·····57

Figure 2.2. (a) N_2 sorption isotherm of CNS, A-CNS and S-CNS, (b) N_2 sorption isotherm of FeO_x-CNS-13, FeO_x-CNS-28 and FeO_x-CNS-60·····58

Figure 2.3. FTIR spectra of CNS, A-CNS, S-CNS, FeO_x-CNS-13, FeO_x-CNS-28, and FeO_x-CNS-60 ·····62

Figure 2.4. TGA curves of CNS, A-CNS, S-CNS, and FeO_x-CNS composites in air·····63

Figure 2.5. XRD patterns of A-CNS, S-CNS, FeO_x-CNS-13, and FeO_x-CNS-60·····66

Figure 2.6. TEM (a), HRTEM images (b), DF-STEM image (c) and the corresponding C (d) O (e) and Fe (f) elemental maps of FeO_x-CNS-13·····68

Figure 2.7. (a) As(III) adsorption isotherms (at pH = 8) and (b) As(V) adsorption isotherms (at pH = 3) of A-CNS, S-CNS, and FeO_x-CNS composites. The adsorption isotherms are fitted the Freundlich adsorption model (solid line)·····70

Figure 2.8. (a) As(III) and As(V) adsorption kinetic curves of FeO_x-CNS-13; (b) fitting of the kinetic data with the pseudo-second-order model·····75

Figure 2.9. Arsenic uptake of FeO_x-CNS-13 as a function of pH. The initial arsenic concentration is 1,000 mg L^{-1}·····76

Figure S2.1. Size distribution (average size: 27 nm; PDI: 0.19) of poly(DEB) polymer nanospheres obtained by miniemulsion polymerization by DLS measurement·····83

Figure S2.2. Mesopore/macropore size distributions (obtained by DFT model) of (a) CNS, A-CNS, and S-CNS; (b) three FeO_x-CNS composites ……84

Figure S2.3. (a) XPS survey scan of CNS, A-CNS, S-CNS, and FeO_x-CNS-28; (b) The content of C, O, and Fe in CNS, A-CNS, S-CNS, and FeO_x-CNS-28 determined by XPS; (c) high-resolution Fe_{2p} spectra of FeO_x-CNS-28……85

Figure S2.4. The O_{1s} (a) and C_{1s} (b) spectra of CNS, A-CNS, S-CNS and FeO_x-CNS-28 ……86

Figure S2.5. TEM (a), HRTEM images (b), DF-STEM image (c) and the corresponding C (d) O (e) and Fe (f) elemental maps of FeO_x-CNS-60……87

Figure S2.6. (a) Zeta potential of FeO_x-CNS-13 as a function of pH, and (b) the concentration of leached Fe in the equilibrium solution as a function of pH, where the initial arsenic concentration is 1,000 mg L^{-1}……90

Scheme 3.1. Schematic synthesis of FeO_x-GOs nanocomposites……103

Figure 3.1. TGA curves (a) and differential curves (b) for GO, FeO_x-GO-36, FeO_x-GO-60, FeO_x-GO-80 and iron oxide control sample in the air atmosphere……105

Figure 3.2. TEM and high-resolution TEM images of GO (a and b), FeO_x-GO-36 (c and d), FeO_x-GO-80 (e and f), and the iron oxide control sample (g and h) …… 106

Figure 3.3. FTIR spectra of GO, FeO_x-GO composites, and the iron oxide control sample ……108

Figure 3.4. (a) XPS survey scan of GO, FeO_x-GO-36, FeO_x-GO-80, and the iron oxide control sample, (b) the content of C, O, and Fe in the samples measured by XPS, (c)–(e) Fe_{2p} spectra in FeO_x-GO-36, FeO_x-GO-80, and the iron oxide control sample, respectively ……109

Figure 3.5. Wide-angle XRD patterns of GO, FeO_x-GO-80, and the iron oxide control sample……111

Figure 3.6. (a) N_2 adsorption-desorption isotherm of FeO_x-GO composites, GO, and the iron oxide control sample, (b) DFT meso-/macro-pore size distribution curves, (c) dependencies of surface area and pore volume data on the iron oxide content……113

Figure 3.7. (a) As(III) adsorption isotherms (at pH = 7) and (b) As(V) adsorption isotherms (at pH = 3) of FeO_x-GO nanocomposites, GO, and the iron oxide control sample. All the isotherms are well fitted with the Langmuir model (solid line) ……117

Figure 3.8. (a) As(III) and As(V) adsorption kinetic curves with FeO_x-GO-80 (initial arsenic concentration of 400 and 350 mg L^{-1} for As(III) (pH = 7) and As(V) (pH = 3), respectively; (b) fitting of the kinetic curves with the pseudo-second-order model ……121

Figure 3.9. (a) Arsenic uptake of FeO_x-GO-80 as a function of pH (initial arsenic concentration of 350 mg L^{-1}); (b) Zeta potential of FeO_x-GO-80 as a function of pH ……123

Figure S3.1. (a) AFM height image of GO, (b) height profiles across three profiles denoted in (a) ……130

Figure S3.2. The C_{1s} (a) and O_{1s} (b) scan results of GO, FeO_x-GO-36, FeO_x-GO-80 and the iron oxide control sample……131

Figure S3.3. DF-STEM image (a) and the corresponding C (b), O (c), and Fe (d) elemental maps of FeO_x-GO-80……132

Figure S3.4. DF-STEM image (a) and the corresponding C (b), O (c), and Fe (d) elemental maps of FeO_x-GO-36……133

Figure S3.5. Arsenic adsorption with FeO_x-GO-80 at different dosages (0.1–1 mg mL^{-1}). Initial arsenic concentration: 1200 and 350 mg L^{-1} for As(III) (at pH = 7) and As(V) (at pH = 3), respectively····· 134

List of Tables

Table 1.1. Summary of arsenic removal processes (adapted from ref. 1) ……3

Table 1.2. Summary of arsenic removal processes (adapted from ref. 3) ……4

Table 1.3. Comparison of arsenic adsorption capacities……37

Table 2.1. Results from N_2 sorption characterization……60

Table 2.2. Comparison of arsenic adsorption capacity data of representative iron oxide-based adsorbents ……73

Table S2.1. A summary of the fitted parameters of the arsenic adsorption isotherms and kinetics…… 88

Table S2.2. Summary of arsenic adsorption capacity data……89

Table 3.1. Results from N_2 sorption characterization……114

Table 3.2. Comparison of maximum arsenic adsorption capacities achieved with iron oxide-GO/RGO nanocomposites ……119

Table S3.1. A summary of the fitting parameters of arsenic adsorption isotherms and kinetics with FeO_x-GOs, GO, and the iron oxide control……135

Chapter 1: Introduction

1.1 Background

Arsenic is an abundant element in the Earth's crust with an average terrestrial concentration of about 5 g ton^{-1}. Arsenic is a persistent, bio-accumulative, toxic element. Arsenic is toxic because of its affinity for proteins, lipids and other cellular components. Many adverse health effects, such as several cancers, cardiovascular and neurological effects, have been attributed to chronic exposure to high levels of arsenic, primarily in drinking water. The United States Environmental Protection Agency (EPA) has implemented the discharge standard of 10 µg L^{-1} for arsenic as the maximum acceptable level for ground water. [1]

As shown in Figure 1.1 and Figure 1.2, arsenic in the environment can exist in multiple oxidation states (−3, +3, and +5). In natural waters, it is found mainly as the oxy-anionic trivalent arsenic [(III), arsenite] and pentavalent arsenic [(V), arsenate] species. Speciation of arsenic in water can be estimated by the pH and zeta potential. Species such as $H_3As(III)O_3$ and $H_3As(V)O_4$ predominate in the reduced conditions and oxidized conditions, respectively. In normal pH of natural waters (6 to 8), arsenate is found in two

anionic forms with negative charges: $H_2AsO_4^-$ and $HAsO_4^{2-}$, while arsenite is found in the only abundant form of H_3AsO_3 without charges.[2]

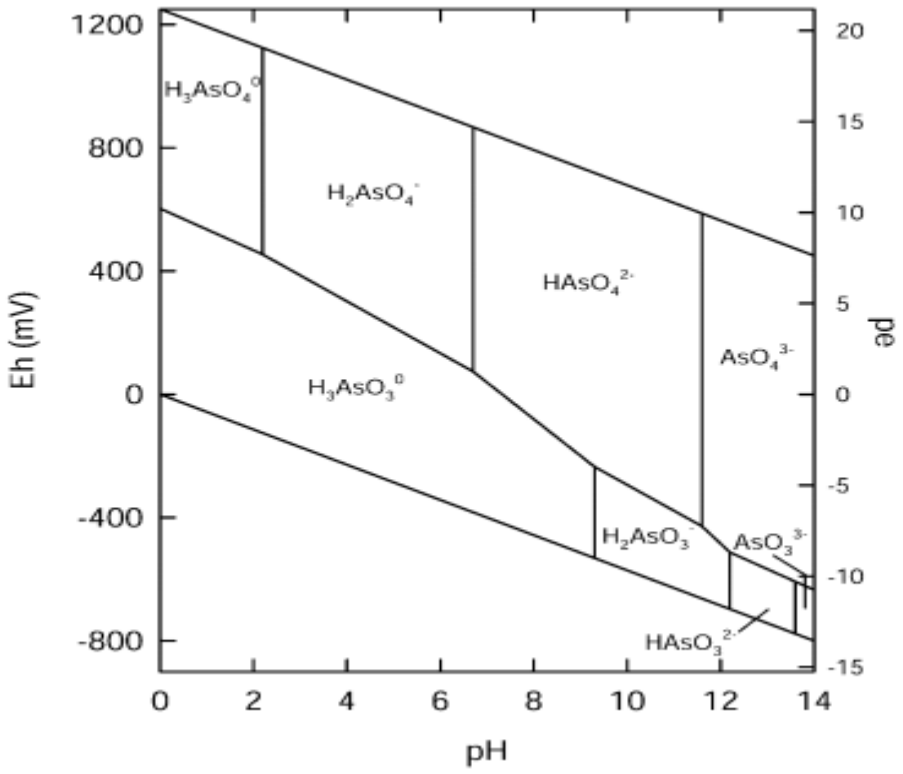

Figure 1.1. Eh-pH diagram for aqueous As species in the system As-O_2-H_2O at 25 ºC and 1 bar total pressure (adapted from ref. 2).

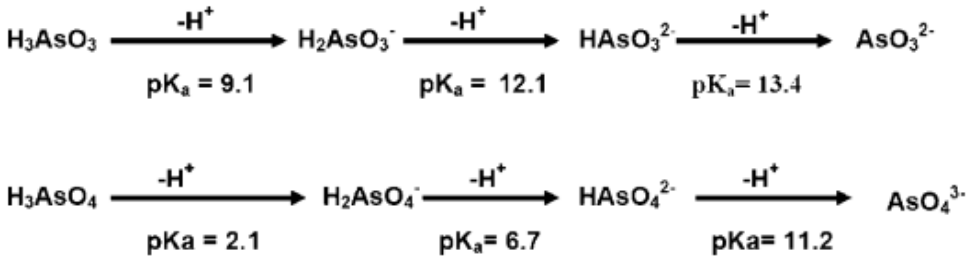

Figure 1.2. Dissociation of As(V) (adapted from ref. 3).

1.2 Arsenic removal methods

During the past decades, several techniques have been developed in the removal of arsenic from the wastewater, including chemical precipitation, adsorption, ion exchange/reverse osmosis, membrane, and so on. Table 1.1 summarizes the various processes that have been developed for the removal of arsenic from solution.

Table 1.1. Summary of arsenic removal processes (adapted from ref. 1).

Precipitation	Calcium arsenate Mineral-like arsenates Ferrous arsenates
Adsorption	Ferrihydrite Aluminum hydroxide Alumina Activated carbon Other sorbents
Ion Exchange/Reverse Osmosis	Ion exchange Liquid ion exchange Reverse osmosis
Cementation Processes	Iron cementation

All arsenic removal technologies have some kinds of advantage, limitations, and application scope. The major arsenic removal technologies are compared in Table 1.2.

Table 1.2. Summary of arsenic removal processes (adapted from ref. 3).

Major oxidation/precipitation tech.	Advantages	Disadvantages
Air oxidation	Relatively simple, low cost but slow; arsenic removal *in situ*; also oxidizes other organic and inorganic constituents in water	Removes primarily arsenic (V) and accelerates the oxidation process
Chemical oxidation	Oxidizes other impurities and kills microbes; relatively simple and fast, minimal residual masses	Efficient control of pH; low stability of waste causing build-up
Major coagulation/co-precipitation tech.	**Advantages**	**Disadvantages**
Alumen coagulation	Durable chemicals available; comparatively low capital cost and simple operation; effective over a wide pH range	Produces toxic sludge; low arsenic removal; pre-oxidation may be necessary
Iron coagulation	Common chemical products available; more efficient than the alumen coagulation in terms of the basis weight	Medium removal of As (III); sedimentation and filtration necessary
Lime treatment	Chemicals commercially available	pH adjustment required
Major ion exchange and sorption tech.	**Advantages**	**Disadvantages**
Activated alumina	Commercially available and relatively well known	Needs replacement after four to five regenerations
Iron-coated sand	Cheap; regeneration not required; remove both As (III) and As (V)	Not standardized; produces toxic solid waste
Ion exchange resin	Medium and capacity well-defined; independent of pH; specific ion resin exclusive to arsenic removal	High cost medium; high operation and maintenance technology; the regeneration creates a problem of mud disposal; As (III) is difficult to remove; life of resins
Major membrane technologies	**Advantages**	**Disadvantages**
Nanofiltration	Well defined and with high filtration efficiency	Very high capital and operational costs, preconditioning, high water rejection
Reverse osmosis	Without toxic waste production	Operation and maintenance of high-tech
Electrodialysis	Able to remove other contaminants	Production of toxic wastewater

1.2.1 Chemical precipitation method

The precipitation with trivalent iron salts and lime is the technique commonly applied in industry for arsenic removal. As reported by Harper et al. in 1992,[4] the chemical precipitation method had been identified as being the most effective means of arsenic treatment for a long time before 1980s. They did bench-scale treatability testing,

which was completed to determine the effectiveness of various coagulants, including ferric chloride, hydrated lime, sodium sulfide, and alum. The following Figure 1.3 is a schematic wastewater treatment system flow sheet.

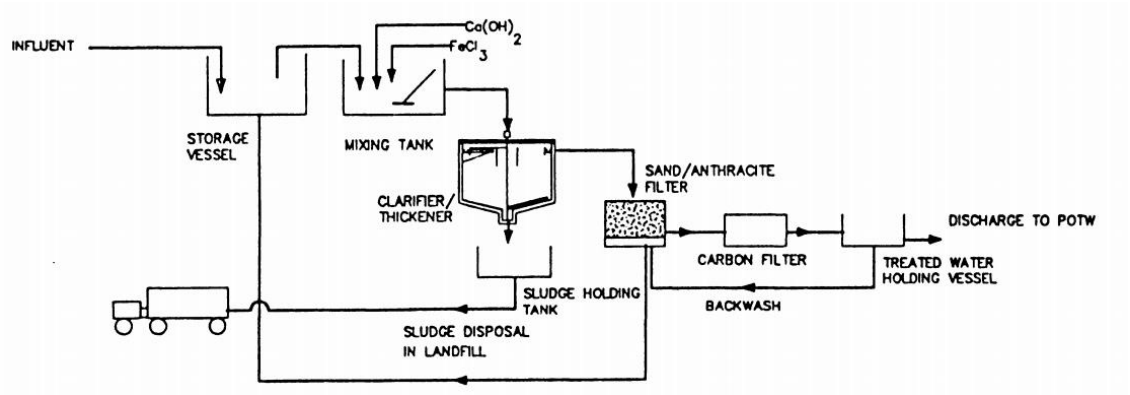

Figure 1.3. Wastewater treatment system flow sheet (adapted from ref. 4).

The influent was transferred to storage vessel and then to mixing tank, followed by adding ferric chloride and hydrated lime ($Ca(OH)_3$). The sludge was disposed by truck to landfill. And the upper solution was filtered by sand, adsorbed by carbon and achieved arsenic removal rates of 97 to 98%. This reduction of arsenic produced water that met the approved discharge permit limitation as established by the regulatory agency. The disadvantage of this method is the formation of several calcium arsenate compounds including $Ca_4(OH)_2(AsO_4)_2$, $Ca_5(AsO_4)_3OH$ and $Ca_3(AsO_4)_2$, the waste residues are hard to dispose, causing second contamination. Lime precipitation which was widely used in the past is being abandoned as a result of evidence showing that calcium arsenate

compounds decompose slowly in contact with CO_2 to form calcium carbonate and soluble arsenic acid.[1]

$$Ca_3(AsO_4)_2 + 3CO_2 + 3H_2O = 3CaCO_3 + 2H_3AsO_4$$

In the Canadian metallurgical industry, co-precipitation with ferric salts is the preferred method for removing arsenic. This technique has replaced lime precipitation which was the commercial used technology in industries until the early 1980s.

The co-precipitation with ferric salts can be described as following: When a solution with Fe(III) ions is neutralized rapidly, ferric oxyhydroxide, known as ferrihydrite, forms and precipitates.[1]

$$Fe^{3+} + (3+x)\ H_2O = FeO(OH)(H_2O)_{1+x} + 3H^+$$

Ferrihydrite has adsorption properties for AsO_3^{3-} and AsO_4^{3-}.[1]

$$FeO(OH)(H2O)_{1+x} + AsO_4^{3-} = AsO_4^{3-}\cdot FeO(OH)(H2O)_{1+x}$$

However, Ferric co-precipitation treatment process, the technology used industrially at present, produces large amounts of secondary waste with low stability, which leads to arsenic eventually being released back to the environment through natural oxidation processes.

1.2.2 New arsenic removal processes classification

In the late 1990s, several new technologies were developed. Arsenic removal technologies can be classified as adsorption-based technologies such as ion exchange (IX) or granular iron media adsorption (GIM) and membrane-based technologies such as nanofiltration (NF) or reverse osmosis (RO). (Figure 1.4).[5]

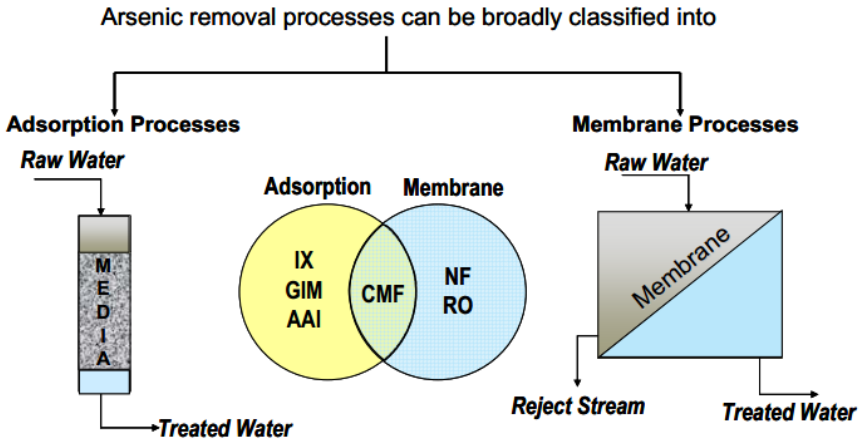

Figure 1.4. Arsenic removal processes (adapted from ref. 5).

Ion exchange method has good adsorption effect, but it is not suitable for multi-ions separation. Membrane processes are more complex than adsorption processes, which can cause high capital cost, and high TOC-containing waters resulting in more frequent cleaning requirements for membranes.

1.2.3 Adsorption method

Due to the low cost, good performance and easy operation, adsorption is considered to be one of the most effective approaches among these new-developed technologies.[5]

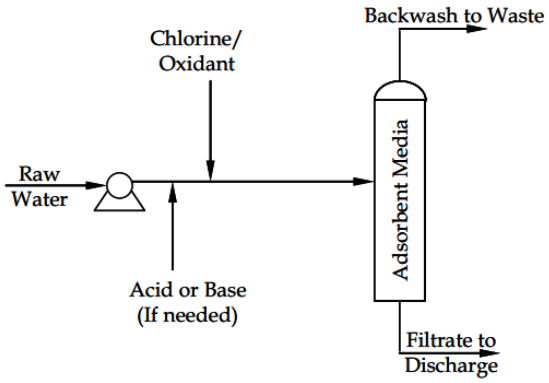

Figure 1.5. Schematic for arsenic removal using adsorbent media (adapted from ref. 5).

A typical process for adsorption process is shown in Figure 1.5. Raw water is oxidized by chlorination and then passed through the adsorbent media.[5] Adsorption is a useful tool for controlling the extent of aqueous arsenic pollution.

Several adsorbents have been developed and studied. Activated carbon was studied extensively for arsenic removal. However, it only removes a few milligrams of metal ions per gram.[3] Activated alumina is efficient but sorption efficiency is highest

only at low pH and arsenites must be pre-oxidized to arsenates before adsorption. Organic polymers are good adsorbents but with high cost.[3]

Iron compounds such as iron oxides, oxyhydroxides and hydroxides are the most widely used adsorbents. They have higher removal efficiency at lower cost compared with many other adsorbents. However, their adsorption capacity is highest only at low pH.[3]

1.2.3.1 Arsenic adsorption by iron oxide

Since 2000, iron oxide-based materials have been widely used in arsenic removal because of their low cost, natural abundance and effective performance for both As(V) and As(III) removal.

Ferroferric Oxide (Fe_3O_4) nanocrystals (NC) with low-field magnetic separation was firstly reported by Yavuz et al. in 2006.[6] The material was synthesized from the high temperature (320 °C) decomposition of finely ground Fe(O)OH in oleic acid, using 1-octadecene as solvent. The particle size was 12 ± 1.0 nm. A schematic of an oleic acid coated magnetite NC is showed in the following scheme (Figure 1.6, circles are iron (black), oxygen (red) and carbon (blue)).

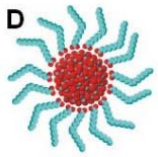

Figure 1.6. A schematic of an oleic acid coated magnetite NC (adapted from ref. 6).

The nanoscale Fe_3O_4 was acid-digested, and after As adsorption, the Fe and As concentrations in the digest were measured by ICP-AES and ICP-MS, respectively (Figure 1.7).[6]

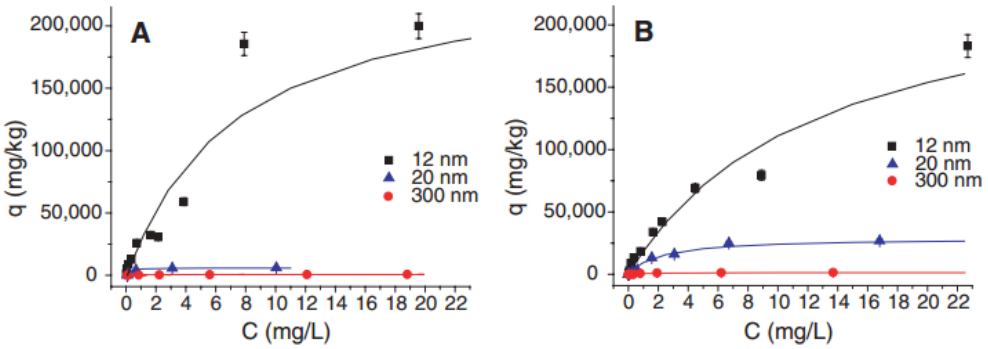

Figure 1.7. Arsenic adsorption studies with nanocrystalline (12 nm) and commercially available (20 and 300 nm) Fe_3O_4. (A) As(V) adsorption; (B) As(III) adsorption (adapted from ref. 6).

In 2011, Mou et al. reported magnetic Fe_2O_3 with a chestnut-like amorphous-core/γ-phase-shell hierarchical nanostructure (CAHN), which single crystalline γ-Fe_2O_3

nanorods, with a diameter of 20 nm and a length of 300 nm, radially grew from the surfaces of amorphous and porous Fe_2O_3 sub-microspheres (Figure 1.8).[7]

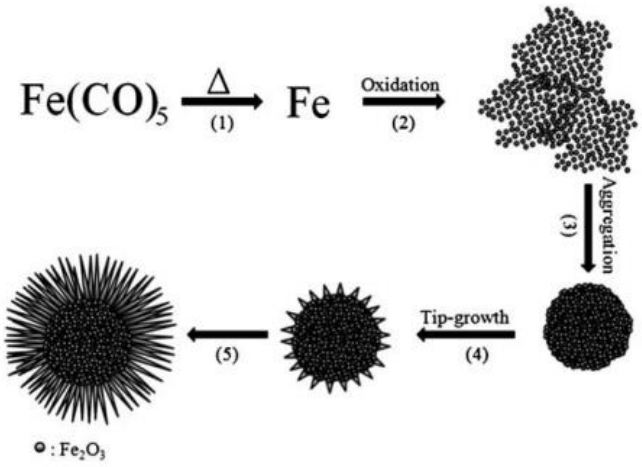

Figure 1.8. A schematic illustration of the formation process of the Fe_2O_3 CAHNs: (1) the formation of iron by decomposing $Fe(CO)_5$; (2) oxidation of iron into amorphous iron oxide nanoparticles; (3) aggregation of iron oxide nanoparticles into a porous sphere; (4) tip-growth of maghemite nanorods on the surface of the amorphous iron oxide sphere and finally (5) the growth into Fe_2O_3 CAHNs (adapted from ref. 7).

The as-obtained Fe_2O_3 CAHNs show maximum adsorption capacity of 137.5 $mg \cdot g^{-1}$capability for As(V). (Figure 1.9).[7]

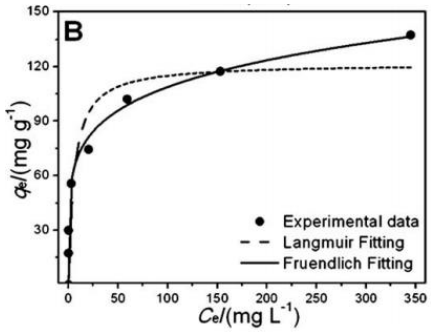

Figure 1.9. The equilibrium isotherm data of As(V) adsorption at pH 4 and room temperature, as well as the non-linear isotherm analysis using both the Langmuir and Freundlich adsorption equations (adapted from ref. 7).

Cao et al. reported a flowerlike α-Fe_2O_3 nanostructures were synthesized via a template-free microwave-assisted solvothermal method.[8] $FeCl_3 \cdot 6H_2O$ and urea were dissolved in anhydrous ethanol, then heated by microwave. The reaction time was less than 30 min with microwave heating. These flowerlike α-Fe_2O_3 nanostructures had a large surface area (130 m^2 g^{-1}) and abundant surface hydroxyl groups and showed excellent adsorption properties for As(V). The maximum adsorption capacity for As(V) was 51 $mg \cdot g^{-1}$ (Figure 1.10).[8]

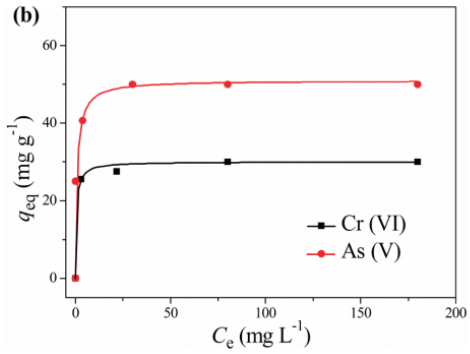

Figure 1.10. Adsorption isotherms of As(V) and Cr(VI) using flowerlike α-Fe_2O_3 nanostructures (adapted from ref. 8).

In 2013, Wei et al. reported a facile template-free fabrication of hollow nestlike α-Fe_2O_3 nanostructures,[9] also using microwave heating. Different with Cao,[8] they synthesized via a novel glycerol-assisted method. $FeCl_3 \cdot 6H_2O$ and urea were dissolved in a mixture containing of glycerol and water, followed by microwave heating at 140 °C for 30 min. A possible mechanism for the formation of hollow structures was proposed based on a systematic investigation of the morphology of products, prepared with different amounts of glycerol in the solvent (Figure 1.11).[9]

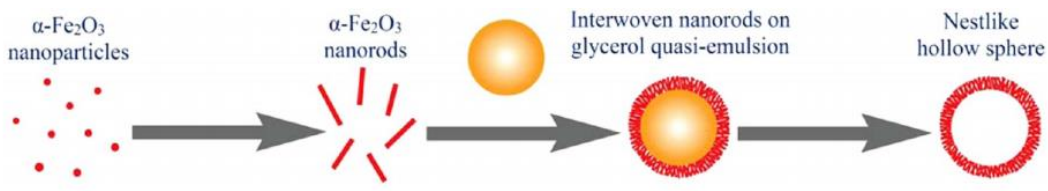

Figure 1.11. Schematic illustration of the formation mechanism of a hollow nestlike α-Fe_2O_3 nanostructure (adapted from ref. 9).

The experimental data fit well with the Langmuir adsorption model isotherms. Based on this isotherm, the maximum adsorption capacity was 75.3 $mg \cdot g^{-1}$ for As(V) for the hollow nestlike α-Fe_2O_3 nanostructures (Figure 1.12).[9]

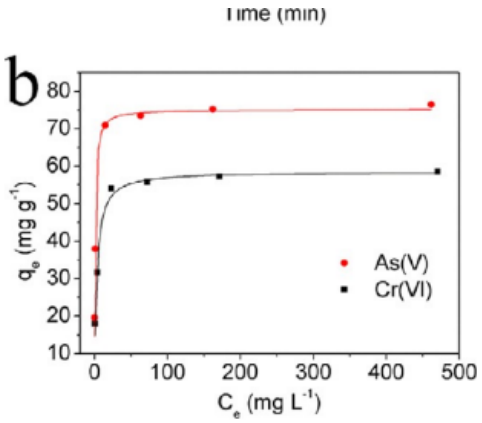

Figure 1.12. Adsorption isotherms of As(V) and Cr(VI) using the hollow nestlike α-Fe_2O_3 nanostructures (adapted from ref. 9).

In 2014, Das et al. reported a γ-Fe_2O_3 ultra-long magnetic nanochains for efficient arsenic removal.[10] The ultra-long γ-Fe_2O_3 nanochains possessed high surface area (151.12 $m^2\ g^{-1}$), large saturation magnetization (77.1 emu g^{-1}) that aided in their gas phase self-assembly into long chains (>100 μm) in an external magnetic field (Figure 1.13).

The magnetic nanochains were synthesized in a H_2/air diffusion flame. H_2 was bubbled though the liquid $Fe(CO)_5$ precursor, and the precursor-laden H_2 stream was passed through the central annulus in a co-annular burner. A stable, self-sustaining

laminar diffusion flame was established on the tubular burner that generated the iron oxide nanoparticles. A homogeneous magnetic field was established on each side of the flow (Figure 1.13). As seen in the following figure, the nanochains showed an excellent maximum adsorption capacity which was calculated to be 162 $mg \cdot g^{-1}$ (Figure 1.14).[10]

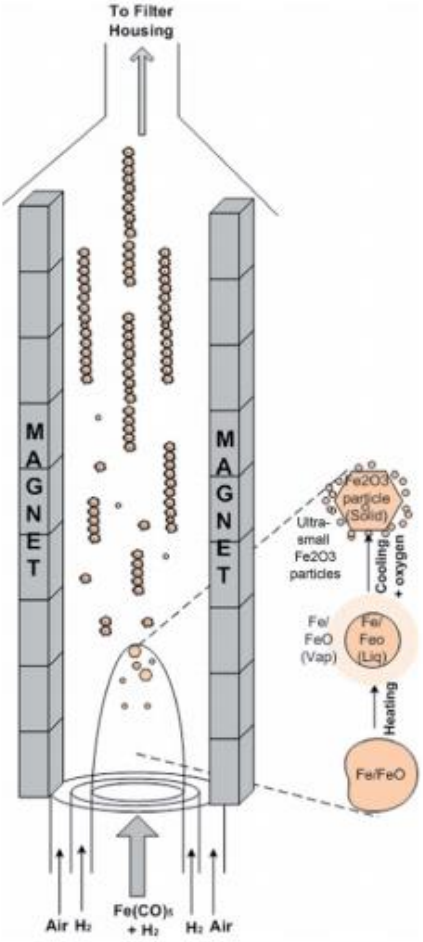

Figure 1.13. Flame synthesis set-up. The magnified area shows different phases of iron oxide nanoparticles formation in different flame heights (adapted from ref. 10).

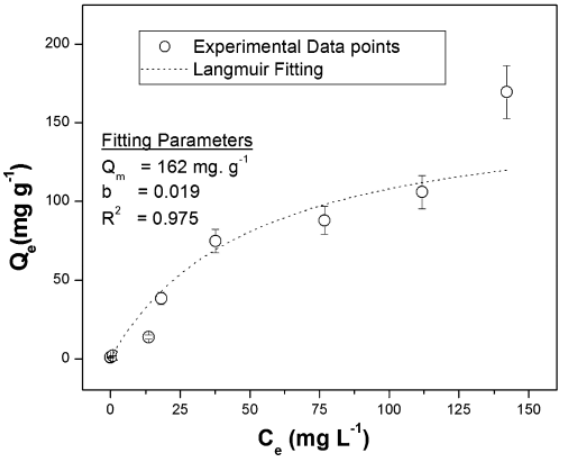

Figure 1.14. Room temperature equilibrium isotherm data of As(V) adsorption on the γ-Fe_2O_3 nanochains at pH 7 (adapted from ref. 10).

1.2.3.2 Arsenic adsorption by Fe/metal binary oxides

There are several literatures which reported synthesis of binary metal oxides nanocomposites for arsenic removal. Gupta et al. reported iron (III)-titanium (IV) binary mixed oxides, with As(III) adsorption capacity of 85 $mg \cdot g^{-1}$ and As(V) adsorption capacity of 14.3 $mg \cdot g^{-1}$.[11] Zhan et al. reported iron (III)-copper (II) binary oxides, with As(III) adsorption capacity of 122.3 $mg \cdot g^{-1}$ and As(V) adsorption capacity of 82.7 $mg \cdot g^{-1}$.[12] Xu et al. reported a synthesis of small-sized magnetic $MnFe_2O_4$ nanocrystal building blocks to form mesoporous clusters, with As(III) adsorption capacity of 27.327 $mg \cdot g^{-1}$.[13] Wen et al reported an iron manganese bimetal oxides, with an adsorption capacities of As(III) and As(V) 67.89 and 93.54 $mg \cdot g^{-1}$, respectively.[14]

In 2014, Chen et al. reported a facile hydrothermal synthesis of nanostructured hollow Iron-Cerium Alkoxides.[15] They successfully synthesized a novel nanostructured hollow Iron-Cerium Alkoxide (NH-ICA) with a high surface area and abundant surface functional groups through an ethylene glycol mediated solvothermal method.[15]

When the molar ratio of Fe to Ce was 5:1, the product has the highest surface area 271.5 m^2 g^{-1}, and exhibits the excellent adsorption capacities for both As(V) and As(III) (206.6 and 266.0 $mg \cdot g^{-1}$, respectively in Figure 1.15).[15]

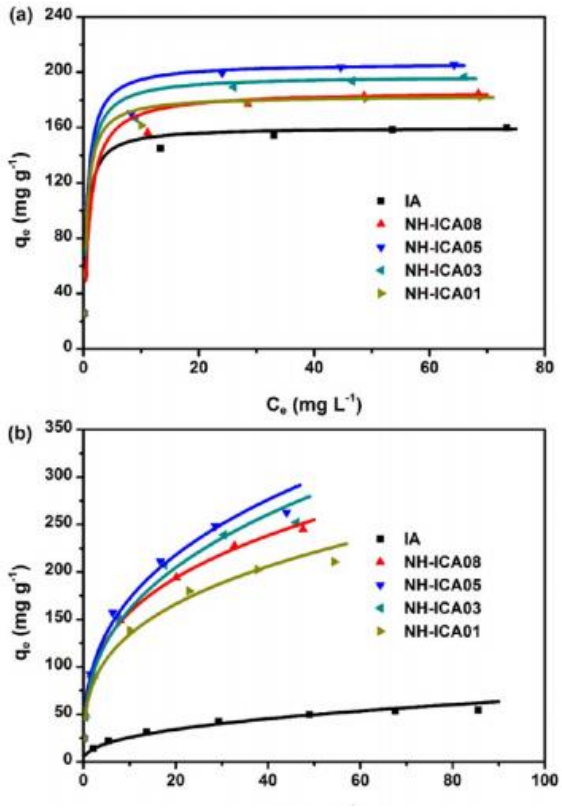

Figure 1.15. Adsorption isotherms of (a) As(V) fitted by the Langmuir model and (b) As(III) by the Freundlich model, respectively, on IA and NH-ICAs. The initial arsenic concentration ranged from 1 to 100 mg L^{-1}. The dosage of adsorbents and the initial pH value were 0.2 g L^{-1} and 6, respectively. NH-ICA08, NH-ICA05, NH-ICA03, and NH-ICA01, respectively, corresponding to the molar ratio (adapted from ref. 15).

1.2.3.3 Arsenic adsorption by Fe/Organic composites

There are several literatures which reported synthesis of Iron-organic composites for arsenic removal. Zhu et al. reported Iron and 1,3,5-Benzenetricarboxylic, with As(V) adsorption capacity of 12.3 mg·g^{-1}.[16] Santos et al. reported iron-PVA hydrogel

microspheres, with As(V) adsorption capacity of 87.2 $mg \cdot g^{-1}$.[17] Gupta et al. reported a synthesis of iron encapsulated chitosan nanospheres, with As(III) adsorption capacity of 94 $mg \cdot g^{-1}$ and As(V) adsorption capacity of 119 $mg \cdot g^{-1}$.[18] Yu et al reported cellulose@iron oxide nanoparticles, with an adsorption capacities of As(III) and As(V) 23.16 and 32.11 $mg \cdot g^{-1}$, respectively.[19]

1.2.3.4 Arsenic adsorption by Fe/Carbon composites

1.2.3.4.1 Arsenic adsorption by Fe/Graphene composites

Graphene oxide (GO)/iron oxide nanocomposites have been proposed to be promising adsorbents.[20] GO is produced by oxidative exfoliation of graphite, considered to be the most frequently used graphene precursor because of its low cost and abundance. More importantly, GO has a variety of oxygen-containing functional groups on its surface, including epoxy (COC), hydroxyl (OH), and carboxyl (COOH) groups, which causes graphene oxide sheets are hydrophilic and readily dispersible in water.[20]

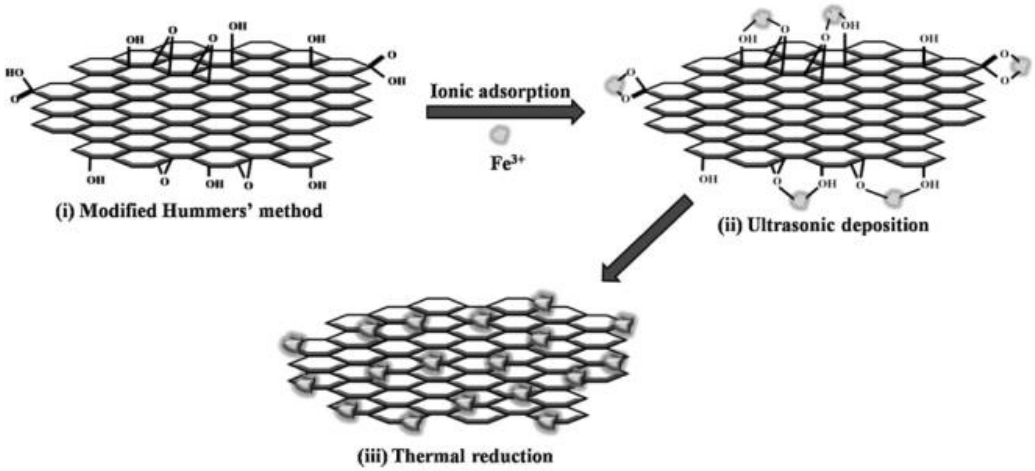

Figure 1.16. Scheme showing the reaction steps for preparation of a graphene/iron oxide hybrid where the two components are linked via hydroxyl groups (adapted from ref. 20).

Typically, graphene/iron oxide nanocomposites are synthesized shown in Figure 1.16. First, graphene oxide is prepared by the modified Hummers' method and then reacts with Fe^{3+} ions. The obtained graphene sheets are then thermally treated under a H_2 atmosphere and Fe_3O_4 nanoparticles are formed.[20]

Iron Oxide-Graphene Oxide composites were synthesized and reported by Chandra et al. in 2010.[21]

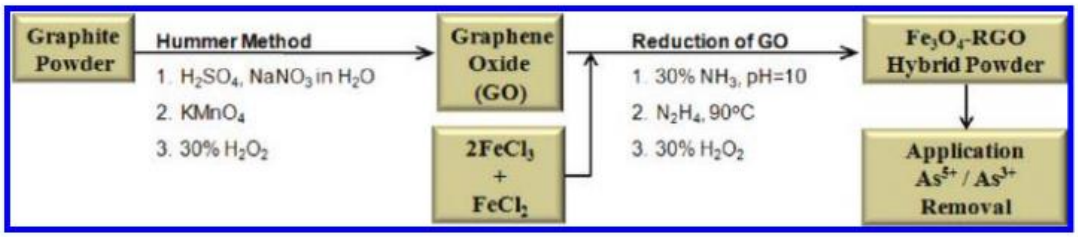

Figure 1.17. Synthesis and application of Fe_3O_4-RGO composites (adapted from ref. 21).

GO was synthesized by using the Hummers method through oxidation of graphite powder (Figure 1.17).[21] The Fe_3O_4-RGO composites were synthesized using ammonia solution (30%) and hydrazine hydrate at a temperature of 90 °C and pH 10. Since the composites show near complete (over 99.9%) arsenic removal within 1 ppb, they are practically usable for arsenic separation from water (Figure 1.18).[21]

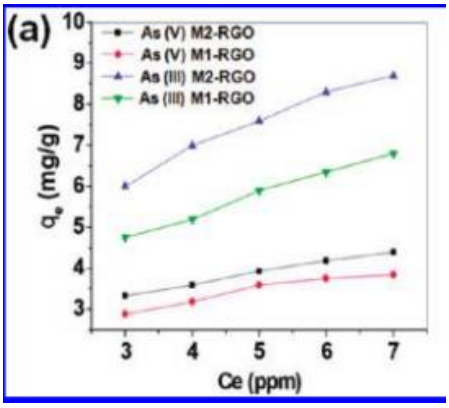

Figure 1.18. Adsorption isotherms of As(III) and As(V) on the Fe_3O_4-RGO composite (temperature 20 °C, pH 7) (adapted from ref. 21).

1.2.3.4.2 Arsenic adsorption by Fe/ porous carbon composites

Porous carbon materials have recently triggered enormous research activities because of their features such as high specific surface area, adjustable structure and pore size, good chemical and thermal stability, and great potential in adsorption and separation.[22]

The history of porous carbon materials can be traced to 3750 BC. It was firstly used by Egyptians to reduce copper, zinc, and tin ores. In 1773, the adsorption properties of porous carbonaceous material (charcoal) was first developed by Scheele for the adsorption of gases. The production of porous carbonaceous material, which was called activated carbon (AC), was commercialized in the twentieth century in the form of powder and granules. AC got huge attention in the World War I because its application for the adsorption of poisonous gases and purification of water.[22]

Conventional porous carbon materials, such as AC, are synthesized by pyrolysis and physical or chemical activation of organic precursors, such as coal, wood, fruit shell (coconut and almond), or polymers. These porous materials have nanoparticles on their outer and inner surface, and throughout the bulk of the materials. The pore size distribution, shapes, and volume of void spaces in porous material directly relates to their ability to perform the desired function in a particular application. It can be used for

adsorption, chromatography, energy storage and catalysis. AC is an extensively applied porous material because of easy mass production and low cost. However, it is difficult to produce purely mesoporous AC. Meanwhile, most of the AC has an abundant presence of micropores (pore size <2 nm), which limit the access of all internal and external areas by the atoms, ions, and molecules, causing low adsorption efficiency.[22]

Two kinds of advanced micro-mesoporous carbonaceous nanomaterials have received special attention in recent years. One is the carbon nanosphere (CNS) with micro-mesopores, and the second is highly ordered mesoporous carbon (OMC) materials. These two materials have uniform micro and mesopore size, high surface area, and large pore volume. These features are of great interest for a broad spectrum of applications. CNS and OMC materials can be used as adsorbents for the following applications: [23]

- Water pollution control: Adsorption of heavy metal ions, anions, organic pollutants.
- Gas storage: Hydrogen adsorption, CO_2 capture.
- Bioadsorption: Adsorption of small biomolecules, and large biomolecules.

Ouyang et al. have reported the monodisperse microporous CNSs prepared by the hydrothermal and carbonization of a monodisperse microporous polystyrene nanosphere.[24] The micropores structure is generated in two steps: First one polymerization of carbon source thereafter hypercrosslinking. These steps are described in Figure 1.19.

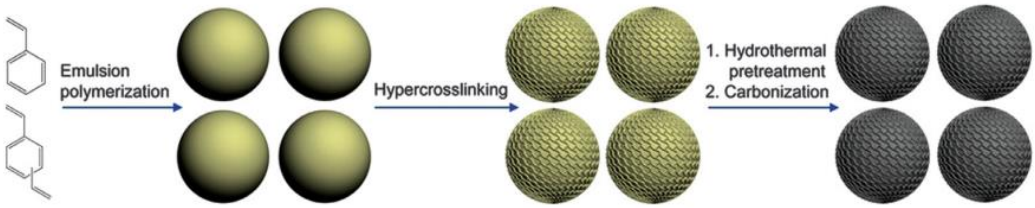

Figure 1.19. Schematic preparation process of microporous monodisperse carbon nanospheres (adapted from ref. 24).

Yoo et al. have proposed the two-step crosslinking strategy for the synthesis of highly microporous CNSs.[25] In the first step, divinyl benzene is used to crosslink the polystyrene and methyl methacrylate and the post-crosslinking process was applied for the conversion of the crosslinked polymer sphere to high yield carbon. The micropores were generated by the pyrolyzing methyl methacrylate during the carbonization process of the crosslinked sphere, and this step is described in the Figure 1.20.[25]

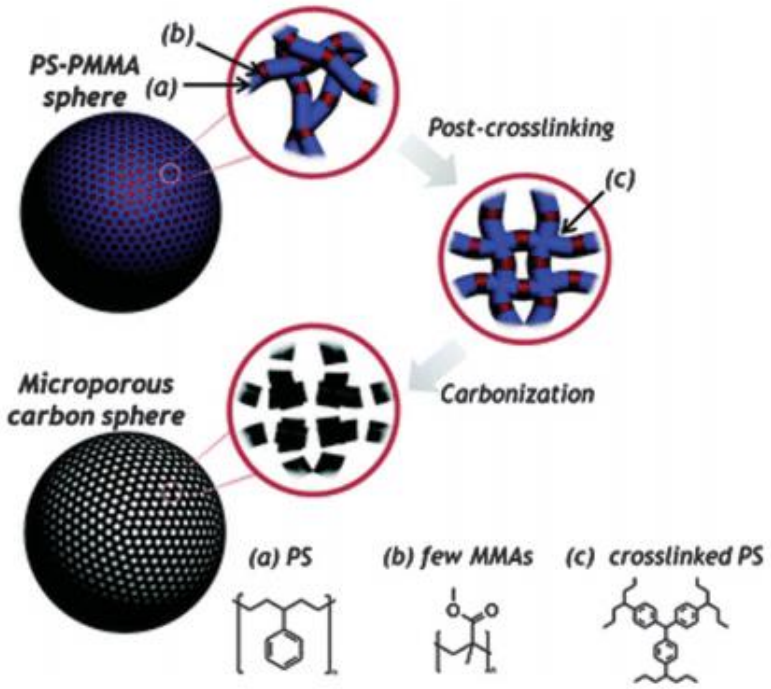

Figure 1.20. A schematic diagram showing the preparation of microporous carbon particles via selective pyrolysis of PS-PMMA spheres (adapted from ref. 25).

In general most of the CNSs are microporous by nature. The mesopores on the surface of CNSs are generated through the process of CNSs organic and inorganic precursor combinations and after the carbonization removal of inorganic precursor. Tashima et al. have reported the CNSs having micro and meso bimodal pores; which has been constructed by template and chemical activation approaches.[26]

Iron oxide-carbon based materials have been widely used in arsenic removal because of their low cost, natural abundance and effective performance for both As(V)

and As(III) removal.[20] Iron Oxide can be readily introduced into mesoporous carbon matrices, through:

- Direct synthesis approach [27]
- Post loading method [28]

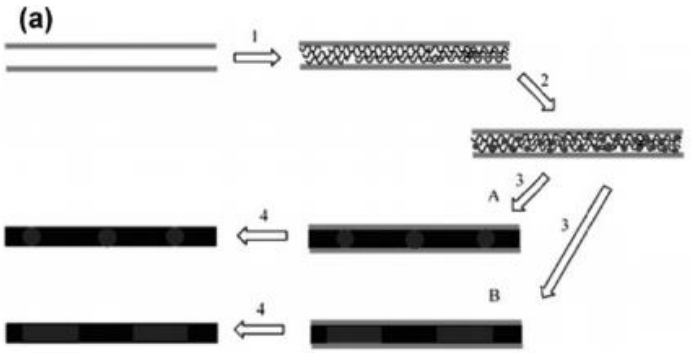

Figure 1.21. Schematic illustrations of preparing mesostructured meso-Fe/C composites via direct synthesis approach. (adapted from ref. 27).

A typical synthetic route toward mesoporous carbon/iron oxide hybrid is shown in Figure 1.21: 1) the furfuryl alcohol introduction into the channel of mesoporous silicas and polymerization; 2) iron ion absorption by the polyfurfuryl alcohol framework; 3) carbonization of the polyfurfuryl alcohol and the precursor decomposition to oxides in nanoparticle form with low Fe precursor content (A) and in nanorod form with high Fe precursor content (B); 4) removal of the silica template.[27]

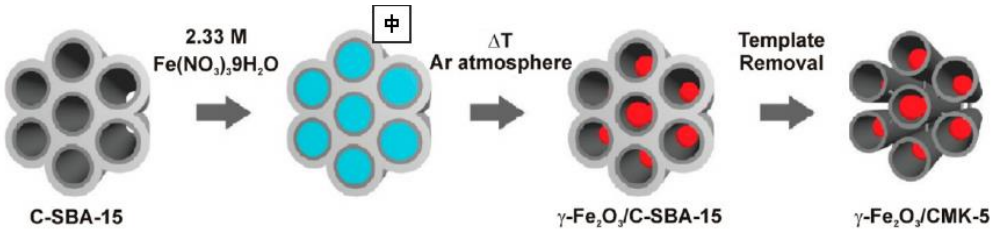

Figure 1.22. Schematic illustrations of preparing mesostructured meso-Fe/C composites via post loading method. (adapted from ref. 28).

Alternative synthetic procedure of mesoporous carbon/iron oxide nanocomposite is depicted in Figure 1.22: First, 2.33 M $Fe(NO_3)_3 \cdot 9H_2O$ containing one drop of HCl (37%) was impregnated into the pore space of carbon-silica composite (CS). Subsequently, the samples were dried at room temperature and further heated to temperatures up to 1000 °C with a heating rate of 2 °C min^{-1} and left at this temperature for 4 h in an argon atmosphere. Finally the silica was leached out by an aqueous NaOH solution. [28]

However, at a high metal loading level and/or a high converting temperature, the metal species normally aggregate severely into large particles. It is extremely challenging to fix highly concentrated (e.g., >20 wt%) and uniformly dispersed crystalline nanoparticles into predefined mesopores of carbons without aggregating and blocking the open pore networks.

Wu et al. reported Iron Oxide@Carbon for the first time for arsenic removal in 2012.[29] The construction of ordered mesoporous carbon encapsulated metal oxide nanoparticles with high concentration (40 wt%) homogeneously dispersed in predefined mesopores through a general ammonia-atmosphere pre-hydrolysis post-synthetic route. The obtained materials possessed uniformly dispersed, and exclusively mesopore-confined nanoparticles even at a very high metal oxide content up to 52 wt%.[29]

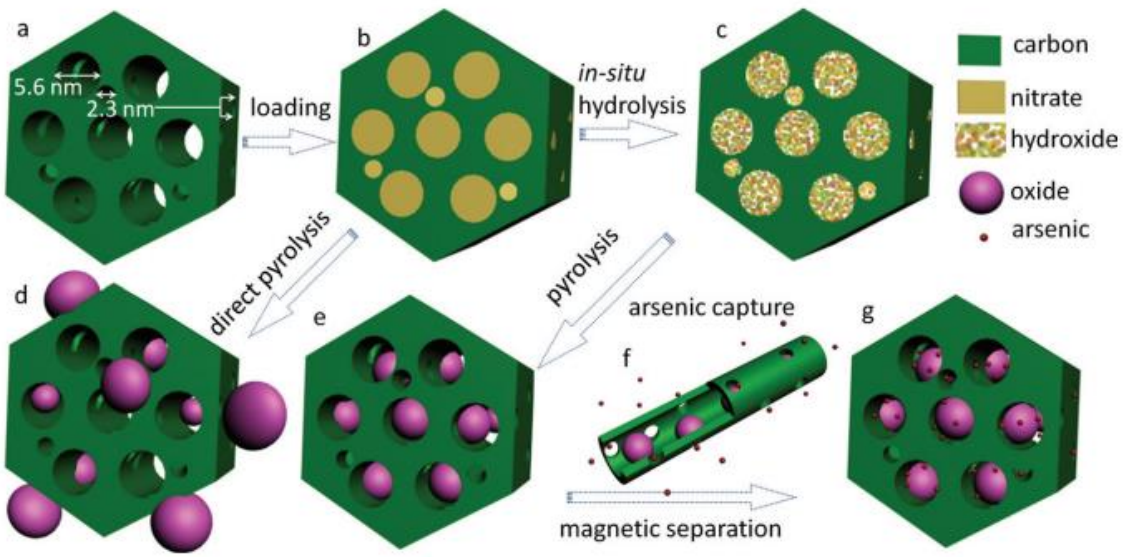

Figure 1.23. Illustration of the synthesis and arsenic capture processes for the ordered mesoporous Fe_2O_3@C encapsulates. (adapted from ref. 29).

The synthetic procedure of mesoporous carbon/iron oxide nanocomposite is depicted in Figure 1.23: a) the bimodal mesoporous carbon, b) carbon loaded with hydrated iron nitrate precursor, c) carbon loaded with iron hydroxide obtained by in situ

hydrolysis under ammonia atmosphere, d) iron oxide@carbon composites obtained by direct pyrolysis, e) the Fe_2O_3@C encapsulates obtained by pyrolysis following the pre-hydrolysis, f) arsenic capture, and g) arsenic-enriched encapsulates.[29]

Direct pyrolysis without the pre-hydrolysis step can result in a considerable amount of large particles aggregating on the external surface of the carbon matrix especially in the case of a high metal content. This is because of the low melting and boiling points of the hydrated metal nitrate precursors (e.g., ~47 and 100 °C for the melting and boiling points of hydrated iron nitrates). A large amount of metal precursors can transfer out of the mesopores before they were decomposed to oxides. On the contrary, through a simple pre-hydrolysis step, the obtained hydroxide had much higher melting points (e.g., ~136 °C for iron oxyhydroxide) and can easily decompose before melting to oxides, thus avoiding aggregating.[29]

Upon the loading of iron oxides, the Fe_2O_3@C-T encapsulates obtained after pyrolysis at 300 and 500 °C possessed impressive capacities of ~29.4 and 17.9 $mg \cdot g^{-1}$ for As(III) and As(V) (Figure 1.24).[29]

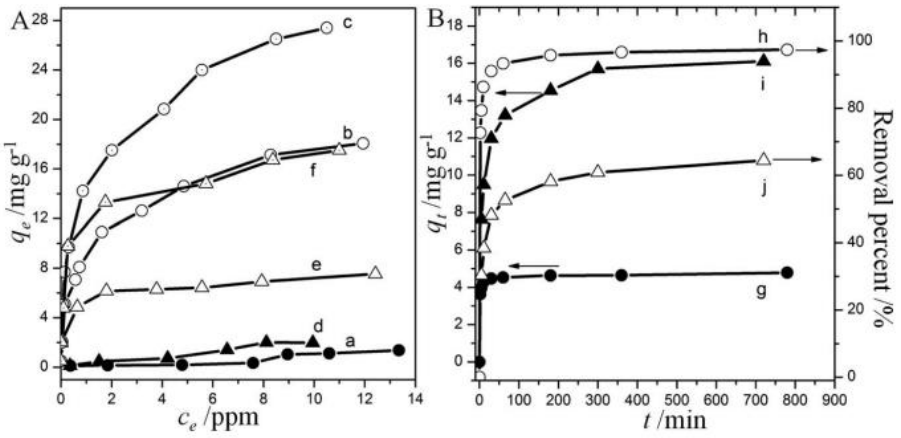

Figure 1.24. Adsorption isotherms at 25 °C (A) of As III (a–c) and As V (d–f) on the mesoporous carbon matrix (a, d), encapsulates Fe_2O_3@C-300 (c, f), and Fe_2O_3@C-500 (b, e). Time-dependent capture of As III (B) by the mesoporous encapsulates Fe_2O_3@C-500 with a sorbent loading of 1 mg mL^{-1} and an initial arsenic concentration of 5 (g, h) and 25 mg L^{-1} (i, j) (adapted from ref. 29).

There were several literatures which reported iron-carbon nanotubes or Iron-Cerium carbon nanotubes and their applications for arsenic removal. Ma et al. reported a one-pot synthesis of magnetic iron oxide/activated carbon nanotubes (MI/CNTs), based on as-prepared CNTs (APCNTs) using KOH activation.[30] The MI/CNTs composites were prepared by an alkali-activated method using APCNTs. The APCNTs were prepared by the catalytic chemical vapor deposition method. The computed maximum monolayer adsorption capacities had values of 9.74 mg·g^{-1} for As(V) and 8.13 mg·g^{-1} for As(III) on the MI/CNTs (Figure 1.25).[30]

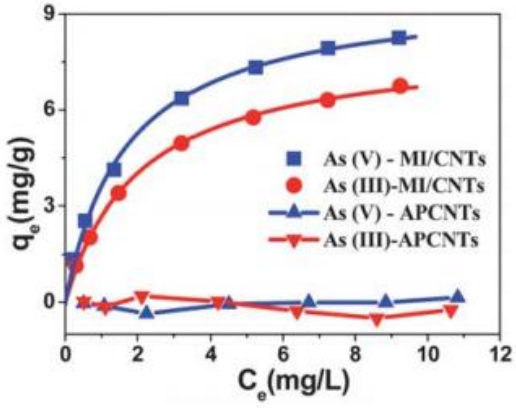

Figure 1.25. Arsenic adsorption of MI/CNTs (adapted from ref. 30).

In 2014, Chen et al. reported a one-pot solid-phase synthesis of magnetic multi-walled carbon nanotube/iron oxide composites.[31] The maximum arsenic adsorption capacities are 40.83 and 20.17 $mg \cdot g^{-1}$ for As(V) and As(III), respectively. In another literature, Yurum et al. reported a fast synthesis of iron oxide on activated carbon by microwave heating method.[32] With the MH technique, porous iron oxide was obtained with a loading value of 20.27% in just 9 min. Maximum adsorption capacity was 27.78 $mg \cdot g^{-1}$ for As(V).

Chen et al. reported Ce-Fe mixed oxides decorated multi-walled carbon nanotubes.[33] The decoration of the o-CNTs with Ce-Fe mixed oxides was performed by

surfactant (NaSDBS) assisted co-precipitation using $FeCl_3 \cdot 6H_2O$ as the ferric source and $CeCl_3 \cdot 7H_2O$ as the ceric source (Figure 1.26).

Figure 1.26. Schematic representation of the preparation of CF-CNTs via a surfactant assisted method (adapted from ref. 33).

The maximum adsorption capacity of the CF-CNTs for As(V) was 30.96 $mg \cdot g^{-1}$ which was slightly higher than that for As(III) (28.74 $mg \cdot g^{-1}$) (Figure 1.27).[33]

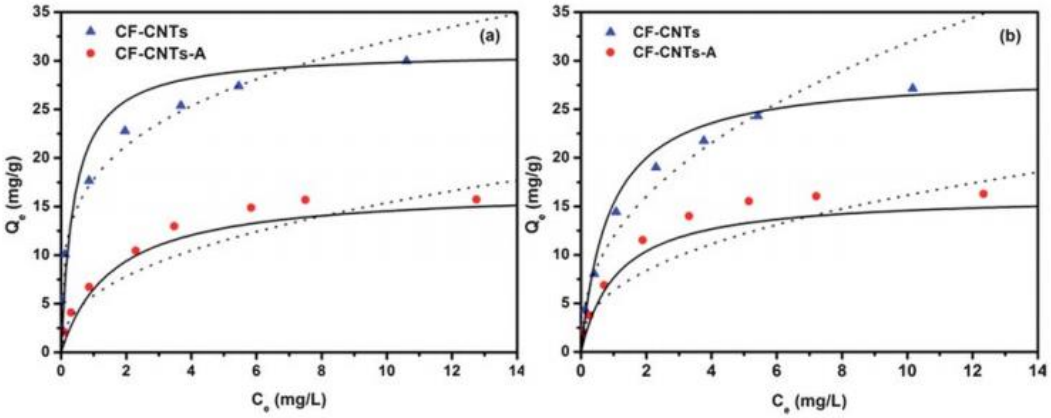

Figure 1.27. Adsorption isotherms of As(V) (a) and As(III) (b) on CF-CNTs at 298 K. The initial concentration ranged from 1 to 20 mgL^{-1}, the dosage of adsorbents was 0.2 g L^{-1}, and the initial pH values for the solutions were 4 and 7.5 for As(V) and As(III), respectively (adapted from ref. 33).

Lin et al. reported iron oxide/carbon aerogel structures, via the carbonization of composite Fe_3O_4/phenol–formaldehyde resin, shown in Figure 1.28.[34] Mesoporous Fe/CA structures were successfully synthesized with high specific surface areas of 487 $m^2 g^{-1}$ and pore sizes of 3.3 nm.[34]

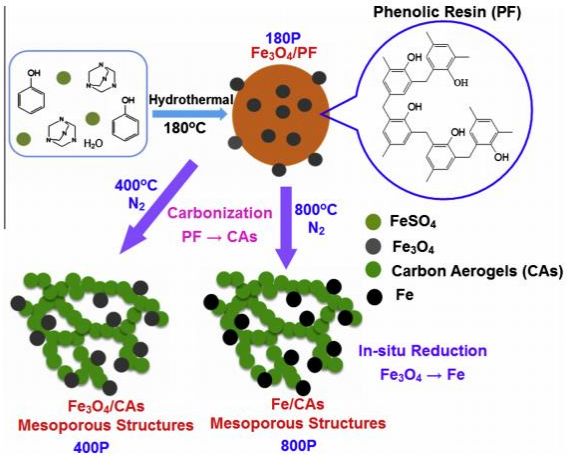

Figure 1.28. The scheme of the preparation of Fe_3O_4/CAs and Fe/CAs mesoporous structures using hydrothermal process (adapted from ref. 34).

The ferromagnetic Fe/CA mesoporous structures were further used for arsenic ion adsorption, and the maximum uptake of arsenic ions was calculated to be 216.9 $mg \cdot g^{-1}$ (Figure 1.29).[34]

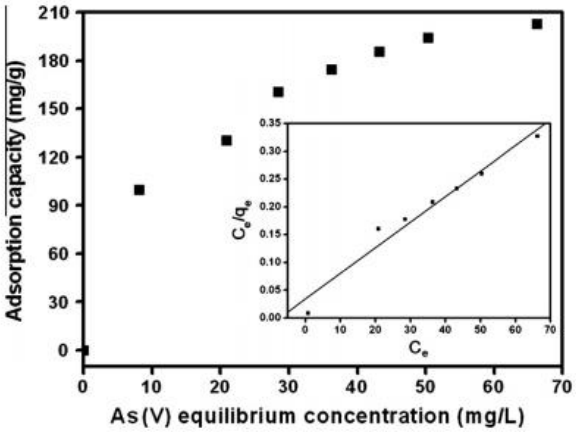

Figure 1.29. Plot of the arsenic adsorption capacity versus the arsenic equilibrium concentration (adapted from ref. 34).

1.2.3.5 Arsenic adsorption by Fe/Silica composites

Silica is another material which was used for excellent arsenic removal. In 2013, Du et al. reported iron oxide-diatomite composites as good absorbents, which was prepared by using a precipitation-deposition method. The maximal As(III) and As(V) adsorption capacities were 60.6 and 81.2 $mg \cdot g^{-1}$.[35]

Up till now, the best arsenic adsorption capacities were reported by Yang et al. in 2014.[36] They synthesized γ-Fe_2O_3 nanoparticles encapsulated in macroporous silica, which had superior arsenic removal performance. The weight percentage of Fe_2O_3 in the final products (denoted Fe_XMOSF) was adjusted to be 11.8, 21.0 and 34.8 wt% (X=1, 2 and 3, respectively).[36]

Fe_XMOSF composites showed a significantly increased As(V) adsorption capacities from 112 to 248 $mg \cdot g^{-1}$ while iron oxide content varying from 11.8 wt% to 34.8 wt%. Similar results were found in As(III) adsorption. Fe_XMOSF composites showed a better adsorption ability of As(III) than that of As(V). The As(III) adsorption capacities of Fe_XMOSF were 144, 296 and 320 $mg \cdot g^{-1}$ (X=1, 2, and 3, respectively) (Figure 1.30).[36]

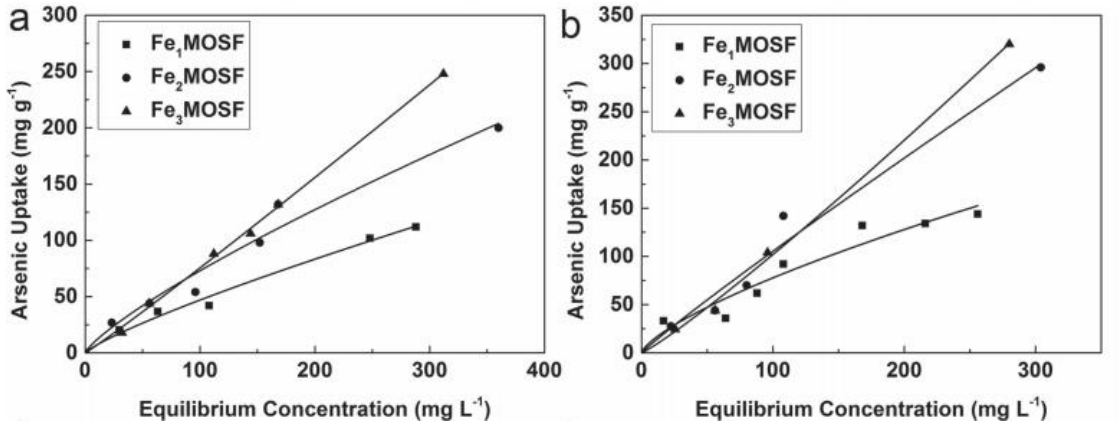

Figure 1.30. a) As(V) and b) As(III) adsorption isotherms of FexMOSF composites (adapted from ref. 36).

1.3 Summary

Table 1.3. Comparison of arsenic adsorption capacities.

Year	Adsorbents	Surface area $m^2 g^{-1}$	Pore size nm	Pore volume $cm^3 g^{-1}$	Adsorption capacity $mg g^{-1}$		Reference
					As(III)	As(V)	
	Iron oxide						
2006	Fe_3O_4 12nm				160	180	6
2011	Fe_2O_3 CAHNs	143				137.5	7
2012	Flowerlike α-Fe_2O_3	130				51	8
2013	Hollow Nestlike α-Fe_2O_3	152.4	3.8	0.42	58.6	75.3	9
2014	γ-Fe_2O_3 nanochains	151				162	10
	Fe/Metal binary oxides						
2009	Iron(III)–Titanium(IV) oxides	77.8	11		85	14.3	11
2013	Fe-Cu binary oxides				122.3	82.7	12
2013	$MnFe_2O_4$	74.68			27.27		13
2014	Fe-Mn bimetal oxides	579.6	6.25	0.777	67.89	93.54	14
2014	Hollow Fe-Ce Alkoxides	217.5	5.29	0.262	266	206	15
	Fe/Organic composites						
2012	Iron and 1,3,5-Benzenetricarboxylic					12.3	16
2012	Iron-PVA hydrogel	105	4.6	0.15		87.2	17
2012	Fe-Chitosan	69	5.9	0.103	94	119	18
	Fe/Graphene composites						
2010	Fe_3O_4-RGO				13.1	5.83	21
	Fe/Porous Carbon composites						
2012	Fe_2O_3-Carbon	1700	2.7, 5.6	1.7	29.4	17.9	29
2013	Fe_2O_3-Carbon nanotubes	662.1	2.26	0.726	8.13	9.74	30
2014	Fe_2O_3-Carbon nanotubes	209.8	4.62	0.39	20.17	40.83	31
2014	Fe_2O_3-Actiated carbon	1313	18.1	1.184		27.78	32
2013	Ce–Fe Oxides@Carbon nanotubes	216.3	2.8	1.17	28.74	30.96	33
2014	Fe_2O_3-Carbon aerogel	487	3.3			216	34
	Fe/Silica composites						
2013	Fe_2O_3-Diatomite	140			60.65	81.16	35
2014	Fe_2O_3-Macroporous silica	448	156	1.62	320	248	36

1.4 Objective and Organization of Thesis

The primary objectives of this thesis are (1) to design high-performance iron oxide nanocomposite adsorbents with the use of carbon nanospheres and graphene oxide, respectively, as the hosting matrix; (2) study the fundamental structure-performance relationships governing these nanocomposite adsorbents towards arsenic adsorption.

In Chapter 2, carbon nanospheres synthesized through a novel catalytic emulsion polymerization are employed as the carbon matrix for the iron oxide nanocomposites. A set of nanocomposite adsorbents has been synthesized, thoroughly characterized for their structure, composition, and textural properties, and investigated for their performance towards arsenic adsorption.

In Chapter 3, we developed and investigated the synthesis of a range of cost-effective amorphous iron oxide-graphene oxide (FeO_x-GO) nanocomposite adsorbents of significantly improved arsenic adsorption capacity. The key to the significantly enhanced adsorption capacity is the unique loading of amorphous iron oxide nanoparticles of high specific surface area on GO.

Chapter 4 summarizes the conclusions derived from the research conducted in this thesis, and suggests the possible directions for future work.

1.5 References

(1) P. Riveros, J. Dutrizac and P. Spencer. *Can. Metall. Q.*, 2001, Vol. 40, **No. 4**, 395–420.

(2) P. Smedley and D. Kinniburgh, *Appl. Geochem.*, 2002, **17**, 517–568.

(3) D. Mohan and C. Pittman, *J. Hazard. Mater.*, 2007, **142**, 1–53.

(4) T. Harper and N. Kingham, *Water Environ. Res.*, 1992, Vol. 64, **No. 3**, 200–203.

(5) G. Ghurye, J. Younan and J. Chwirka. *Journal of EUEC*, 2007, Volume **1**, 1–22.

(6) C. Yavuz, J. Mayo, W. Yu, A. Prakash, J. Falkner, S. Yean, L. Cong, H. Shipley, A Kan, M. Tomson, D. Natelson and V. Colvin. *Scienc*e, 2006, **314**, 964–967.

(7) F. Mou, J. Guan, Z. Xiao, Z. Sun, W. Shi and X. Fan. *J. Mater. Chem.*, 2011, **21**, 5414–5421.

(8) C. Cao, J. Qu, W. Yan, J. Zhu, Z. Wu, and W Song. *Langmuir*, 2012, **28**, 4573–4579.

(9) Z. Wei, R. Xing, X. Zhang, S. Liu, H. Yu, and P. Li. *ACS Appl. Mater. Interfaces*, 2013, **5**, 598–604.

(10) G. Das, C. Bonifacio, J. Rojas, K. Liu, K. Benthem, and I. Kennedy. *J. Mater. Chem. A*, 2014, **2**, 12974–12981.

(11) K. Gupta and U. Ghosh. *J. Hazard. Mater.*, 2009, **161**, 884–892.

(12) G. Zhan, Z. Ren, X. Zhang and J. Chen. *Water Res.*, 2013, **47**, 4022–4031.

(13) W. Xu, L. Wang, J. Wang, G. Sheng, J. Liu, H. Yu and X. Huang. *CrystEngComm*, 2013, **15**, 7895–7903.

(14) Z. Wen, Y. Zhang, C. Dai, B. Chen, S. Guo, H. Yu and D. Wu. *Microporous Mesoporous Mater.*, 2014, **200**, 235–244.

(15) B. Chen, Z. Zhu, S. Liu, J. Hong, J. Ma, Y. Qiu, and J. Chen. *ACS Appl. Mater. Interfaces*, 2014, **6**, 14016–14025.

(16) B. Zhu, X. Yu, Y. Jia, F. Peng, B. Sun, M. Zhang, T. Luo, J. Liu, and X. Huang. *J. Phys. Chem. C*, 2012, **116**, 8601–8607.

(17) A. Santos, F. Oliveira, F. Silva, D. Maria, J. Ardisson, W. Macêdo, H. Palmieri and M. Franco. *Chem. Eng. J.*, 2012, **210**, 432–443.

(18) A. Gupta, M. Yunus and N. Sankararamakrishnan. *Chemosphere*, 2012, **86**, 150–155.

(19) X. Yu, S. Tong, M. Ge, J. Zuo, C. Cao and W. Song. *J. Mater. Chem. A*, 2013, **1**, 959–965.

(20) J. Tucek, K. Kemp, K. Kim and R. Zbori. *ACS Nano*, 2014, VOL. 8, **8**, 7571–7612.

(21) V. Chandra, J. Park, Y. Chun, J. Lee, I. Hwang, and K. Kim. *ACS Nano*, 2010, **4**, 3979–3986.

(22) P.Tripathi, L. Gan, M. Li, and N. Rao. *J. Nanosci. Nanotechno*. 2014, Vol. 14, No. **2**, 1823–1837.

(23) Z. Wu and D. Zhao. *Chem. Commun.*, 2011, **47**, 3332–3338.

(24) Y. Ouyang, H. Shi, R. Fu, and D. Wu, *Sci. Rep*. 2013, **3**, Article number: 3:1430 1–5.

(25) H. Yoo and J. H. Moon, *RSC Adv*. 2012, **2**, 8934–8936.

(26) D. Tashima, E. Yamamoto, N. Kai, D. Fujikawa, G. Sakai, M. Otsubo, and T. Kijima, *Carbon*, 2011, **49**, 4848–4857.

(27) X. Dong, H. Chen, W. Zhao, X. Li and J. Shi, *Chem. Mater*., 2007, Vol. 19, **No. 14**, 3484–3490.

(28) A. Lu, J. Nitz, M. Comotti, C. Weidenthaler, K. Schlichte, C. Lehmann, O. Terasaki and F.Schuth. *J. Am. Chem. Soc.*. 2010, **132**, 14152–14162.

(29) Z. Wu, W. Li, P. Webley, and D. Zhao. *Adv Mater*., 2012, **24**, 485–491.

(30) J. Ma, Z Zhu, B. Chen, M. Yang, H. Zhou, C. Li, F. Yu and J. Chen. *J. Mater. Chem. A*, 2013, **1**, 4662–4666.

(31) B. Chen, Z. Zhu, J. Ma, M. Yang, J. Hong, X. Hu, Y. Qiu and J. Chen. *J. Colloid Interface Sci.*, 2014, **434**, 9–17.

(32) A. Yürüm, Z. Ataklı, M. Sezen, R. Semiat and Y. Yürüm. *Chem. Eng. J.*, 2014, **242**, 321–332.

(33) B. Che, Z. Zhu, J. Ma, Y. Qiu and J. Chen. *J. Mater. Chem. A*, 2013, **1**, 11355–11367.

(34) Y. Lin and J. Chen. *J. Colloid Interface Sci.*, 2014, **420**, 74–79.

(35) Y. Du, H. Fan, L. Wang, J. Wang, J. Wu and H. Dai. *J. Mater. Chem. A*, 2013, **1**, 7729–7737.

(36) J. Yang, H. Zhang, M. Yu, I. Emmanuelawati, J. Zou, Z. Yuan, and C. Yu. *Adv. Funct. Mater.* 2014, **24**, 1354–1363.

Chapter 2:

Carbon Nanosphere-Iron Oxide Nanocomposites as High-Capacity Adsorbents for Arsenic Removal

This chapter is adapted from a manuscript draft prepared (by H. Su and Z. Ye) for journal publication.

Abstract

In the design of iron oxide-derived composite adsorbents for arsenic removal, the matrix selected for the encapsulation of iron oxide active material is critical to their arsenic adsorption performance. The ideal matrix should have high surface area, high pore volume, and large pores that can accommodate the iron oxide nanoparticles while without causing the undesired pore filling or blockage. In this work, we report the use of hierarchical carbon nanospheres featured with high surface area, high pore volume, and hierarchical large mesopore/macropore structures as the matrix for the design of iron oxide composites. Iron oxide has been encapsulated into the carbon nanospheres at different contents (7–60 wt%). The composites have been systematically characterized for their structural, morphological, and textural properties, and investigated for their

performance for arsenic adsorption. An optimum iron oxide content of 13 wt% has been established with superior adsorption capacities of 416 and 201 mg g^{-1} achieved for As(III) and As(V), respectively, which are highest (for As(III)) or among the highest (for As(V)) reported thus far for iron oxide-based adsorbents. The results confirm the high potential of this class of composite adsorbents for arsenic removal from industrial wastewater streams. Meanwhile, the structure-performance relationship demonstrated herein is also of value to the further design of high-performance arsenic adsorbents.

2.1 Introduction

Arsenic is a persistent, bio-accumulative, toxic element, which is widely distributed in the Earth's crust with an average terrestrial content of about 5 g ton^{-1}.[1] Arsenic contamination of natural water sources due to mineral leaching and/or anthropogenic has been recorded by World Health Organization as a first priority issue.[1-3] The main species of arsenic in natural environment are arsenite (As(III)) and arsenate (As(V)), with As(V) predominant under oxidizing conditions and As(III) in moderately reducing environments such as groundwater. Generally, both species exist in natural water simultaneously, with As(III) being more toxic and more difficult for removal than As(V).[1-3] Various techniques have been developed to remove arsenic from both natural and industrial water sources. Among them, adsorption is most economical and efficient, particularly in the low arsenic concentration range. A broad spectrum of adsorbents have been extensively studied and developed to arsenic removal. These include commercial metal oxides, activated carbons, natural minerals, soils and constituents, agricultural and industrial by-products/wastes, etc.[3,4]

Iron oxide-derived adsorbents have received, in particular, enormous interest for arsenic removal due to their superior performance for arsenic adsorption while with low cost.[5] Iron oxides in various forms have been studied, such as amorphous iron oxide,[6,7]

goethite (α-FeOOH),[8] hematite (α-Fe_2O_3),[8,9] crystalline magnetic maghemite (γ-Fe_2O_3) and magnetite (Fe_3O_4) nanoparticles,[10-12] and various iron oxide nanostructures.[13-20] Among the various forms of iron oxides, amorphous iron oxides show the highest adsorption capacity (as high as 260 and 200 mg g^{-1} for As(III) and As(V), respectively) due to its highest specific surface area,[8] but with the difficulty (as fine powders) for separation and its tendency to form low-surface-area crystalline iron oxides during preparation.[4] Crystalline iron oxides generally show lowered adsorption capacity due to their low surface area.[10-12] Reducing the size of the crystalline iron oxide nanoparticles can substantially increase the surface area and consequently arsenic adsorption capacity.[11,12] However, such ultra-small crystalline nanoparticles are difficult for separation and tend to aggregate easily with deteriorated adsorption performance. The various iron oxide nanostructures often show relatively low adsorption capacity.[13-20] Meanwhile, they have the issue of cost-effectiveness due to the requirement of special, sophisticated synthesis and/or expensive additives/precursors.

To facilitate more convenient adsorbent separation, iron oxide-derived composite adsorbents with iron oxides loaded onto various matrices have also been extensively developed for arsenic adsorption.[3,4] In this aspect, a careful selection of the appropriate matrices and the uniform dispersion of iron oxide are key to the performance of the resulting composite adsorbents. The desired matrices should have open 3-dimensional

interconnected pore structures with accessible, high surface area and pore volume. Meanwhile, the pore size of the matrices should be significantly larger than that of the loaded iron oxide nanoparticles, particularly at high iron oxide content, so as to avoid/minimize pore blockages, which would otherwise affect the mass diffusion and consequently the adsorption performance. Typical matrices have included abundant ones, such as naturally occurring minerals,[21] activated carbons,[22] graphene oxide (GO),[23-34] and cellulose,[35] as well as some specially-synthesized ones, such as mesoporous carbons,[36,37] carbon nanotubes,[38] macroporous silica,[39] etc. The majority of composite adsorbents reported to date show limited arsenic adsorption capacities, with significant room for improvements. One exception is the iron oxide-macroporous silica foam composite adsorbent reported by Yu et al.,[39] which shows remarkably high adsorption capacity [320 and 248 mg g^{-1} for As(III) and As(V), respectively]. Therein, the encapsulation of iron oxide at high contents (up to 34.8 wt%) does not block the open pore structures of the macroporous silica foam substrate having large macropores.

In this article, carbon nanospheres (CNS) having unique hierarchical large meso-/macro-pore structures are chosen for the first time as the porous matrix to fabricate iron oxide nanocomposite adsorbents of high arsenic adsorption capacity. CNS is synthesized via carbonization of polymer nanospheres obtained by catalytic emulsion polymerization of 1,3-diethynylbenzene (DEB),[40] followed with further activation and surface

modification. Iron oxide has been loaded onto the CNS matrix at different content (7–60 wt%). The resulting composites have been systematically characterized with various techniques for their compositional, structural, and textural properties. Their performance for arsenic adsorption has been evaluated. High adsorption capacities of 416 and 201 mg g^{-1} for As(III) and As(V), respectively, have been achieved, which are even better than or comparable to the best results demonstrated thus far in the literature for iron oxide-derived composite adsorbents.

2.2 Experimental Section

2.2.1 Materials

1,3-Diethynylbenzene (DEB, 97%, Aldrich), sodium dodecyl sulphate (SDS, ≥98.5%, Aldrich), palladium acetate (98%, Strem Chemicals), α,α'-bis(di-tert-butylphosphino)-o-xylene (97%, Strem Chemicals), methanol (ACS reagent, Fisher Scientific), methanesulfonic acid (99.5%, Aldrich), dichloromethane (HPLC grade, Aldrich), ammonium persulfate (98%, Aldrich), sulfuric acid (96.9 wt.%, Fisher Scientific), iron (III) nitrate nonahydrate (≥98%, Aldrich), ethanol (ACS reagent, Fisher Scientific), were used as received without any additional purification. Deionized water was purified by a Barnstead/Synbron Nanopure II purification system.

Sodium (meta)arsenite ($NaAsO_2$, ≥90%, Aldrich) and sodium arsenate dibasic heptahydrate ($Na_2HAsO_4 \cdot 7H_2O$, ≥98%, Aldrich) were used as the source of As(III) and As(V), respectively. Fresh ammonium persulfate (APS) solution at 1.0 M was prepared in 2 M H_2SO_4. $Fe(NO_3)_3$ solution at 20 wt% was freshly prepared in ethanol. Standard stock solutions of As(III) and As(V) were prepared in deionized water at an arsenic concentration of 2,000 mg L^{-1}. The standard solutions with other different concentrations were prepared by diluting the standard stock solutions. The pH of the standard solutions was adjusted to desired values by adding an appropriate amount of HNO_3 or NaOH.

2.2.2 Synthesis of carbon nanospheres (CNS) and CO_2-activated carbon nanospheres (A-CNS)

CNS was synthesized by a catalytic minemulsion polymerization technique developed by our group.[40] Poly(DEB) nanospheres with an average size of ca. 24 nm were first synthesized by catalytic miniemulsion polymerization of DEB. Sodium dodecyl sulfate (SDS) (1.6 g) was dissolved in deionized water (31.2 g) in a round-bottom Schlenk flask, followed with the addition of DEB (3.72 g; 29.5 mmol). The mixture was sonicated for 15 min and was then stirred for 5 h at 60 °C. In the meantime, palladium acetate (6.62 mg; 0.03 mmol) and α,α′-bis(di-t-butylphosphino)-o-xylene (34.9 mg; 0.09 mmol) were dissolved in a mixture solvent containing 0.54 mL of dichloromethane and

0.06 mL of methanol to prepare a catalyst solution. Then the catalyst solution was injected into the flask, followed by the addition of five drops of methanesulfonic acid, to start the miniemulsion polymerization. The polymerization lasted overnight in N_2 atmosphere under stirring at 450 rpm at 60 ºC, rendering a dark brown miniemulsion dispersion of polymer nanospheres. A hydrothermal treatment of the resulting polymer nanospheres was subsequently carried out. The miniemulsion was diluted with deionized water by 15 times. The mixture was heated in an autoclave at 220 ºC overnight. The resulting hydrothermally treated polymer precipitates were collected by filtration, washed with a large amount of water, and dried under vacuum at 60 ºC for 48 h, rendering the polymer nanospheres (2.77 g). Pyrolysis of the polymer nanospheres in a tube furnace at 800 ºC for 1 h in a nitrogen atmosphere (preceded with heating from room temperature to 800 ºC at a heating rate of 10 ºC min^{-1}) rendered CNS (1.65 g).

A-CNS was prepared by CO_2 activation of CNS at 900 ºC for 3 h. In a tube furnace, CNS (1.65 g) was heated to 900 ºC at a rate of 10 ºC min^{-1} in a flowing N_2 atmosphere. After reaching 900 ºC, the atmosphere was changed to CO_2 within 5 min and the temperature was maintained for 3 h. When the activation was finished, the atmosphere was switched back to N_2 within 5 min, followed with natural cooling of the sample down to room temperature in the N_2 atmosphere, rendering A-CNS (0.8 g).

2.2.3 Synthesis of iron oxide-CNS composites (FeO_x-CNSs)

Iron oxide-CNS composites were synthesized by following a similar method reported by Zhao et al. for the preparation of mesoporous iron oxide-carbon nanocomposites.[36] Surface oxidation of A-CNS with APS was first undertaken to render S-CNS with improved surface polarity for the loading of iron oxide. A-CNS (240 mg) was dispersed and stirred in 20 mL of 1.0 M acidic APS solution (in 2 M H_2SO_4) at 70 ºC for 12 h. The solids were then filtered, washed with copious amounts of water and then methanol, and dried under vacuum at 60 ºC overnight, rendering S-CNS (200 mg).

The following is the procedure used for the synthesis of the representative iron oxide-CNS nanocomposite having an iron oxide content of 13 wt% (i.e., FeO_x-CNS-13). S-CNS (200 mg) was dispersed in absolute ethanol (1.4 g), followed by the addition of a 20 wt% ethanolic solution of $Fe(NO_3)_3$ (152 mg, 374 mmol). After sufficient and subsequent solvent evaporation, the resulting powder was transferred into a small plastic ampoule. The ampoule was subsequently placed in a Teflon bottle containing a ~14 wt% ammonia solution (~10 mL), but without direct contact of the powder with the ammonia solution. After sealing, the bottle was heated in an oven at 60 ºC for 3 h to hydrolyze the metal precursor in situ. After cooling, the product was filtered and washed with small amounts of water and methanol. After drying at 60 ºC under vacuum overnight, the solid

product was pyrolyzed at 300 ºC in a N_2 atmosphere for 1 h to obtain FeO_x-CNS-13 (0.2 g).

Other nanocomposites (FeO_x-CNS-7, FeO_x-CNS-28, and FeO_x-CNS-60) having different contents of iron oxide (7, 28, and 60 wt%, respectively) were similarly prepared with the feed amounts of S-CNS and iron nitrate at different mass ratios (50 mg/19 mg, 100 mg/197 mg, and 50 mg/380 mg, respectively).

2.2.4 Characterizations and Measurements

Thermogravimetric analysis (TGA) of the various composites was carried out on a Q50 TGA from TA Instruments. Measurements were performed in an air atmosphere with a continuous air flow of 60 mL min^{-1} through the sample furnace and a continuous N_2 flow of 40 mL min^{-1} through the balance compartment. In a typical measurement, the sample (10 mg) was heated to 100 ºC at a rate of 10 ºC min^{-1}, held at 100 ºC for 10 min, and then heated to 800 ºC at a rate of 10 ºC min^{-1}. N_2 sorption analysis was carried out with a Micromeritics ASAP 2020 physiosorption analyzer at 77 K to determine their Braunauer–Emmett–Teller (BET) specific surface area, pore volume, and pore size distribution. Before the sorption measurements, the samples were degassed under vacuum at 180 ºC for at least 12 h. X-ray photoelectron spectroscopy (XPS) measurements of the

samples were carried out on a Thermo Scientific Theta Probe XPS spectrometer. A monochromatic Al Kα X-ray source was used, with a spot area of 400 μm. The samples were run in a standard mode, i.e., all angles collected (60º angular acceptance) for the survey spectra, and for the region spectra. Wide-angle x-ray diffraction (XRD) patterns were recorded on an X'Pert Pro diffractometer with Cu radiation (wavelength 1.54 Å) at room temperature. Transmission electron microscopy (TEM) images were taken on a JEOL 2010F field emission electron microscope operated at 200 keV, equipped with energy-dispersive spectroscopy (EDS). The TEM samples were prepared by depositing a few drops of a dilute dispersion of the samples in methanol on holey grids, followed with drying. Dynamic light scattering (DLS) and zeta potential measurements of the dilute dispersions (0.1 mg mL^{-1}) of the various samples were performed on a Brookhaven NanoBrook Omni Instrument at 25 ºC. Fourier-transformed infrared (FTIR) spectra were obtained on a Thermo Scientific Nicolet 6700 Analytical FTIR spectrometer. The samples were prepared as pellets using spectroscopic-grade KBr. The arsenic concentration of the various aqueous solutions in the adsorption study was measured with an Analytik Jena 810 ICP-MS system with a detection limit of 50 μg L^{-1}.

2.2.5 Arsenic Adsorption

Batch adsorption of arsenic with all adsorbents (A-CNS, S-CNS, or FeO_x-CNS composites) was all undertaken with an adsorbent loading of 1.0 mg mL^{-1} at 23 ºC. Typically, the adsorbent (1 mg) was dispersed in various As(III) or As(V) solutions (1 mL) at different known concentrations (50–2,000 mg L^{-1}), followed by magnetic stirring (300 rpm) for 24 h to achieve equilibrium. Afterwards, the dispersion was filtered with 0.2 µm syringe filter and the filtrate was measured with ICP-MS for equilibrium arsenic concentration and for the calculation of the amount of adsorbed arsenic to construct adsorption isotherms. The adsorption isotherms were fitted with Freundlich model (Equation 1).

$$q_e = k(C_e)^{1/n} \qquad (1)$$

where q_e is the equilibrium adsorption uptake (mg g^{-1}), C_e is the equilibrium concentration (mg L^{-1}), k is the Freundlich constant, and n is the index that stands for heterogeneity of adsorbent.

To obtain the adsorption kinetic curves, FeO_x-CNS-13 (1 mg) was dispersed in a series of As(III) and As(V) solutions with the same volume (1 mL) and initial concentrations (950 mg L^{-1} for As(III) and 800 mg L^{-1} for As(V)). Each dispersion was stirred for a prescribed period of time (ranging from 15 min to 24 h) and was quickly

filtered for measurement of the corresponding equilibrium concentration of As(III) and As(V), thus giving rise to the time-dependent adsorption uptake. The adsorption kinetics was fitted with the pseudo-second-order kinetic model (Equation 2 or 3) based on which the initial adsorption rate was obtained (Equation 4).

$$dq_t/dt = k_2(q_e - q_t)^2 \qquad (2)$$

$$t/q_t = 1/(k_2 q_e^2) + t/q_e \qquad (3)$$

$$V_0 = k_2 q_e^2 \qquad (4)$$

Where q_t is the adsorption uptake (mg g^{-1}) after a time of t (min), k_2 is the rate constant (g mg^{-1} min^{-1}), and V_0 is the initial adsorption rate (mg g^{-1} min^{-1}).

2.3 Results and Discussion

2.3.1 Synthesis and Characterization of Carbon Nanosphere Matrix

The carbon nanosphere matrix (S-CNS), employed herein for the construction of the composite adsorbents, was synthesized by CO_2-activation of carbon nanospheres (CNS) obtained by a unique catalytic miniemulsion polymerization technique followed with surface oxidization. Scheme 1 summarizes the synthesis. The catalytic miniemulsion polymerization technique was recently developed by our group for the synthesis of carbon nanospehres.[40] Herein, the miniemulsion polymerization of a cross-linkable dialkyne monomer, DEB, renders uniform poly(DEB) polymer nanospheres (average size of 27 nm

with polydispersity index of 0.19 as per DLS characterization; see Figure S2.1 in Supporting Information). Each polymer nanosphere is constructed uniquely with highly cross-linked poly(DEB) networks. Carbonization of the polymer nanospheres following hydrothermal treatment renders CNS.[40] Having relatively low specific surface area (524 $m^2\ g^{-1}$) and pore volume (0.84 $cm^3\ g^{-1}$) as shown below, CNS, directly, is unsuitable as the matrix for iron oxide. CO_2 activation is thus employed to yield A-CNS with dramatically enhanced surface area and pore volume. Consisting predominantly of carbon, the surface of A-CNS is highly hydrophobic and incompatible with polar iron oxide. Wet chemical surface oxidation[41] of A-CNS is further taken to render S-CNS with improved surface polarity in order for uniform encapsulation of iron oxide.

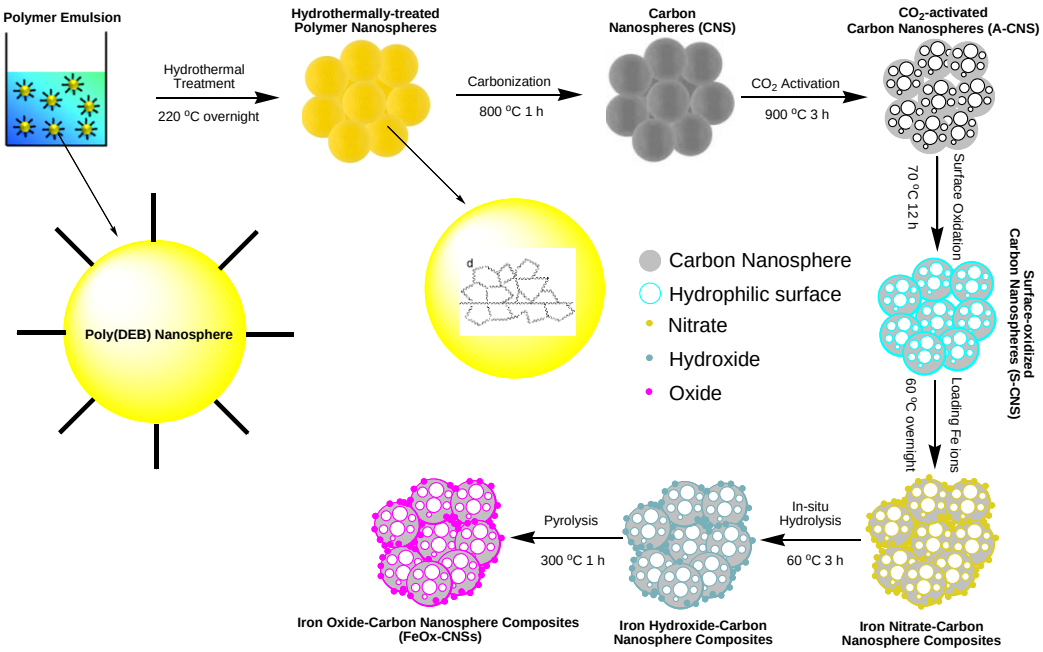

Scheme 2.1. Schematic synthesis of carbon nanosphere matrix and the FeO_x-CNS nancomposites.

Figure 2.1 shows TEM images of CNS, A-CNS, and S-CNS. CNS is comprised of aggregates of well-defined carbon nanospheres with average size of 24 nm (Figure 2.1(a)). Following the CO_2 activation, the nanosphere morphology is still well retained in A-CNS (Figure 2.1(b). The average nanosphere size in A-CNS is ca. 28 nm, which is slightly bigger than that in CNS, indicating the slight expansion of the carbon nanospheres due to mesopore/micropore generation within the nanospheres upon CO_2 activation. However, surface oxidation leads to slight structural collapse in S-CNS, with slightly deteriorated nanosphere morphology observed (Figure 2.1(c)).

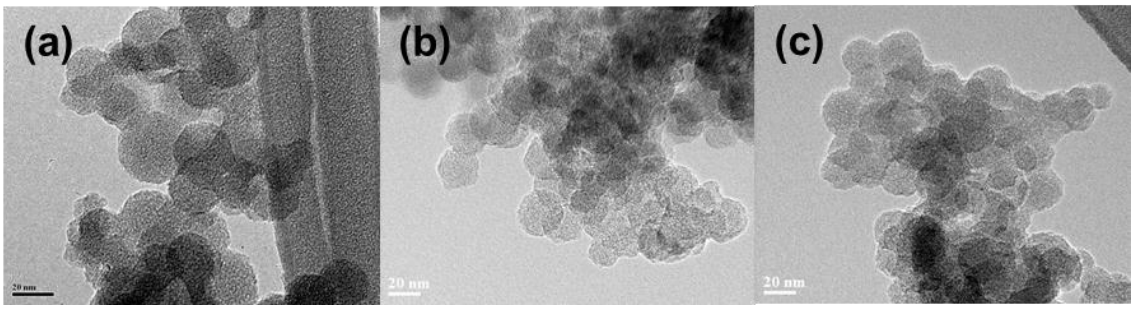

Figure 2.1. TEM of CNS (a), A-CNS (b), and S-CNS (c).

N_2 sorption analysis at 77 K was undertaken on the three carbon nanosphere samples to reveal their textural properties. Figure 2.2 shows their N_2 sorption curves, with the results summarized in Table 2.1. All three samples show typical type IV adsorption isotherm,[42] with a slight uptake at low relative pressure ($P/P_0 < 0.05$), and a sharp uptake at high relative pressure ($P/P_0 > 0.90$ for CNS and A-CNS; $P/P_0 > 0.7$ for S-CNS),

indicating that all samples contain predominantly mesopores/macropores. All samples have distinct type H3 hysteresis loops,[42] which is characteristic of slit-shaped pores. Relative to CNS, A-CNS has dramatically enhanced surface area (2,271 vs. 524 $m^2 g^{-1}$) and pore volume (5.18 vs. 0.84 $cm^3 g^{-1}$) with the generation of a large quantity of new mesopores/macropores upon CO_2 activation. However, upon further surface oxidation, the surface area and pore volume of S-CNS are reduced to 1073 $m^2 g^{-1}$ and 1.17 $cm^3 g^{-1}$, respectively, due to the slight unavoidable structural collapse. Despite this, the values are still high, making S-CNS suitable for the encapsulation of iron oxide.

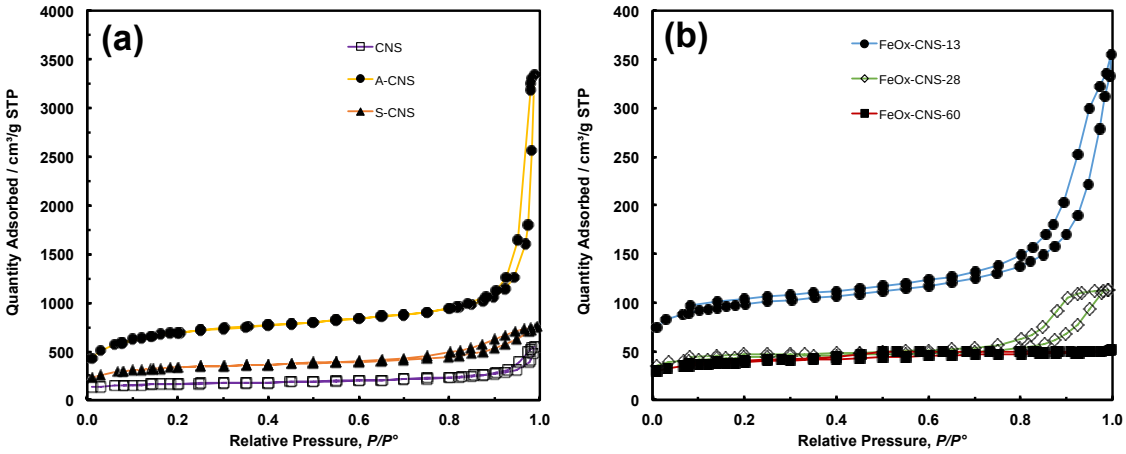

Figure 2.2. (a) N_2 sorption isotherm of CNS, A-CNS and S-CNS, (b) N_2 sorption isotherm of FeO_x-CNS-13, FeO_x-CNS-28 and FeO_x-CNS-60.

All the three carbon nanosphere samples should have the characteristic hierarchical pore structures with the presence of both inter-sphere mesopores/macropores

resulting from nanosphere aggregation/packing and intra-sphere micropores/mespores. They are predominantly mesoporous/macroporous, with micropores contributing to only 8–21% of total pore volume (see Table 2.1). Figure S2.2(a) compares their mesopore/macropore size distribution curves. S-CNS has a slightly reduced average mesopore/macropore size of 20 nm compared to CNS and A-CNS (32 and 41 nm, respectively). The 3-dimentional interconnected hierarchical mesopore/macropore structures of S-CNS, along with its high surface area and pore volume, is beneficial for rendering iron oxide composites with uniform encapsulation of iron oxide and in consequence high arsenic adsorption capacity.

Table 2.1. Results from N_2 sorption characterization.

Samples	Surface Area ($m^2\ g^{-1}$)[a]				Pore Volume ($cm^3\ g^{-1}$)[b]				$D_{meso/macro}$[c]
	S_{BET}	S_{micro}	$\%S_{micro}$	$S_{meso/macro}$	V_{total}	V_{micro}	$\%V_{micro}$	$V_{meso/macro}$	
CNS	524	292	56%	232	0.84	0.15	18%	0.69	32
A-CNS	2271	749	33%	1522	5.18	0.41	8%	4.77	41
S-CNS	1073	458	43%	615	1.17	0.25	21%	0.92	20
FeO_x-CNS-13	311	168	54%	143	0.55	0.09	16%	0.46	24
FeO_x-CNS-28	135	88	65%	47	0.22	0.05	23%	0.17	20
FeO_x-CNS-60	123	60	49%	63	0.08	0.03	38%	0.05	5

[a] BET surface area (S_{BET}), surface area of micropores (S_{micro}) and mesopores/macropores ($S_{meso/macro}$) determined with t-plot method; $\%S_{micro}$ denotes the percentage of surface area of micropores. [b] Total pore volume (V_{total}), micropore volume (V_{micro}) and mesopore/macropore volume ($V_{meso/macro}$) determined with t-plot method; $\%V_{micro}$ denotes the percentage of micropore volume. [c] Average mesopore/macropore size ($D_{meso/macro}$) determined from the N_2 desorption data with NLDFT model.

XPS characterization (see Figures S2.3 and S2.4) shows that S-CNS has a high content (22.8 atom%) of O, which is much higher than those (4.4 and 7.7 atom%, respectively) in CNS and A-CNS. Confirming the efficiency of surface oxidization, the high O content of S-CNS is beneficial for the subsequent even uniform encapsulation of iron oxide. Figure 2.3 compares their FTIR spectra. Both CNS and A-CNS show nearly featureless spectra, with only weak and broad bands in the frequency region of 1700−1000 cm^{-1} having two maxima at around 1570 cm^{-1} and 1149 cm^{-1}. The broad bands can be assigned to the stretching vibrations of C−C and C−H bonds in aromatic carbon rings, respectively.[43] In agreement with XPS results, new intense bands indicative of significant oxidation of the carbon surface are observed in the spectrum of S-CNS. The bands at 1733 and 1616 cm^{-1} can be assigned to asymmetric stretching vibrations of the newly formed –COOH carboxyl and −COO− carbonyl and/or –C=O ketone units.[41,44,45] The band at 1246 cm^{-1} can be attributed to asymmetric stretch of −C−C−C bridges in ketonic groups and/or to deformation vibrations of O−H in the carboxylic acid groups. In addition, the weak band at 667 cm^{-1} can be assigned to bending O−C−O vibrations of carboxyl units.[39]

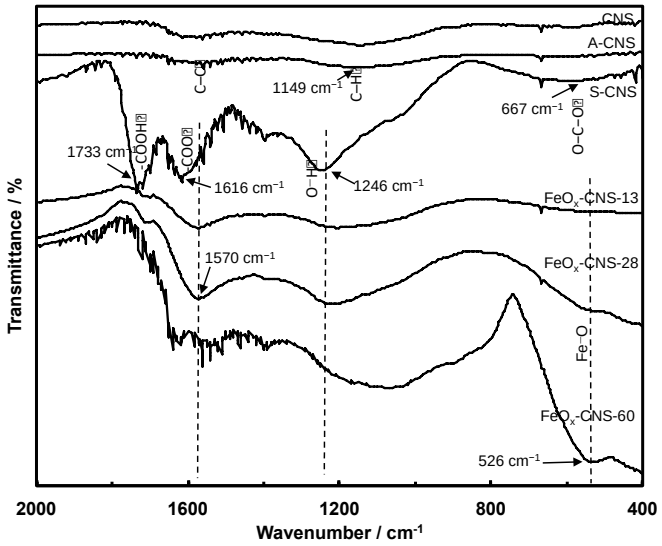

Figure 2.3. FTIR spectra of CNS, A-CNS, S-CNS, FeO_x-CNS-13, FeO_x-CNS-28, and FeO_x-CNS-60.

2.3.2 Synthesis and Characterization of FeO_x-CNS Nanocomposites

FeO_x-CNS nanocomposites were synthesized by loading iron nitrate precursors ($Fe(NO_3)_3 \bullet 9H_2O$) into the pore structures of S-CNS, followed with an in situ hydrolysis under ammonia atmosphere for the conversion of the iron nitrate precursors into hydroxides, and a pyrolysis step (at 300 ºC) for the transformation of the hydroxides into oxides (Fe_2O_3 and/or Fe_3O_4) and the release of porosity (see Scheme 1).[36,46] In order to investigate the effects of the iron oxide content on the arsenic adsorption efficiency, four composites with varying iron oxide content were synthesized by tuning the feed ratio of S-CNS and iron nitrate. Figure 2.4 shows the TGA curves of the resulting composites in an air atmosphere, along with those of CNS, A-CNS, and S-CNS for comparison. Among the three carbon materials (CNS, A-CNS, and S-CNS), CNS shows the best thermal stability in air given its highest C content. It starts to show weight loss at around 450 ºC

and has the complete weight loss at around 600 ºC with the peak weight loss at 587 ºC. A-CNS starts to lose weight at ca. 300 ºC and have complete weight loss at 500 ºC with peak weigh loss temperature of 470 ºC, due to its enhanced porosity and surface area for contact with air. S-CNS instead starts to lose weight at as early as 130 ºC and the weight loss covers a broad temperature range of 130 to 600 ºC, with the peak temperature of 560 ºC. The weight loss at the low temperature region is attributed to the loss of the labile oxygen-containing functionalities upon heating.

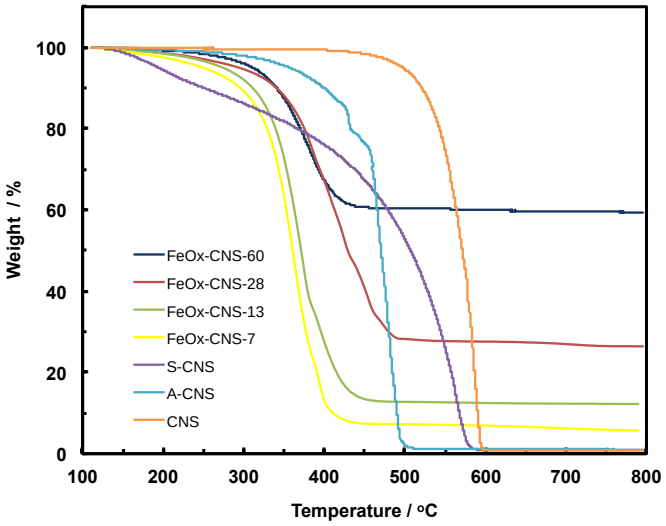

Figure 2.4. TGA curves of CNS, A-CNS, S-CNS, and FeO_x-CNS composites in air.

The FeO_x-CNS nanocomposites all show weight loss within the temperature range of 220–480 ºC, which should correspond primarily to the combustion of the carbon matrix. Their peak maximum temperature is within the range of 360–400 ºC, which is significantly reduced relative to that of S-CNS. This should be ascribed to the existence of iron oxide nanoparticles on the surfaces of the carbon matrix which act as catalysts for the carbon combustion since their exothermic oxidation takes place at lower

temperatures.[47] Different from the complete weight loss observed in the carbon samples, the composites show different residual char yield at 500 ºC (7, 13, 28, and 60 wt%, respectively), corresponding to the content of iron oxide within the nanocomposites. Consequently, these composites are termed as FeO_x-CNS-#, with the number representing the mass percentage of iron oxide in the composites.

The composites were characterized with XPS and FTIR for their spectroscopic properties. The XPS spectra of FeO_x-CNS-28 as the representative one are shown in Figures S2.3 and S2.4. Relative to S-CNS, FeO_x-CNS-28 has slightly reduced C and O content of 71.6 and 18.0 atom%, respectively, but with the significant presence of Fe at 4.0 atom%, confirming the incorporation of iron oxide. From its Fe_{2p} spectrum and the deconvoluted peaks (Figure S2.3(c)), both Fe^{3+} and Fe^{2+} species are present in the composite. In particular, the presence of Fe^{3+} species is confirmed by the $Fe_{2p3/2}$ peak at 712.58 eV and the associated satellite peak at 719.08 eV, $Fe_{2p1/2}$ peak at 726.18 eV and the satellite peak at 732.68 eV; the Fe^{2+} species is confirmed by the $Fe_{2p3/2}$ peak at 710.68 eV and the satellite peak at 715.78 eV, $Fe_{2p1/2}$ peak at 724.28 eV and the satellite peak at 729.38 eV (see Figure 2.3(c)).[48,49] The formation of Fe^{2+} can be attributed to the reducing ability of carbon matrix during the pyrolysis treatment in the synthesis.[15] In particular, the Fe^{3+}/Fe^{2+} ratio according to the $Fe_{2p3/2}$ peaks is estimated to be 1.57:1, which is close to the ratio of 2:1 for Fe_3O_4.[34] This indicates that the iron oxide present in the composite is primarily Fe_3O_4 and the presence of γ-Fe_2O_3 should be minor. The O_{1s} spectrum (Figure S2.4(a)) can be well fitted to three peaks at 530.3, 531.6, and 533.6 eV, which are attributed to the binding energies of oxygen atoms in the O–Fe, carboxyl O=C, and

hydroxyl O–H bonds, respectively.[50] The binding energy of C_{1s} can be found at 284.8, 286.1, 287.7, and 288.8 eV (Figure S2.4(b)), in agreement with the binding energy values of C–C, C–O, C=O and O–C=O reported in the literature.[51]

FTIR spectra of FeO_x-CNS-13, FeO_x-CNS-28, and FeO_x-CNS-60 are included in Figure 2.3. The basic bands attributed to the vibrations of aromatic carbon rings, carbonyl and ketone units are still observed, indicating that the carbon matrix retains the basic carbon structure and the main active groups of the parent S-CNS. The incorporation of iron oxide in the nanocomposites can be confirmed with a new broad band in the low frequency region (750−400 cm^{-1}) with the peak intensity at 526 cm^{-1} in FeO_x-CNS-28 and FeO_x-CNS-60 of significantly high iron oxide contents, which corresponds to the Fe–O vibration in Fe_3O_4 and γ-Fe_2O_3.[37]

Figure 2.5 shows the XRD spectra of two representative composites, FeO_x-CNS-13 and FeO_x-CNS-60, along with those of A-CNS and S-CNS. In the spectra of all samples, two weak but broad peaks (indicated by arrows), attributed to the (002) and (100) peaks of graphitic structures, are found at around 24 and 43º, respectively.[52] The weak and broad nature of the peaks suggests a low degree of graphitization with a low content of parallel single layers in these carbon materials, which is typical of amorphous carbon materials. Apart from the diffraction peaks of the carbon matrix, distinct diffractions arising from Fe_3O_4 and/or γ-Fe_2O_3 crystals (indicated by solid squares and open circles, respectively) can be clearly seen in the spectrum of FeO_x-CNS-60 having the highest iron oxide content. These peaks can be indexed to the diffractions of Fe_3O_4 (JCPDS Card No. 88–0315) and γ-Fe_2O_3 (JCPDS Card No. 39–1346), which are

indistinguishable.[15] Herein, given the minor presence of γ-Fe_2O_3 in the composite according to the XPS results above, these diffraction peaks should thus result predominantly from Fe_3O_4. The average crystallite size (L) is evaluated from the full width at half maximum of the (311) peak at 2θ = 35.5º according to the Scherrer equation:

$$L = \frac{K\lambda}{\beta cos\theta} \qquad (7)$$

where K is the shape factor usually assigned as 0.9, λ is the wavelength used (1.54 Å), and β is the full width at half-maximum (in rad) of the diffraction peak. The resulting L is about 8 nm. This size is much smaller than the size of large iron oxide aggregates seen under DF-STEM, indicating the polycrystalline nature of the aggregates. In the spectrum of FeO_x-CNS-13, characteristic peaks resulting from the iron oxide are not seen due to the low iron oxide content.

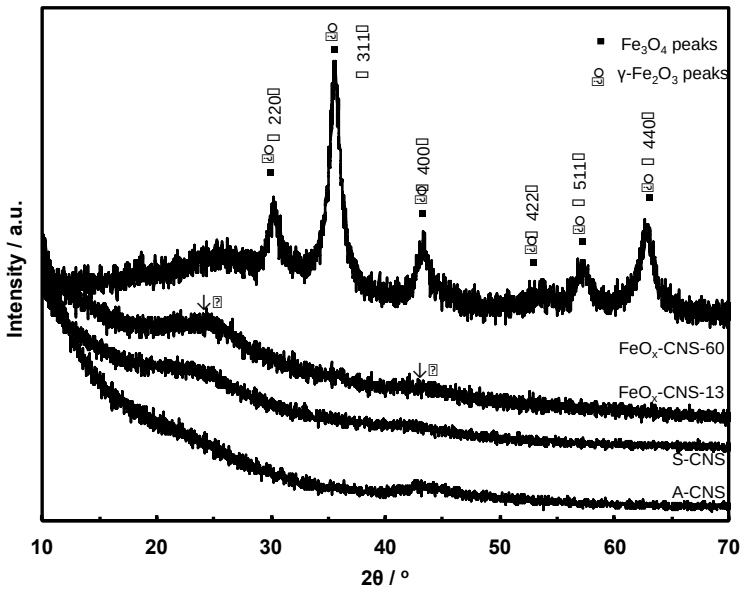

Figure 2.5. XRD patterns of A-CNS, S-CNS, FeO_x-CNS-13, and FeO_x-CNS-60.

TEM characterization of two representative composites, FeO_x-CNS-13 and FeO_x-CNS-60, was conducted, with typical TEM images shown in Figures 2.6 and S2.5, respectively. In FeO_x-CNS-13, some nanospheres can still be observed (see Figure 2.6(a)) though not as well defined as those in S-CNS. The presence of iron oxide nanoparticles in the composite can be confirmed from the high-resolution TEM (HRTEM) image shown in Figure 2.6(b). In particular, the inset in Figure 2.6(b) clearly demonstrates the crystalline lattices with a *d*-spacing of ~2.5 Å, which matches well the d_{311} of Fe_3O_4/γ-Fe_2O_3.[36] Figure 2.6(c) shows a dark-field scanning transmission electron microscopy (DF STEM) image of FeO_x-CNS-13. In DF-STEM images, heavy atoms such as Fe appear brighter compared to the light atoms (e.g., C or O). As shown in Figure 2.6(c), uniformly distributed bright spots with sizes of around 3–4 nm, corresponding to the iron oxide nanoparticles, can be found in the dark domain of FeO_x-CNS-13. The uniform dispersion of iron oxide nanoparticles in the carbon matrix is further confirmed by high-resolution elemental mapping for C, O, and Fe (Figure 2.6(d)–(f), respectively), where the C, O, and Fe elements are quite uniformly distributed and apparently correlated with the domain. Due to the significantly higher iron oxide content, the carbon nanosphere morphology is no longer observable in FeO_x-CNS-60 (see Figure S2.5(a)–(b)). Its DF STEM image (Figure S2.5(c)) reveals the much denser distribution of large iron oxide aggregates. Unlike the small interspersed nanoparticles seen in FeO_x-CNS-13, the iron oxide in FeO_x-CNS-60 forms the inter-connected networks within the pores of the carbon matrix. Nevertheless, overall uniform distribution of the iron oxide within the composite is still maintained in FeO_x-CNS-60 on the basis of the C, O, and Fe elemental maps (Figure S2.5(d)–(f)).

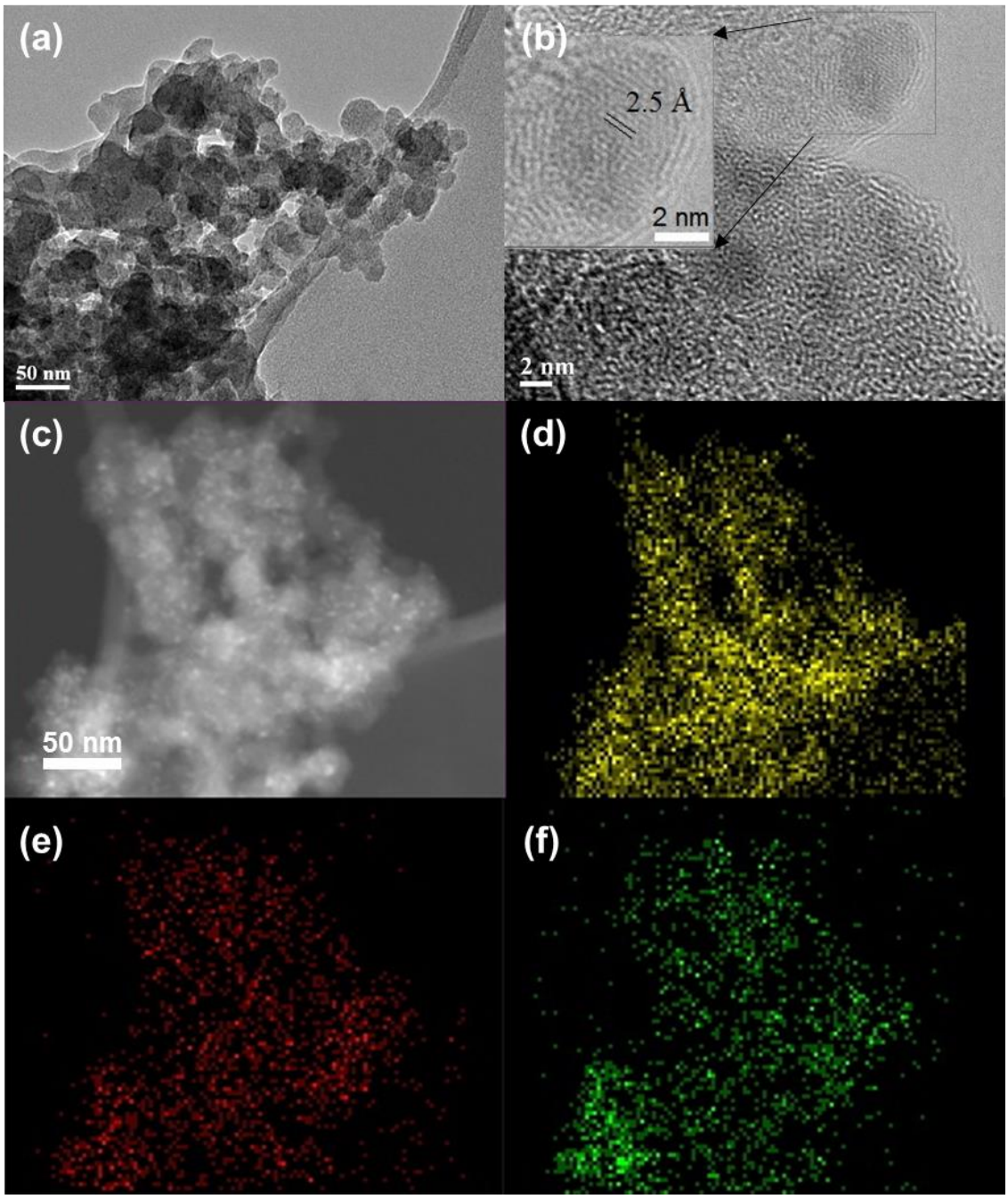

Figure 2.6. TEM (a), HRTEM images (b), DF-STEM image (c) and the corresponding C (d) O (e) and Fe (f) elemental maps of FeO_x-CNS-13.

With the increase of iron oxide content, the composites show continuously reduced N_2 sorption with much lowered surface area and pore volume relative to S-CNS

(see Figure 2.2(b) and Table 2.1). While both FeO_x-CNS-13 and FeO_x-CNS-28 still show the type IV isotherm with a hysteresis loop at the high relative pressure end (P/P_0: 0.8–1), FeO_x-CNS-60 of highest iron oxide content exhibits instead a type I isotherm with no distinct hysteresis loop observed (i.e., minor presence of mesopores/macropores). The surface area and pore volume decrease consistently from 311 $m^2 g^{-1}$ and 0.55 $cm^3 g^{-1}$ for FeO_x-CNS-13 to 135 $m^2 g^{-1}$ and 0.22 $cm^3 g^{-1}$ for FeO_x-CNS-28, and to 123 $m^2 g^{-1}$ and 0.03 $cm^3 g^{-1}$ for FeO_x-CNS-60. These results indicate the significant pore filling and blockage upon the encapsulation of iron oxide within the carbon matrix, which become increasingly severe with the increase of the iron oxide content. In particular, such filling and blockage are reasoned to be more prevalent within mesopores/macropores since the percentages of mesopore/macropore surface and volume decrease while those for micropores increase (see Table 2.1) upon the encapsulation of iron oxide relative to S-CNS.

2.3.3 Arsenic Adsorption with FeO_x-CNS Composites

A systematic investigation on the performance of the set of FeO_x-CNS composite adsorbents in arsenic adsorption has been undertaken. Batch equilibrium adsorption of both As(III) and As(V) was carried out at the initial arsenic concentrations of 50–2,000 mg L^{-1} for As(III) (at pH = 8) and 50–1,000 mg L^{-1} for As(V) (at pH = 3). The specific pH values are chosen herein since the composite adsorbents show optimum arsenic adsorption at the conditions according to the study on the effect of pH below. Figure 2.7 shows the adsorption isotherms of the various composites, as well as those of A-CNS and S-CNS as control samples, at 23 ºC. The two control carbon nanosphere samples without

containing iron oxide show similar isotherms for both As(III) and As(V), with S-CNS having slightly raised isotherms relative to A-CNS possibly due to its more hydrophilic surface. For the composites, the content of iron oxide shows a dramatic effect on their arsenic adsorption. Relative to the carbon samples, the incorporation of iron oxide at 7 and 13 wt% in FeO_x-CNS-7 and FeO_x-CNS-13 leads to significantly improved arsenic adsorption with increasingly raised isotherms for both As(III) and As(V). However, the further increase of iron oxide content to higher values of 28 and 60 wt% instead lowers the isotherms, which become close to those of the two control samples.

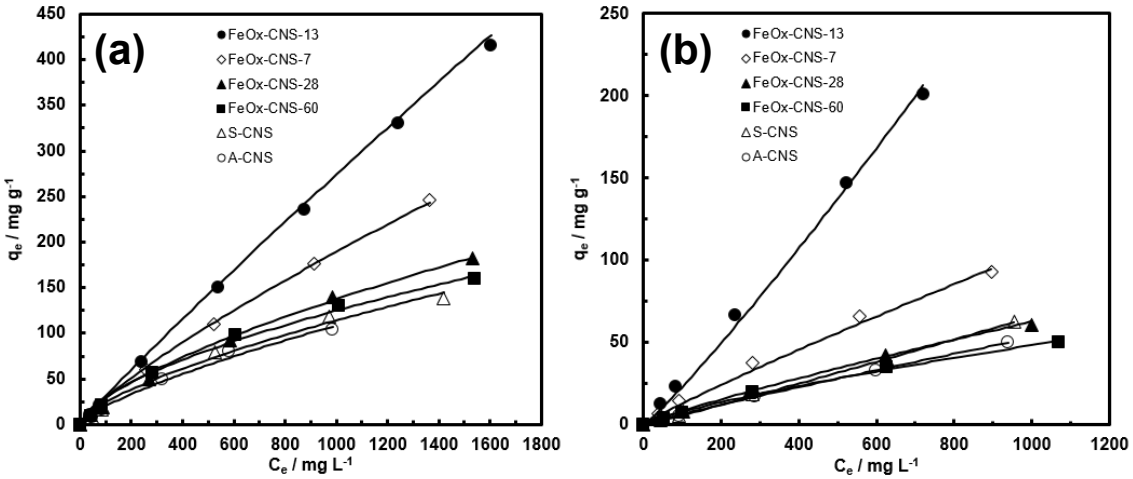

Figure 2.7. (a) As(III) adsorption isotherms (at pH = 8) and (b) As(V) adsorption isotherms (at pH = 3) of A-CNS, S-CNS, and FeO_x-CNS composites. The adsorption isotherms are fitted the Freundlich adsorption model (solid line).

All the isotherms have been found to well follow Freundlich adsorption model (Equation 1) with R^2 values close to 1 (see Table S2.1). The Langmuir model instead does not give good fitting with low R^2 values. The adsorption capacity data (q_{max}), taken from the last point in each isotherm (i.e., highest adsorption uptake in each isotherm), are

summarized in Table S2.2. With any given adsorbent herein, we find that the adsorption capacity for As(III) is always higher than that for As(V). This is beneficial and desirable because of the prevalence of more toxic As(III) in groundwater and wastewater.[1] The two carbon nanosphere samples, A-CNS and S-CNS, show q_{max} of 104 and 138 mg g^{-1}, respectively, for As(III) and 50 and 63 mg g^{-1}, respectively, for As(V). These q_{max} data are significantly higher than the values reported for various activated carbons within the similar range of initial arsenic concentration,[53] possibly due to the much higher accessible surface area of the carbon nanosphere samples as a result of their hierarchical pore structures.

The two composites having relatively low iron oxide contents, FeO_x-CNS-7 and FeO_x-CNS-13, show dramatically enhanced adsorption capacity, 246 and 416 mg g^{-1}, respectively, for As(III), and 93 and 201 mg g^{-1}, respectively, for As(V). In our best knowledge, the As(III) adsorption capacity of 416 mg g^{-1} for FeO_x-CNS-13 is by far the highest among the various iron oxide-based adsorbents (see Table 2.2). It is even higher than the value of 320 mg g^{-1} for a high-performance γ-Fe_2O_3-macroporous silica composite adsorbent reported by Yu et al.[39] Meanwhile, the As(V) adsorption capacity of 201 mg g^{-1} FeO_x-CNS-13 is also comparable to some best values (up to 248 mg g^{-1}; see Table 2.2) reported.[39] These capacity data are remarkable given the encapsulation of iron oxide at such low contents. Clearly, the small non-aggregated iron oxide nanoparticles interspersed uniformly on the porous carbon nanosphere matrix contribute to the dramatic enhancement in the adsorption capacity since their surface is more active than the carbon surface for arsenic adsorption. Increasing the iron oxide content within this range (< ca.

13 wt%) is thus beneficial for enhanced capacity. From the summary data of fitted parameters of the arsenic adsorption equilibrium on FeOx-CNS showed in Table S2.1, we can find that the parameter n of FeO_x-CNS-13 gotten from Freundlich model is 1.06, closer to 1 compared with other composites, which means FeO_x-CNS-13 has highest homogeneity. As reported, the parameter n could be regarded as the parameter characterising the system heterogeneity. [58] The parameter n is usually greater than unity, and therefore the larger is this parameter the more heterogeneous is the system. This can also explain the reason why FeO_x-CNS-13 has highest arsenic adsorption capacity.

Table 2.2. Comparison of arsenic adsorption capacity data of representative iron oxide-based adsorbents.

Iron oxide-based adsorbents	Adsorption capacity ($mg\ g^{-1}$)		Reference
	As(III)	As(V)	
Fe_3O_4 nanoparticles (12 nm)	160	180	11
Fe_2O_3 CAHNs		137.5	14
Flowerlike α-Fe_2O_3		51	13
Hollow Nestlike α-Fe_2O_3	58.6	75.3	19
γ-Fe_2O_3 nanochains		162	20
bimetal iron(III)–titanium(IV) oxide	85	14.3	6
Fe-Cu binary oxide	122.3	82.7	54
Hollow Fe-Ce Alkoxides	266	206	56
Fe_3O_4-RGO	13.1	5.83	23
Fe_2O_3-Graphene nanoplatelet	11.34		27
Fe_2O_3-cellulose	23.16	32.11	35
Fe_2O_3-ordered mesoporous carbon	29.4	17.9	36
Ce–Fe oxide@carbon nanotube	28.74	30.96	38
Fe_2O_3-carbon aerogel		216	56
Fe_2O_3-diatomite	60.65	81.16	57
Fe_2O_3-macroporous silica	320	248	39
FeO_x-CNS-13	**416**	**201**	**This study**

Relative to FeO_x-CNS-13, the other two composites, FeO_x-CNS-28 and FeO_x-CNS-60, instead show much deteriorated adsorption capacity data (182 and 160 $mg\ g^{-1}$,

respectively, for As(III); 61 and 50 mg g^{-1}, respectively, for As(V)) despite the higher iron oxide contents. Within this range of iron oxide content (ca. 28–60 wt%), the increase in iron oxide content is detrimental to arsenic adsorption. This should result from the formation of large iron oxide aggregates, which leads to filled/blocked pores and reduced active surface area for effective arsenic adsorption. Clearly, 13 wt% is approximately the optimum iron oxide content for this range of composite adsorbents. A similar trend of change in arsenic adsorption capacity has been noted in iron-impregnated granular activated carbon adsorbents, where the adsorption capacity increases with the iron content up to 6% and then decreases with further increase in the content.[22]

The adsorption kinetics of FeO_x-CNS-13 was monitored at the initial arsenic concentration of 950 mg L^{-1} for As(III) (at pH = 8) and 800 mg L^{-1} for As(V) (at pH = 3). Figure 2.8 shows the kinetic curves. For both curves, the adsorption can be divided into two stages, a rapid uptake within the first 30 min of contact and a slow uptake thereafter until equilibrium is reached. In particular, the majority of the arsenic uptake, 62 and 73% for As(III) and As(V), respectively, occurs within the first 30 min, indicating the very fast adsorption rate. The adsorption kinetics can be perfectly fitted with a pseudo-second-order model (Equation 2 or 3) with the rate constant k_2 of 0.000315 and 0.000504 g mg^{-1} min^{-1} for As(III) and As(V), respectively. The k_2 values are high, in particular for As(III), when compared to other superior adsorbents reported in the literature. For example, the high-performance γ-Fe_2O_3-macroporous silica composite adsorbent reported by Yu et al. has the k_2 values of 0.00015 and 0.0014 g mg^{-1} min^{-1} for As(III) and As(V), respectively, under similar conditions.[39] These kinetic results demonstrate that, within the

concentration ranges, the rapid removal of the arsenic species from wastewater can be achieved with FeO_x-CNS-13.

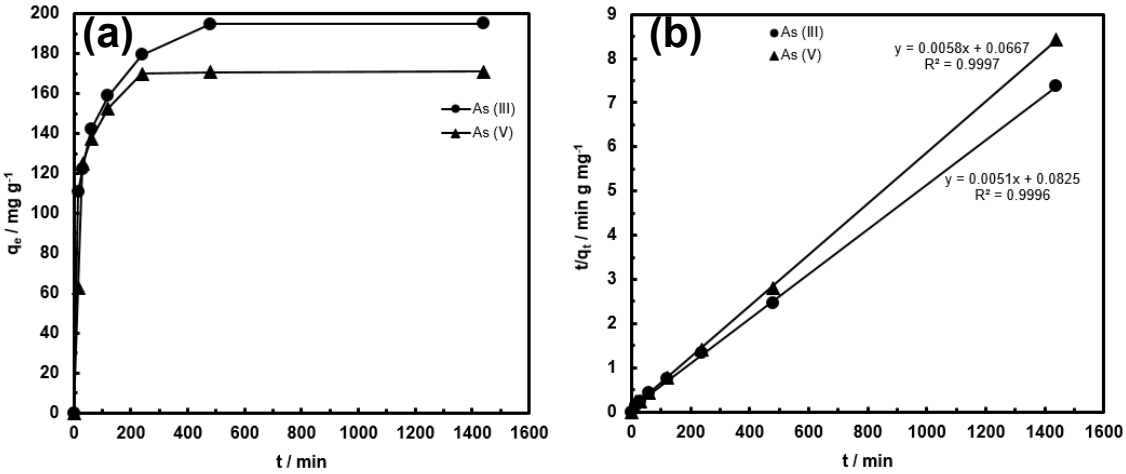

Figure 2.8. (a) As(III) and As(V) adsorption kinetic curves of FeO_x-CNS-13; (b) fitting of the kinetic data with the pseudo-second-order model.

It is expected that the pH of the aqueous medium should have a crucial influence on arsenic removal by the composite adsorbents, because it greatly affects the surface charge of the composites and arsenic species distribution.[1-4] Thus, the adsorption of arsenic with FeO_x-CNS-13 as a function of pH in a broad range has been investigated. Figure 2.9 plots q_e as a function of pH (within 2–10), which was undertaken at the initial As(III) and As(V) concentration of 1,000 mg L^{-1} and the contact time of 24 h. Clearly, arsenic adsorption with FeO_x-CNS-13 is strongly pH-dependent. With the increase of pH from 2 to 10, the As(V) uptake capacity remains nearly constant at 197–200 mg g^{-1} in the range of 2–4, followed with the continuous drop to 150 mg g^{-1} at pH = 10. The As(III) uptake shows an opposite trend. The maximum As(III) uptake (230 mg g^{-1}) is found at

pH = 8. Both increasing and decreasing the pH value lead to the reduction in adsorption capacity.

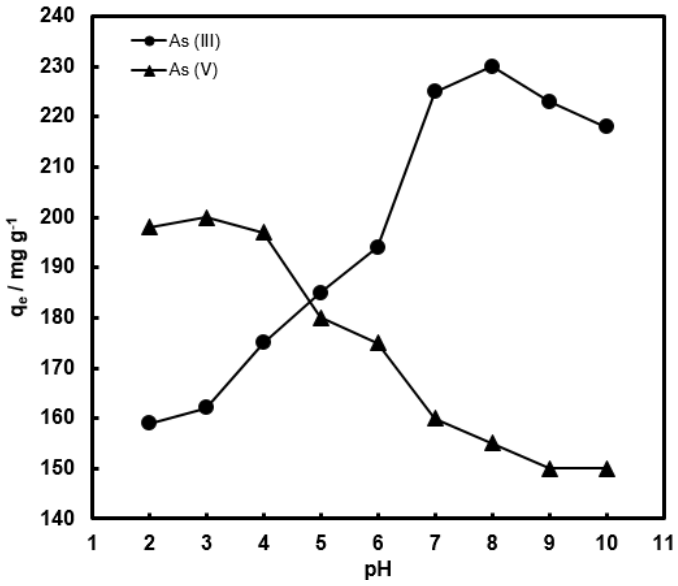

Figure 2.9. Arsenic uptake of FeO_x-CNS-13 as a function of pH. The initial arsenic concentration is 1,000 mg L^{-1}.

Similar trends of change have commonly been observed with various iron oxide-based adsorbents and can be explained by the changes in surface charge of the adsorbents and the arsenic speciation.[7-9,12,21-24,26,32,35,38,39] The point of zero charge (pH_{PZC}) of FeO_x-CNS-13 is measured to be ≈ 2.8 (Figure S2.6(a)). The surface of FeO_x-CNS-13 is positively charged at pH < pH_{PZC}, and in the pH range of 2–2.8, the predominant species of As(V) is $H_2AsO_4^-$ with negative charge.[2] The electrostatic interaction between positively charged FeO_x-CNS-13 and negatively charged As(V) species results in the enhanced adsorption within this pH range. The deprotonation of surface hydroxyl groups occurs with the increase of pH, leading to a negatively charged surface for FeO_x-CNS-13

after pH of 2.8, and the predominant species of As(V) is $H_2AsO_4^-$ from pH 3–6.5, and $HAsO_4^{2-}$ from after pH of 6.5, both with negative charge. It thus results in the reduced As(V) adsorption uptake. However, the adsorption of As(III) on FeO_x-CNS-13 is different. The optimum pH for As(III) adsorption is 8. When the pH value is below 8, the arsenic removal efficiency significantly increases with the increase of pH, but decreases when pH is above 8. The solubilization and leaching of Fe species into the acidic solution at pH 2–6 (Figure S2.6(b)) is the primary reason for the reduced As(III) adsorption capacity with the decrease of pH in this range.[23] At pH < 9.2, As(III) exists mainly as H_3AsO_3,[2] indicating As(III) is adsorbed on FeO_x-CNS-13 through a surface complexation mechanism.[23] The removal efficiency drops at pH > 9 due to the ionization of H_3AsO_3 to $H_2AsO_3^-$ with negative charge, which results in the occurrence of more competition between arsenite and OH^- anions. Moreover, the increasing Coulombic repulsion between As(III) species and the negative surface of FeO_x-CNS-13 may be another important reason for the decrease in As(III) uptake when pH > 9.

2.4 Conclusion

A set of FeO_x-CNS nanocomposite adsorbents has been successfully synthesized by encapsulating iron oxide at different content (7–60 wt%) into a high-surface-area high-pore-volume carbon nanosphere matrix with hierarchical pore structure, S-CNS. Detailed characterizations of the nanocomposites have been undertaken. TEM results reveal the overall uniform distribution of the crystalline iron oxide within the nanocomposites. In FeO_x-CNS-13, small iron oxide nanoparticles with sizes of 3–4 nm are interspersed

uniformly on the carbon nanosphere matrix, with the retention of the hierarchical pore structures. On the contrary, aggregates of iron oxide are observed in FeO_x-CNS-60 with severe pore filling and blockage. XPS and XRD results indicate that the iron oxide species is primarily crystalline Fe_3O_4. The adsorption of both As(III) and As(V) has been investigated with the nanocomposites. Best adsorption performance is achieved with FeO_x-CNS-13 having the optimum iron oxide content, with superior adsorption capacity of 416 and 201 mg g^{-1} for As(III) and As(V), respectively, which are highest or among the highest reported thus far in the literature. Both reducing and increasing the iron oxide content lead to the reduced arsenic adsorption. Meanwhile, from the adsorption kinetics, FeO_x-CNS-13 is also featured with high adsorption rate. The results confirm the high potential of FeO_x-CNS-13 as superior adsorbents for arsenic removal from industrial wastewater streams.

2.5 References

(1) W. R. Cullen and K. J. Reimer, *Chem. Rev.*, 1989, **89**, 713–764.

(2) P. L. Smedley and D. G. Kinniburgh, *Appl. Geochem.*, 2002, **17**, 517–568.

(3) D. Mohan and C. U. Pittman Jr., *J. Hazard. Mater.*, 2007, **142**, 1–53.

(4) T. S. Y. Choong, T. G. Chuah, Y. Robiah, F. L. G. Koay and I. Azni, *Desalination*, 2007, **217**, 139–166.

(5) S. C. N. Tang and I. M. C. Lo, *Water Res.*, 2013, **47**, 2613–2632.

(6) M. L. Pierce and C. B. Moore, *Water Res.*, 1982, **16**, 1247–1253.

(7) K. P. Raven, A. Jain and R. H. Loeppert, *Environ. Sci. Technol.*, 1998, **32**, 344–349.

(8) S. Dixit and J. G. Hering, *Environ. Sci. Technol.*, 2003, **37**, 4182–4189.

(9) S. Luther, N. Borgfeld, J. Kim and J. G. Parsons, *Microchem. J.*, 2012, **101**, 30–36.

(10) S. Yean, L. Cong, C. T. Yavuz, J. T. Mayo, W. W. Yu, A. T. Kan, V. L. Colvin and M. B. Tomson, *J. Mater. Res.*, 2005, **20**, 3255–3264.

(11) C. T. Yavuz, J. T. Mayo, W. W. Yu, A. Prakash, J. C. Falkner, S. Yean, L. Cong, H. J. Shipley, A. Kan, M. Tomson, D. Natelson and V. L. Colvin, *Science*, 2006, **314**, 964–967.

(12) T. Tuutijärvi, J. Lu, M. Sillanpää and G. Chen, *J. Hazard. Mater.*, 2009, **166**, 1415–1420.

(13) L.-S. Zhong, J.-S. Hu, H.-P. Liang, A.-M. Cao, W.-G. Song and L.-J. Wan, *Adv. Mater.*, 2006, **18**, 2426–2431.

(14) F. Mou, J. Guan, Z. Xiao, Z. Sun, W. Shi and X.-A. Fan, *J. Mater. Chem.*, 2011, **21**, 5414–5421.

(15) F. Mou, J. Guan, H. Ma, L. Xu and W. Shi, *ACS Appl. Mater. Interfaces*, 2012, **4**, 3987–3993.

(16) C.-Y. Cao, J. Qu, W.-S. Yan, J.-F. Zhu, Z.-Y. Wu and W.-G. Song, *Langmuir*, 2012, **28**, 4573–4579.

(17) B. Wang, H. Wu, L. Yu, R. Xu, T.-T. Lim and X. W. Lou, *Adv. Mater.*, 2012, **24**, 1111–1116.

(18) T. Wang, L. Zhang, H. Wang, W. Yang, Y. Fu, W. Zhou, W. Yu, K. Xiang, Z. Su, S. Dai and L. Chai, *ACS Appl. Mater. Interfaces*, 2013, **5**, 12449–12459.

(19) Z. Wei, R. Xing, X. Zhang, S. Liu, H. Yu and P. Li, *ACS Appl. Mater. Interfaces*, 2013, **5**, 598–604.

(20) G. K. Das, C. S. Bonifacio, J. De Rojas, K. Liu, K. van Benthem and I. M. Kennedy, *J. Mater. Chem. A.*, 2014, **2**, 12974–12981.

(21) M. Jang, S.-H. Min, T.-H. Kim and J. K. Park, *Environ. Sci. Technol.*, 2006, **40**, 1636–1643.

(22) Z. Gu, J. Fang and B. Deng, *Environ. Sci. Technol.*, 2005, **39**, 3833–3843.

(23) V. Chandra, J. Park, Y. Chun, J. W. Lee, I.-C. Hwang and K. S. Kim, *ACS Nano*, 2010, **4**, 3979–3986.

(24) K. Zhang, V. Dwivedi, C. Chi and J. Wu, *J. Hazard. Mater.*, 2010, **182**, 162–169.

(25) X.-L. Wu, L. Wang, C.-L. Chen, A.-W. Xu and X.-K. Wang, *J. Mater. Chem.*, 2011, **21**, 17353–17359.

(26) G. Sheng, Y. Li, X. Yang, X. Ren, S. Yang, J. Hu and X. Wang, *RSC Adv.*, 2012, **2**, 12400–12407.

(27) J. Zhu, R. Sadu, S. Wei, D. H. Chen, N. Haldolaarachchige, Z. Luo, J. A. Gomes, D. P. Young and Z. Guo, *ECS J. Solid State Sci. Techn.*, 2012, **1**, M1–M5.

(28) J. Zhu, S. Wei, H. Gu, S. B. Rapole, Q. Wang, Z. Luo, N. Haldolaarachchige, D. P. Young and Z. Guo, *Environ. Sci. Technol.*, 2012, **46**, 977–985.

(29) Y. Wang, Q. He, H. Qu, X. Zhang, J. Guo, J. Zhu, G. Zhao, H. A. Colorado, J. Yu, L. Sun, S. Bhana, M. A. Khan, X. Huang, D. P. Young, H. Wang, X. Wang, S. Wei and Z. Guo, *J. Mater. Chem. C*, 2014, **2**, 9478–9488.

(30) G. Gollavelli, C.-C. Chang and Y.-C. Ling, *ACS Sustainable Chem. Eng.*, 2013, **1**, 462–472.

(31) B. Paul, V. Parashar and A. Mishra, *Environ. Sci.: Water Res. Technol.*, 2015, **1**, 77–83.

(32) F. Yu, S. Sun, J. Ma and S. Han, *Phys. Chem. Chem. Phys.*, 2015, **17**, 4388–4397.

(33) J. Ding, B. Li, Y. Liu, X. Yan, S. Zeng, X. Zhang, L. Hou, Q. Cai and J. Zhang, *J. Mater. Chem. A*, 2015, **3**, 832–839.

(34) H. Su, Z. Ye and N. Hmidi, manuscript submitted.

(35) X. Yu, S. Tong, M. Ge, J. Zuo, C. Cao and W. Song, *J. Mater. Chem. A*, 2013, **1**, 959–965.

(36) Z. Wu, W. Li, P. A. Webley and D. Zhao, *Adv. Mater.*, 2012, **24**, 485–491.

(37) M. Baikousi, A. B. Bourlinos, A. Douvalis, T. Bakas, D. F. Anagnostopoulos, J. Tucek, K. Safarova, R. Zboril and M. A. Karakassides, *Langmuir*, 2012, **28**, 3918–3930.

(38) B. Chen, Z. Zhu, J. Ma, Y. Qiu and J. Chen, *J. Mater. Chem. A*, 2013, **1**, 11355–11367.

(39) J. Yang, H. Zhang, M. Yu, I. Emmanuelawati, J. Zou, Z. Yuan and C. Yu, *Adv. Funct. Mater.*, 2014, **24**, 1354–1363.

(40) V. Tiwari, Z. Chen, M. Grundy, Z. Ye, F. Gao, Z. Gu, manuscript submitted.

(41) Z. Wu, P. Webley and D. Zhao, *Langmuir*, 2010, **26**, 10277–10286.

(42) K. S. W. Sing, D. H. Everett, R. A. W. Haul, L. Moscou, R. A. Pierotti, J. Rouquerol and T. Siemieniewska, *Pure Appl. Chem.*, 1985, **57**, 603–619.

(43) A. Dandekar, R. Baker and M. Vannice, *Carbon*, 1998, **36**, 1821−1831.

(44) P. Bazula, A. Lu, J. Nitz and F. Schüth, *Microporous Mesoporous Mater.*, 2008, **108**, 266−275.

(45) A. Kuznetsova, D. Mawhinney, V. Naumenko, J. Yates, J. Liu and R. Smalley, *Chem. Phys. Lett.*, 2000, **321**, 292−296.

(46) Z. Wu, Q. Li, D. Peng, P. Webley and D. Zhao, *J. Am. Chem. Soc.*, 2010, **132**, 12042–12050.

(47) G. Ennas, G. Marongiu and A. Musinu, *J. Mater. Res.*, 1998, **14**, 1570–1578.

(48) H. Kong, J. Song and J. Jang, *Chem. Commun.*, 2010, **46**, 6735–6737.

(49) G. Bhargava, I. Gouzman, C. Chun, T. Ramanarayanan and S. Bernasek, *Appl. Surf. Sci.*, 2007, **253**, 4322–4329.

(50) R. Netterfield, P. Martin, C. Pacey, W. Sainty, D. Mckenzie and G. Auchterlonie, *Appl. Phys.*, 1989, **66**, 1805–1809.

(51) S. Chao, Y. Takagi, G. Lucovsky, P. Pai, R. Custer, J. Tyler and J. Keem, *Appl. Surf. Sci.*, 1986, **26**, 575–583.

(52) L. Xu, J.-W. McGraw, F. Gao, M. Grundy, Z. Ye, Z. Gu and J. Shepherd, *J. Phys. Chem. C*, 2013, **117**, 10730–10742.

(53) J. Pattanayak, K. Mondal, S. Mathew and S. B. Lalvani, *Carbon*, 2000, **38**, 589–596.

(54) G. Zhang, Z. Ren, X. Zhang and J. Chen, *Water Res.*, 2013, **47**, 4022–4031.

(55) B. Chen, Z. Zhu, S. Liu, J. Hong, J. Ma, Y. Qiu and J. Chen, *ACS Appl. Mater. Interfaces*, 2014, **6**, 14016−14025.

(56) Y. Lin and J. Chen, *J. Colloid Interface Sci.*, 2014, **420**, 74–79.

(57) Y. Du, H. Fan, L. Wang, J. Wang, J. Wu and H. Dai, *J. Mater. Chem. A*, 2013, **1**, 7729–7737.

(58) D.D. Do, *Adsorption Analysis: Equilibria and Kinetics ICP*, London, UK, 1998, 50-59.

2.6 Supporting Information

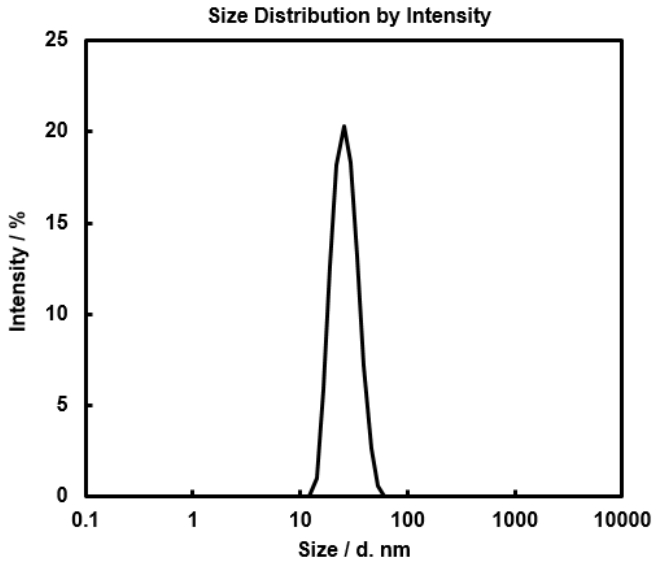

Figure S2.1. Size distribution (average size: 27 nm; PDI: 0.19) of poly(DEB) polymer nanospheres obtained by miniemulsion polymerization by DLS measurement.

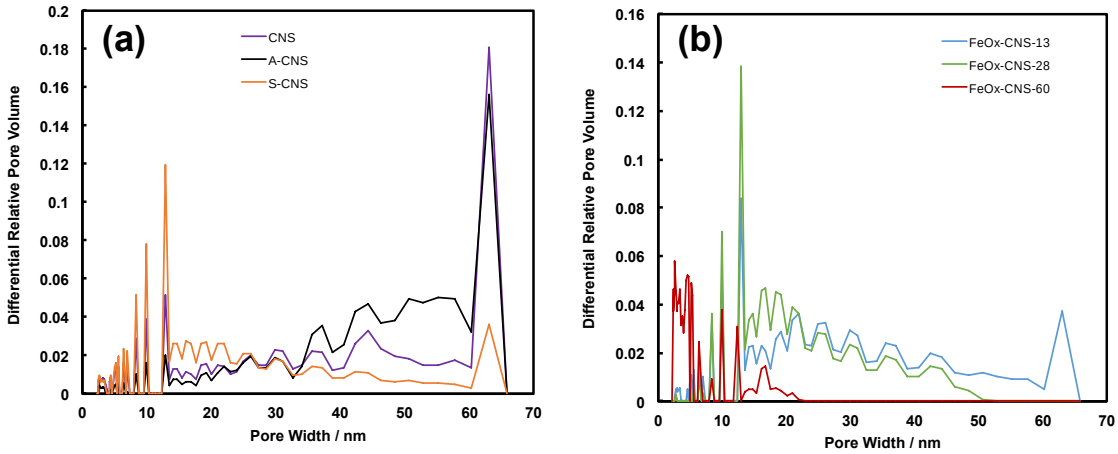

Figure S2.2. Mesopore/macropore size distributions (obtained by DFT model) of (a) CNS, A-CNS, and S-CNS; (b) three FeO_x-CNS composites.

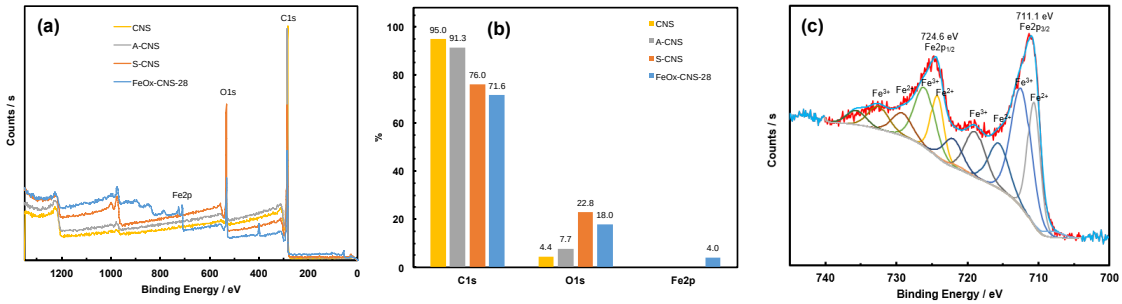

Figure S2.3. (a) XPS survey scan of CNS, A-CNS, S-CNS, and FeO_x-CNS-28; (b) The content of C, O, and Fe in CNS, A-CNS, S-CNS, and FeO_x-CNS-28 determined by XPS; (c) high-resolution Fe_{2p} spectra of FeO_x-CNS-28.

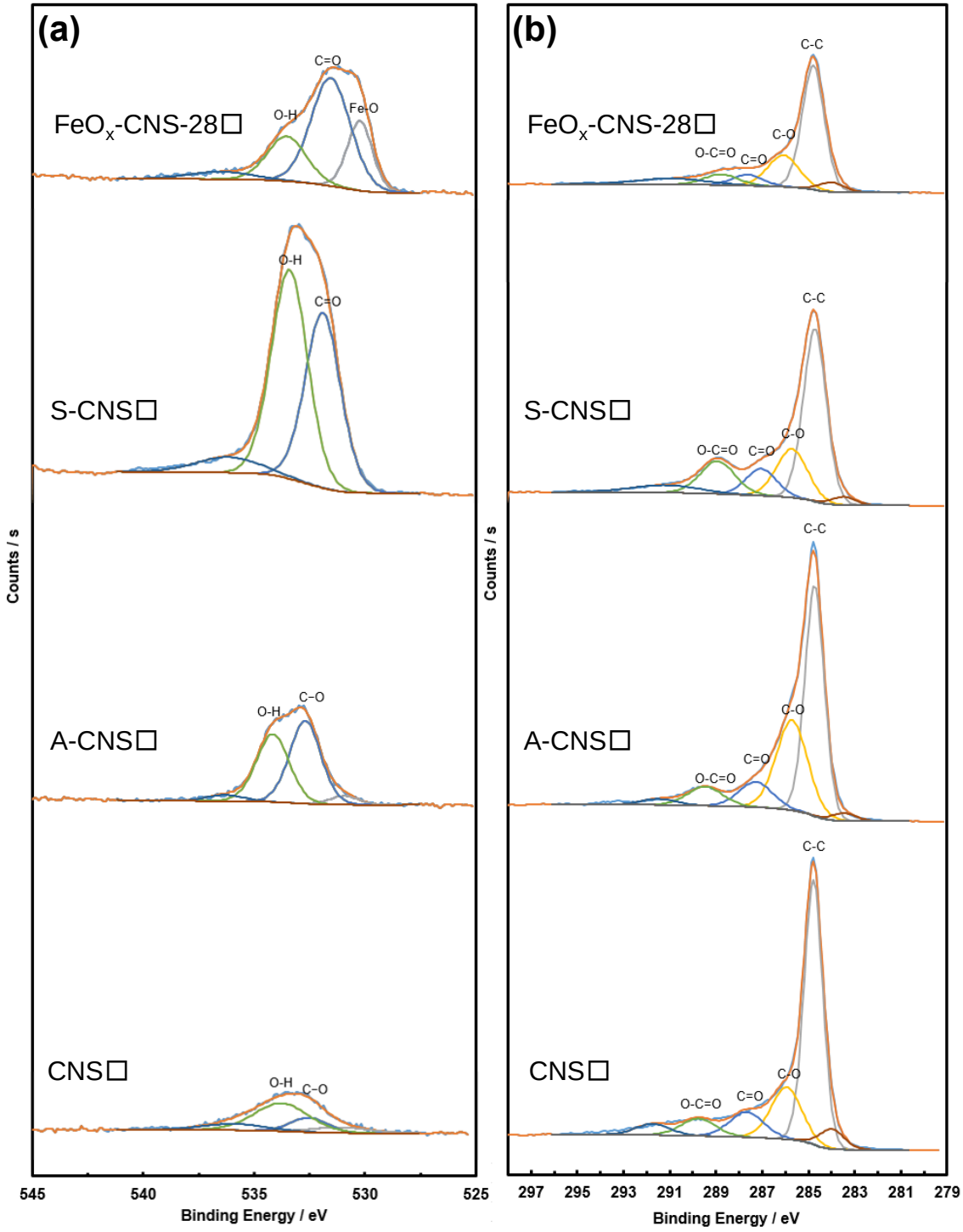

Figure S2.4. The O_{1s} (a) and C_{1s} (b) spectra of CNS, A-CNS, S-CNS and FeO_x-CNS-28.

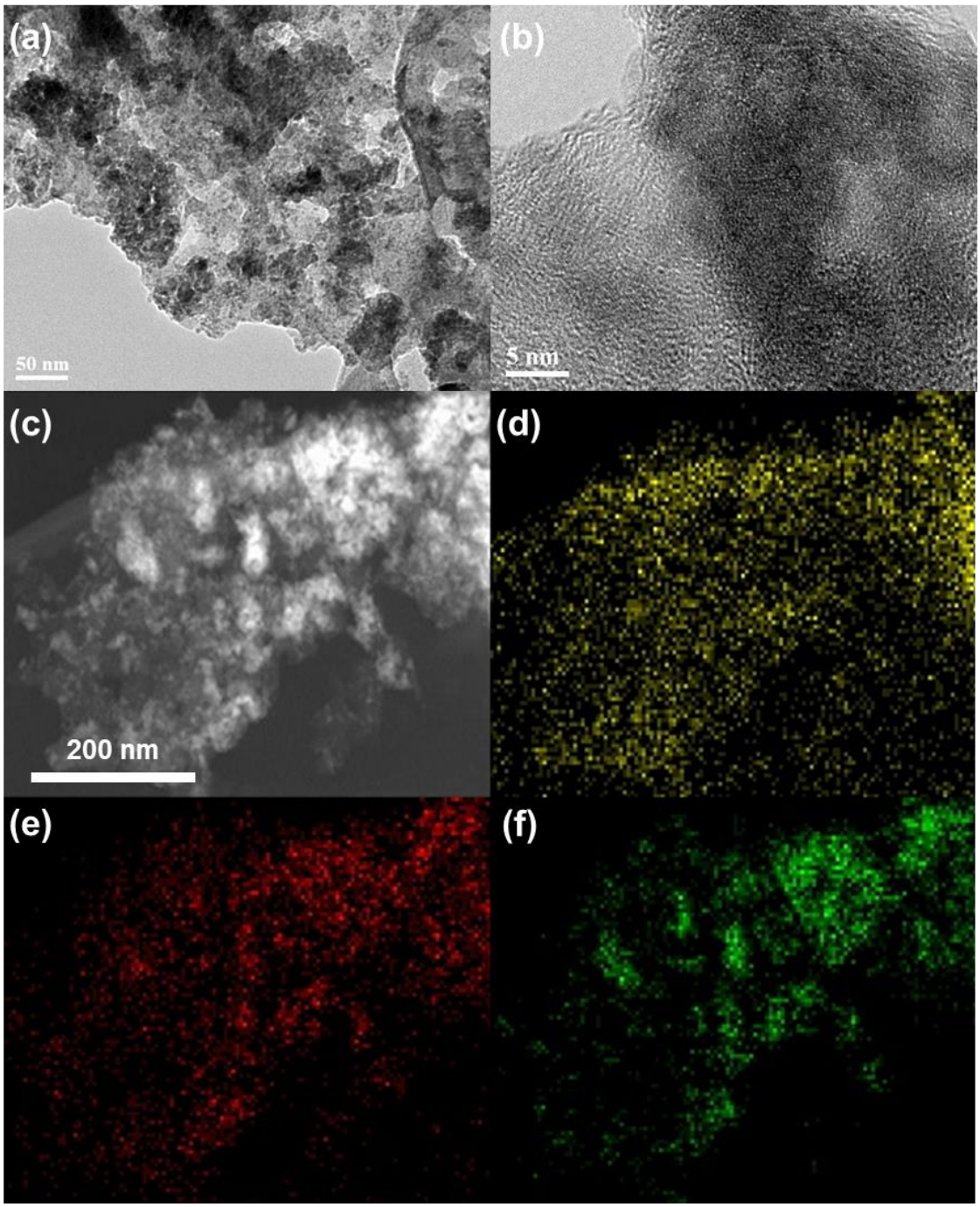

Figure S2.5. TEM (a), HRTEM images (b), DF-STEM image (c) and the corresponding C (d) O (e) and Fe (f) elemental maps of FeO_x-CNS-60.

Table S2.1. A summary of the fitted parameters of the arsenic adsorption isotherms and kinetics.

Samples	Freundlich model			Pseudo-second-order kinetic model			
As(III)	R^2	n	k ($mg^{(1-n)}$ L^n g^{-1})	R^2	k_2 (g mg^{-1} min^{-1})	V_0 (mg g^{-1} min^{-1})	q_{eq} (mg g^{-1})
A-CNS	0.988	1.36	0.676				
S-CNS	0.987	1.48	1.073				
FeO_x-CNS-7	0.996	1.23	0.694				
FeO_x-CNS-13	0.992	1.06	0.414	1.000	0.0003	12.1	196
FeO_x-CNS-28	0.996	1.48	1.307				
FeO_x-CNS-60	0.998	1.63	1.780				

Samples	Freundlich model			Pseudo-second-order kinetic model			
As(V)	R^2	n	k ($mg^{(1-n)}$ L^n g^{-1})	R^2	k_2 (g mg^{-1} min^{-1})	V_0 (mg g^{-1} min^{-1})	q_{eq} (mg g^{-1})
A-CNS	1.000	1.10	0.098				
S-CNS	0.999	0.96	0.048				
FeO_x-CNS-7	0.994	1.10	0.203				
FeO_x-CNS-13	0.995	0.90	0.140	1.000	0.0005	15.0	172
FeO_x-CNS-28	0.992	1.15	0.155				
FeO_x-CNS-60	0.989	1.28	0.219				

Table S2.2. Summary of arsenic adsorption capacity data.

Samples	q_{max} (mg g^{-1}) for As(III)	q_{max} (mg g^{-1}) for As(V)
A-CNS	104	50
S-CNS	138	63
FeO_x-CNS-7	246	93
FeO_x-CNS-13	**416**	**201**
FeO_x-CNS-28	182	61
FeO_x-CNS-60	160	50

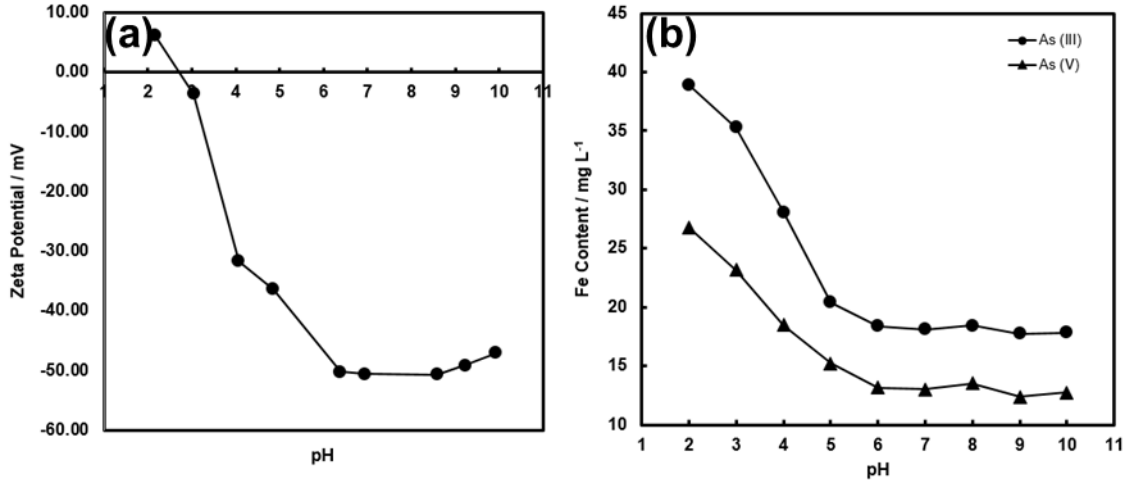

Figure S2.6. (a) Zeta potential of FeO_x-CNS-13 as a function of pH, and (b) the concentration of leached Fe in the equilibrium solution as a function of pH, where the initial arsenic concentration is 1,000 mg L^{-1}.

Chapter 3:

Amorphous Iron Oxide-Graphene Oxide Nanocomposites as High-Performance Adsorbents for Arsenic Removal

This chapter is adapted from a manuscript draft prepared (by H. Su, Z. Ye and N. Hmidi) for journal publication.

Abstract

We report the synthesis of a new range of amorphous iron oxide-graphene oxide (GO) nanocomposites having different iron oxide content (36–80 wt%) as high-performance adsorbents for arsenic removal. Synthesized by co-precipitation of iron oxide on GO sheets that are prepared by an improved Hummers method, the iron oxide in the nanocomposites is featured primarily in the desirable form of amorphous nanoparticles with an average size of ca. 5 nm. This unique amorphous nanoparticle morphology of the iron oxide beneficially endows the nanocomposites with high surface area (up to 341 m^2 g^{-1} for FeO_x-GO-80 having the highest iron oxide content of 80 wt%) and predominant mesopore structures, and consequently increased adsorption sites and enhanced arsenic adsorption capacity. In particular, FeO_x-GO-80 shows high arsenic adsorption capacity of 147 and 113 mg g^{-1} for As(III) and As(V), respectively, which are the highest among all the iron oxide-GO/reduced GO composite adsorbents reported to

date. It also nearly completely (>99.98%) removes arsenic by reducing the concentration from 118 (for As(III) or 108 (for As(V)) to < 0.02 μg L^{-1}, which is far below the limit of 10 μg L^{-1} required for drinking water. The excellent adsorption performance along with their cost-effective synthesis makes this range of adsorbents highly promising for commercial applications in drinking water and wastewater treatment.

Keywords: graphene oxide, arsenic adsorption, iron oxide, adsorption capacity.

3.1 Introduction

Arsenic is one of the most toxic and carcinogenic chemical elements. Arsenic contamination of natural water sources due to mineral leaching and/or anthropogenic activities has been considered as one of the most serious environmental problems worldwide.[1-3] Inorganic arsenic species, primarily in the forms of arsenate (As(V)) and arsenite (As(III)), are believed to be more toxic than the organic forms. Both As(V) and As(III) exist in natural water, with the latter being more toxic and more difficult to remove than the former.[1-3] To date, a variety of techniques has been developed to remove arsenic from both natural and industrial water sources such as coagulation, adsorption, ion exchange, membrane filtration, oxidization, biological remediation, etc.[3,4] In particular, adsorption is considered to be most economical and efficient over other techniques, especially in the low concentration range. A wide range of adsorbents have been studied to remove arsenic from water and wastewater, including commercial activated carbons,

metal oxides, agricultural and industrial by-products/wastes, soils and constituents, natural minerals, etc.[3,4]

Compared to other types of adsorbents, iron oxide-derived adsorbents have received enormous attention for arsenic removal due to their superior performance for arsenic adsorption.[5] In this regard, various forms of iron oxides have been studied and developed for arsenic removal, including amorphous iron oxide,[6,7] goethite (α-FeOOH),[8] hematite (α-Fe_2O_3),[8,9] crystalline magnetic maghemite (γ-Fe_2O_3) and magnetite (Fe_3O_4) nanoparticles,[10-12] as well as other iron oxide nanostructures.[13-20] The specific surface area, along with surface properties, has been one major parameter determining the arsenic adsorption capacity of these adsorbents.[4] In this regard, amorphous iron oxides show the highest adsorption capacity (as high as 260 and 200 mg g^{-1} for As(III) and As(V), respectively) among the various forms of iron oxides due to its highest specific surface area,[8] but with the shortcomings of its difficulty (as fine powders) for separation following adsorption and its tendency to form low-surface-area crystalline iron oxides during preparation.[4] In contrast, magnetic crystalline iron oxides generally show lowered adsorption capacity [< ca. 25 mg g^{-1} for both As(III) and As(V)] due to their low specific surface area.[10-12] Reducing the size of the crystalline iron oxide nanoparticles can substantially increase the surface area and consequently the arsenic adsorption capacity, e.g., up to ca. 175 and 200 mg g^{-1} for As(III) and As(V), respectively, reported for ultrasmall magnetite nanoparticles at a size of 12 nm.[11,12] The synthesis of such ultrasmall stable nanoparticles is often costly due to the requirement of surfactants to avoid their aggregation, which limits their widespread application. The various iron oxide

nanostructures,[13-20] though designed elegantly, generally show relatively low adsorption capacity with only few exceptions due to enhanced surface area[14,15,20], e.g., adsorption capacity of 162 mg g^{-1} for As(V) with γ-Fe_2O_3 nanochains.[20] Meanwhile, they have the same issue of cost-effectiveness due to the requirement of special, sophisticated synthesis and/or expensive additives/precursors.

Iron oxide-derived nanocomposite adsorbents prepared by loading iron oxides onto various substrates have also been extensively developed and investigated for arsenic adsorption.[3,4] Typical substrates include low-cost abundant ones, such as naturally occurring minerals,[21] activated carbons,[22] graphene oxide (GO),[23-33] and cellulose,[34] as well as some specially-synthesized costly ones, such as mesoporous carbons,[35,36] carbon nanotubes,[37] macroporous silica,[38] etc. Such nanocomposite adsorbents facilitate their more convenient separation following adsorption. However, their maximum arsenic adsorption capacity is often relatively low. In one case reporting high adsorption capacity [320 and 248 mg g^{-1} for As(III) and As(V), respectively], the substrate (macroporous silica) employed is too costly for practical applications.[38] Due to its unique two-dimensional one-atom-thick sheet structure with high surface area and abundant oxygen-containing functionalities, GO prepared easily from abundant graphite by oxidization and reduced GO (RGO) prepared by subsequent reduction of GO have recently received significant interest for environmental remediation applications.[39-42] Crystalline magnetic iron oxide nanoparticles have been loaded onto GO or RGO, rendering nanocomposite adsorbents for arsenic adsorption.[23-33] However, the arsenic adsorption capacity achieved thus far with the iron oxide-GO/RGO nanocomposite adsorbents is commonly very low

[only up to 54 and 73 mg g^{-1} reported for As(III) and As(V), respectively], with significant room for further improvements.

Tackling the above issues, we report in this paper the synthesis of a range of cost-effective amorphous iron oxide-GO nanocomposite adsorbents of significantly improved arsenic adsorption capacity. The key to the significantly enhanced adsorption capacity is the unique loading of amorphous iron oxide nanoparticles of high specific surface area on GO. The composite adsorbents have been designed to contain different contents of the amorphous iron oxide, and have been thoroughly characterized for their compositional, structural, and textural properties. A systematic study on the performance of these composite adsorbents for the adsorption of As(III) and As(V) has been undertaken. Our results suggest their high potential as cost-effective adsorbents for arsenic removal from both drinking water and industrial wastewater.

3.2 Experimental Section

3.2.1 Materials

Natural graphite flake (+100 mesh: ≥ 75.5%, Aldrich), potassium permanganate (99.0+%, Sigma Aldrich), hydrogen peroxide (50%, Fisher Scientific), sulfuric acid (96.9 wt%, Fisher Scientific), phosphoric acid (85+%, Acros), ferrous sulfate heptahydrate (99+%, Sigma Aldrich), ferric sulfate hydrate (97%, Fe 21.6%, Sigma Aldrich), ammonium hydroxide solution (28–30%, Sigma Aldrich), hydrochloric acid (37%, Fisher

Scientific), methanol (ACS reagent, Fisher Scientific), were used as received without any additional purification. Deionized water was purified by a Barnstead/Synbron Nanopure II purification system.

Sodium (meta) arsenite ($NaAsO_2$, ≥90%, Aldrich) and sodium arsenate dibasic heptahydrate ($Na_2HAsO_4 \cdot 7H_2O$, ≥98%, Aldrich) were selected as the source of As(III) and As(V), respectively. As(III) and As(V) stock solutions at the arsenic concentration of 2,000 mg L^{-1} were prepared in deionized water. The standard arsenic solutions with different concentrations were diluted from the 2,000 mg L^{-1} stock solutions with the pH adjusted to desired values with HNO_3 or NaOH.

3.2.2 Synthesis of graphene oxide (GO)

GO was synthesized by exfoliation of natural graphite flakes with the use of an improved Hummers method reported by Tour et al.[43] In a typical process, a 9:1 mixture of concentrated H_2SO_4/H_3PO_4 (360:40 mL) was mixed in a round-bottom flask, then 3 g of graphite flakes were added to the mixture under vigorous mechanic stirring for 10 min to obtain a dark-colored suspension. Subsequently, 18 g of $KMnO_4$ was added slowly into the above suspension kept in an ice bath. The mixture was stirred vigorously for 36 h at 50 ºC. A reddish brown viscous mixture was obtained. This mixture was cooled to room temperature, and then poured slowly into 400 mL of cold deionized water containing 3 mL of H_2O_2 (50%). Afterwards, the suspension was centrifuged and washed sequentially with HCl, water, followed by methanol for several times, until pH reached 6. The solid material was collected after centrifugation and dispersed again in 1200 mL of water as the

stock solution (GO concentration of 3.5 mg mL^{-1}; 4.2 g in total). The GO powder was obtained by drying overnight under vacuum at room temperature.

3.2.3 Preparation of amorphous iron oxide-GO nanocomposites (FeO_x-GOs)

FeO_x-GO composites were synthesized by the co-precipitation method. The GO suspension (64 mL, containing 0.22 g of GO) was first dispersed in 160 mL of water. An aqueous solution of $Fe_2(SO_4)_3$ and $FeSO_4$ at 1:1 molar ratio (or Fe^{3+} : Fe^{2+} = 2:1) was prepared. In the case for the preparation of the nanocomposite with 80 wt% of iron oxide (FeO_x-GO-80), the amounts of ferric sulfate hydrate and ferrous sulfate heptahydrate were 1.51 g and 0.81 g, respectively. The solution of $Fe_2(SO_4)_3$ and $FeSO_4$ were added into the GO suspension slowly at room temperature. Subsequently, 30% ammonia solution was added under stirring to this suspension to obtain pH = 10. The suspension was heated to 85 ºC and rapidly stirred for 40 min. It was then cooled down to room temperature. The resulting black suspension was filtered, washed with water and methanol several times, and finally dried overnight under vacuum at 60 ºC, rendering 850 mg of FeO_x-GO-80. Two other nanocomposites (FeO_x-GO-36 and FeO_x-GO-60) containing different contents (36 and 60 wt%, respectively) of iron oxide were similarly prepared. The pure iron oxide control sample was synthesized by the same method, but in the absence of GO.

3.2.4 Characterizations and Measurements

Thermogravimetric analysis (TGA) of the FeO_x-GO nanocomposites was carried out on a Q50 TGA from TA instruments. Measurements were performed in an air atmosphere. In a typical measurement, the sample (10 mg) was heated to 100 ºC at a rate of 10 ºC min^{-1}, held at 100 ºC for 10 min, and then heated to 800 ºC at a rate of 10 ºC min^{-1}. Braunauer–Emmett–Teller (BET) specific surface area, pore volume, and pore size distribution of all FeO_x-GO nanocomposites were determined by N_2 sorption at 77 K using a Micromeritics ASAP 2020 physiosorption analyzer. Before the sorption measurements, the samples were degassed under vacuum at 100 ºC for at least 12 h. X-ray photoelectron spectroscopy (XPS) measurements of FeO_x-GOs nanocomposites were carried out on a Thermo Scientific Theta Probe XPS spectrometer. A monochromatic Al Kα X-ray source was used, with a spot area of 400 μm. The samples were run in a standard mode, i.e., all angles collected (60º angular acceptance) for the survey spectra, and for the region spectra. Wide-angle x-ray diffraction (XRD) patterns of the FeO_x-GO nanocomposites were recorded on an X'Pert Pro diffractometer with Cu radiation (wavelength 1.54 Å) at room temperature. Transmission electron microscopy (TEM) images were taken on a JEOL 2010F field emission electron microscope operated at 200 keV. The TEM samples were prepared by depositing a few drops of a dilute dispersion of the FeO_x-GO composites in methanol on holey grids, followed with drying. Atomic force microscopy (AFM) imaging of the GO sample was performed on a Bruker multimode atomic force microscope in the tapping mode with a phosphorous-doped silicon tip having a force constant of 20–80 N m^{-1}. AFM samples were prepared by placing a freshly cleaved mica piece in the dilute dispersion (ca. 0.1 mg mL^{-1}) of the GO sample overnight

for sample deposition, which was then taken out and dried for the imaging. Fourier-transformed infrared (FTIR) spectra were obtained on a Thermo Scientific Nicolet 6700 Analytical FTIR spectrometer. The samples were prepared as pellets using spectroscopic-grade KBr. Zeta potential measurements of the dilute dispersions (0.1 mg mL^{-1}) of the various the FeO_x-GO nanocomposites were performed with a Brookhaven NanoBrook Omni Instrument at 25 ºC. The concentration of arsenic was measured with an Analytik Jena 810 inductively coupled plasmon mass spectrometry (ICP-MS) system with a detection limit of 50 μg L^{-1} or with a Thermal Fisher iCAP Q ICP-MS system with a detection limit of 0.02 μg L^{-1} for the solutions with arsenic in the very low concentration range.

3.2.5 Arsenic Adsorption

All the arsenic adsorption experiments were undertaken at room temperature, i.e., 23 ºC. Batch equilibrium adsorption of arsenic was carried out at an adsorbent loading of 0.8 mg mL^{-1}. Typically, the FeO_x-GO nanocomposites (2.4 mg) were dispersed in the As(III) and As(V) solutions (3 mL) at different initial concentrations (0.1–1200 mg L^{-1}) and pH, followed by magnetic stirring (300 rpm) for 24 h to achieve adsorption equilibrium. Afterwards, the suspension was filtered using a 0.2 μm Teflon syringe filter and the equilibrium concentration of non-adsorbed arsenic in the filtrate solution was determined. The equilibrium adsorption uptake (q_e in mg g^{-1}) was calculated according to Equation 1 from the difference between the initial arsenic concentration (C_0, mg L^{-1}) and the equilibrium one (C_e, mg L^{-1}):

$$q_e = (C_0 - C_e)V/m \qquad (1)$$

where V is the solution volume (L), and m is the mass of the adsorbent (g).

The adsorption isotherms were fitted with the Langmuir model (Equation 2).

$$q_e = abC_e/(1 + bC_e) \qquad (2)$$

where a is the monolayer saturated/maximum adsorbed capacity (mg g^{-1}) and b is the Langmuir constant that directly relates to the adsorption affinity (L mg^{-1}).

The adsorption kinetic curves with FeO_x-GO-80 as the adsorbent were obtained as follows. FeO_x-GO-80 at the same amount (2.4 mg) was dispersed in a series of As(III) and As(V) standard solutions of the same volume (3 mL) and concentration [400 mg L^{-1} for As(III) and 350 mg L^{-1} for As(V)]. Each dispersion was stirred for a prescribed time (ranging from 15 min to 24 h) and was then quickly filtered for measurement of the corresponding equilibrium concentration of As(III) and As(V) in the filtrate, thus giving rise to the time-dependent adsorption capacity. The adsorption kinetics was fitted with the pseudo-second-order kinetic model (Equation 3 or 4) based on which the initial adsorption rate could be obtained (Equation 5).

$$dq_t/dt = k_2(q_e - q_t)^2 \qquad (3)$$

$$t/q_t = 1/(k_2q_e^2) + t/q_e \qquad (4)$$

$$V_0 = k_2q_e^2 \qquad (5)$$

where q_t is the amount (mg g^{-1}) of arsenic adsorbed on adsorbent at various time t, k_2 is the rate constant (g mg^{-1} min^{-1}), q_e is the equilibrium adsorption capacity (mg g^{-1}), and V_0 is the initial adsorption rate (mg g^{-1} min^{-1}).

The effects of coexisting anions (CO_3^{2-}, SO_4^{2-}, and PO_4^{3-}) on the batch adsorption of As(III) and As(V) were investigated with FeO_x-GO-80 at the initial arsenic concentration of 100 μg L^{-1} at the pH of 6.5. The molar concentration of the coexisting anions was set excessively at 1000 times of that of arsenic (i.e., 184, 189, and 282 mg L^{-1} for K_2CO_3, Na_2SO_4, and K_3PO_4 respectively), with the adsorbent loading of 5 mg in 6.25 mL (i.e., 0.8 mg mL^{-1}). Each adsorption underwent for 24 h under stirring. Afterwards, the suspension was filtered and the filtrate was analyzed with ICP-MS for equilibrium arsenic concentration and the subsequent calculation of the equilibrium adsorption capacity by Equation 1.

3.3 Results and Discussion

3.3.1 Synthesis and Characterization of FeO_x-GOs Nanocomposites

The Hummers method[44] or modified Hummers method has been commonly used for the preparation of GO in the previous studies on iron oxide-GO/RGO composite adsorbents for arsenic adsorption.[23-33] Unlike those previous studies, GO used herein was synthesized with an improved Hummers method developed by Tour et al.[43] Relative to the Hummers and modified Hummers methods, the improved method is noted for improved oxidation efficiency and the greater retention of the graphitic basal plane framework. Figure S3.1 in Supporting Information shows an AFM image of the GO sample synthesized and employed herein. It consists of typical 2-dimensional sheet-like structures, which are loosely bound. The sheets have the lateral dimension within the

range of ca. 1–10 μm and the thickness of around 1–2 nm (see Figure S3.1). The GO sample was characterized with XPS. Its C_{1s} XPS spectrum (see Figure S3.2) is deconvoluted into four peaks that correspond to the following functional groups: carbon sp^2 (C=C, 284.8 eV), epoxy/hydroxyls (C–O, 287.0 eV), carbonyl (C=O, 288.8 eV), and carboxylates (O–C=CO, 289.9 eV).[45] Integration of the deconvoluted peaks indicates that the GO sample has 64% oxidized carbon (and 36% graphitic carbon). This indicates a very high degree of functionalization, where the edges and basal plane of each sheet should be functionalized with oxygen-containing polar groups such as carboxyl, epoxy, hydroxyl, etc.

Due to the high degree of functionalization, the GO powder readily disperses in water to form a stable aqueous suspension upon ultrasonication and stirring. To prepare FeO_x-GO composites, iron salts, $Fe_2(SO_4)_3$ and $FeSO_4$ at 1:1 molar ratio, were added into the aqueous GO suspension as the iron oxide precursors. Iron compounds have been reported to form cross-linking with the oxygen functionalities on the surface of carbon materials.[45] Subsequently, ammonium hydroxide was added into the mixture, followed with subsequent reaction at 85 ºC and post-treatment (precipitation, washing, and drying at 60 ºC). With the equal molar feeding of the two iron salts, we expected to obtain iron oxide with Fe^{3+} and Fe^{2+} at a molar ratio of 2 in the composites. Scheme 1 shows the schematic synthesis. By controlling the feed ratio of the iron salts to GO, three FeO_x-GO composites having different iron oxide contents were prepared. Meanwhile, a pure iron oxide control sample was also synthesized in the absence of GO for the purpose of comparison.

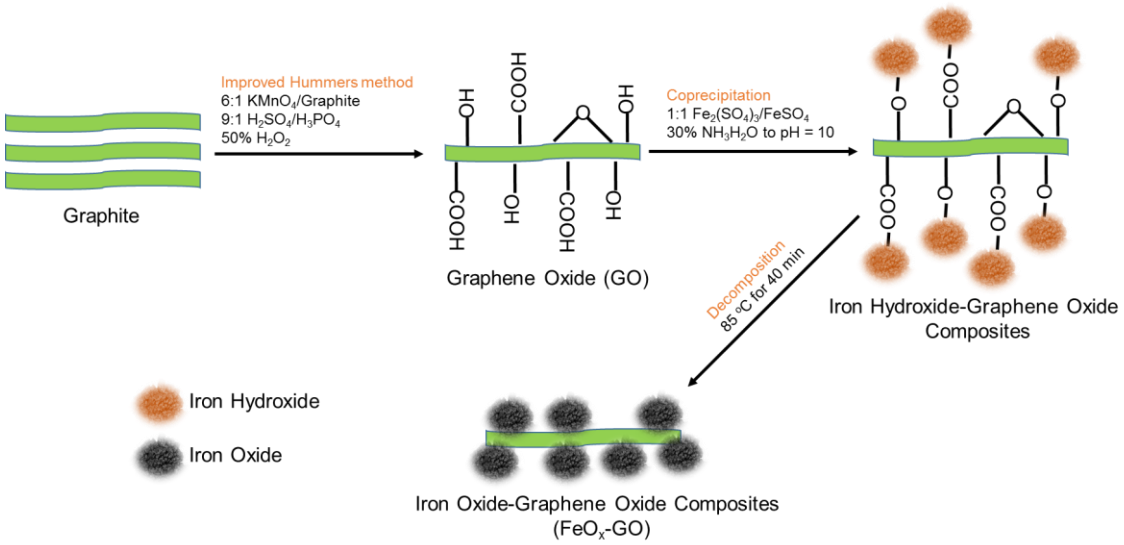

Scheme 3.1. Schematic synthesis of FeO_x-GO nanocomposites.

The resulting composites were thoroughly characterized. Figure 3.1 shows the TGA curves of the composites and their differential curves, along with those of GO and the iron oxide control sample. GO shows a characteristic two-step weight loss. The first step (loss of ca. 40%) occurs within 150–250 ºC with the peak weight loss at 203 ºC. It can be attributed to the evaporation of adsorbed water and the decomposition of thermally labile oxygen-containing functional groups. The second weight loss takes place within 400–500 ºC (peak at 467 ºC) with negligible char yield at 600 ºC. It is ascribed to the decomposition of more stable oxygen functionalities and the combustion of GO framework.[46] On the contrary, the iron oxide control sample shows negligible weight loss even at 600 ºC. The FeO_x-GO composites show weight loss within 100–420 ºC. Their char yield at 600 ºC, which represents the content of iron oxide in the nanocomposites, is 36, 60, and 80 wt%, respectively. In consequence, the composites are termed correspondingly as FeO_x-GO-36, FeO_x-GO-60, and FeO_x-GO-80, with the number representing the mass percentage of iron oxide in the composites. In particular, the iron

oxide content of FeO_x-GO-80 is significantly higher than the typical values (around 10–60 wt%) in iron oxide-GO composites synthesized in earlier works for arsenic adsorption.[23-33] On the basis of their differential curves, the major weight loss of the composites occurs within 250–500 ºC, along with a long tail/shoulder peak within 100–250 ºC. This indicates the significant overlap of the two weight-loss steps due to the decrease of combustion/degradation temperature. With the increase of the iron oxide content, the peak weight-loss temperature shows a continuous decrease from 360 ºC for FeO_x-GO-36 to 338 ºC for FeO_x-GO-60 and to 318 ºC for FeO_x-GO-80. This can be ascribed to the enhanced surface area and pore volume with the increase of iron oxide content in the composites as shown below, which lead to the enhanced contact of GO surface with air for combustion. Meanwhile, it can also result from the existence of iron oxide on the GO surface, which acts as catalysts for the carbon combustion since their exothermic oxidation takes place at lower temperatures.[36]

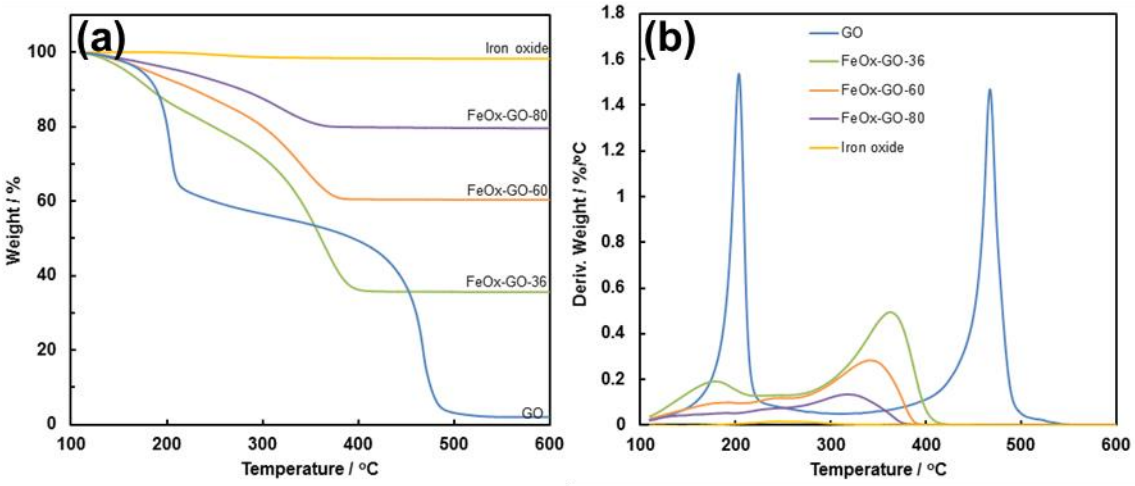

Figure 3.1. TGA curves (a) and differential curves (b) for GO, FeO_x-GO-36, FeO_x-GO-60, FeO_x-GO-80 and iron oxide control sample in the air atmosphere.

Figure 3.2 shows the TEM images and high-resolution TEM images of two composites, FeO_x-GO-36 and FeO_x-GO-80, as well as those of GO and the iron oxide control sample. GO appears as wrinkled sheets under TEM (Figure 3.2(a)). The iron oxide control sample consists of nanoparticles with sizes in the range of 10–20 nm (Figure 3.2(g)). The atomic lattice fringes in the high-resolution TEM images (Figure 3.2(h)) confirm the single crystalline nature of the nanoparticles with an interplanar spacing of about 0.25 nm, which matches well with the (311) lattice spacing of crystalline Fe_3O_4.[47] In the two composites, GO sheets are decorated irregularly with iron oxide nanoparticles (see Figure 3.2(c) and (e)). From the high-resolution images (Figure 3.2(d) and (f)), the iron oxide nanoparticles have an average size of about 5 nm and are primarily amorphous with no distinct crystalline lattice fringes observed. This is in sharp contrast to the crystalline Fe_3O_4 nanoparticles observed in the iron oxide control sample, which was prepared under the same conditions except in the absence of GO. Clearly, the

presence of GO in the coprecipitation preparation of iron oxide promotes the formation of amorphous iron oxide nanoparticles in the composites.

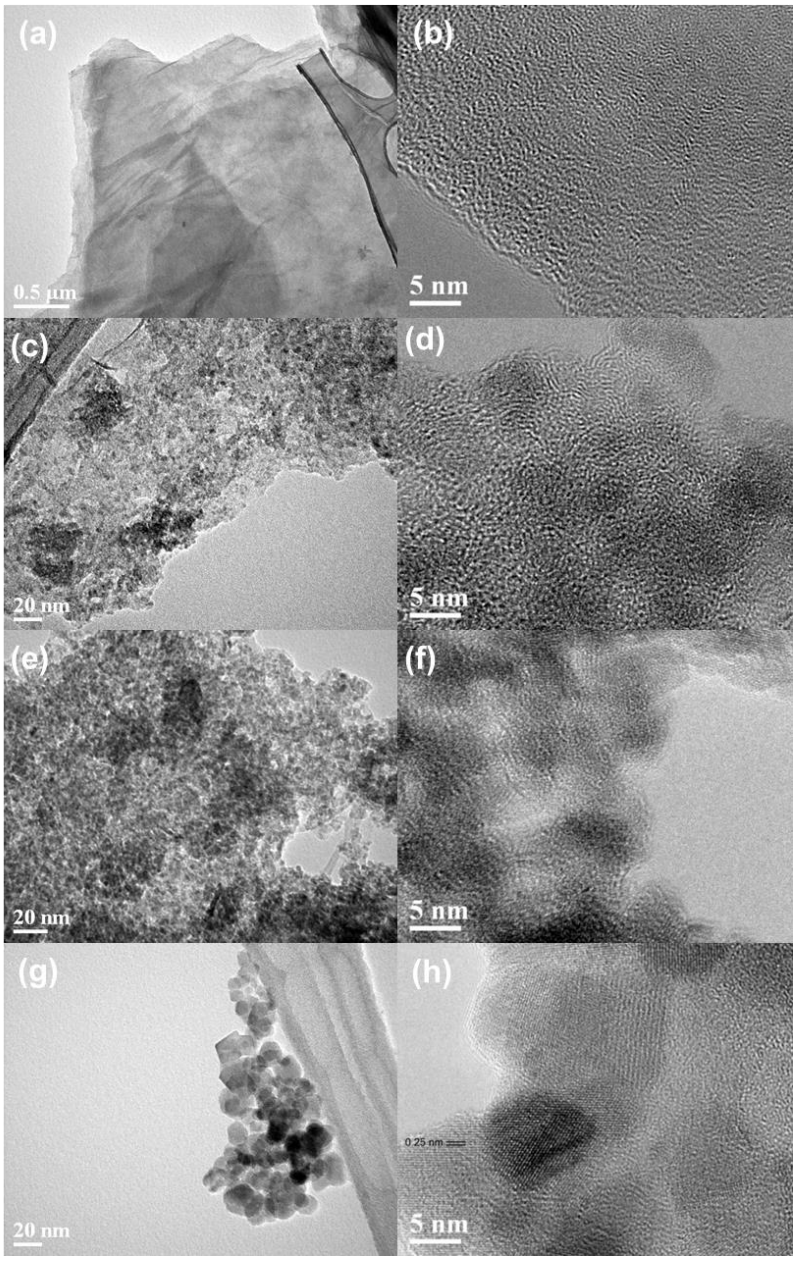

Figure 3.2. TEM and high-resolution TEM images of GO (a and b), FeO_x-GO-36 (c and d), FeO_x-GO-80 (e and f), and the iron oxide control sample (g and h).

To further elucidate the distribution of iron oxide species in the composites, the two composites (FeO_x-GO-36 and FeO_x-GO-80) were characterized with the dark-field scanning TEM (DF-STEM) technique. As shown in Figure S3.3(a), bright spots can be found in the dark domain of FeO_x-GO-80 containing C and O, indicating the existence of heavy atoms, namely Fe. Figure S3.3(b)–(d) show the elemental mapping of C, O, and Fe within the domain. All the three elements are uniformly distributed, confirming the uniform dispersion of iron oxide within the composite. Similarly, the uniform distribution of iron oxide is also confirmed in FeO_x-GO-36 having a lower iron oxide content (see Figure S3.4).

FTIR spectra of GO, the FeO_x-GO composites, and the iron oxide control sample are shown in Figure 3.3. The spectrum of GO shows C=O (1729 cm^{-1}), aromatic C=C (1620 cm^{-1}), carboxyl O=C–O (1400 cm^{-1}), epoxy C–O (1225 cm^{-1}), and alkoxy C–O (1053 cm^{-1}) stretching vibrations.[48] The spectrum of iron oxide sample shows two broad bands in the low frequency region (750−400 cm^{-1}), corresponding to the Fe–O vibration in Fe_3O_4.[36] The infrared spectra of FeO_x-GO-36, FeO_x-GO-60, and FeO_x-GO-80 all show a broad band with the peak maximum at 1578 cm^{-1}, corresponding to aromatic C=C stretch in GO.[23] Other bands arising from GO become indistinct in the composites due to its lowered content. In FeO_x-GO-80, the presence of iron oxide can be confirmed from the bands at 552 cm^{-1} and 442 cm^{-1}. FeO_x-GO-36 and FeO_x-GO-60 show also similar spectral characteristics with more or less differences in the absorption intensities in the low wavenumber range due to their relatively lowered iron oxide content.

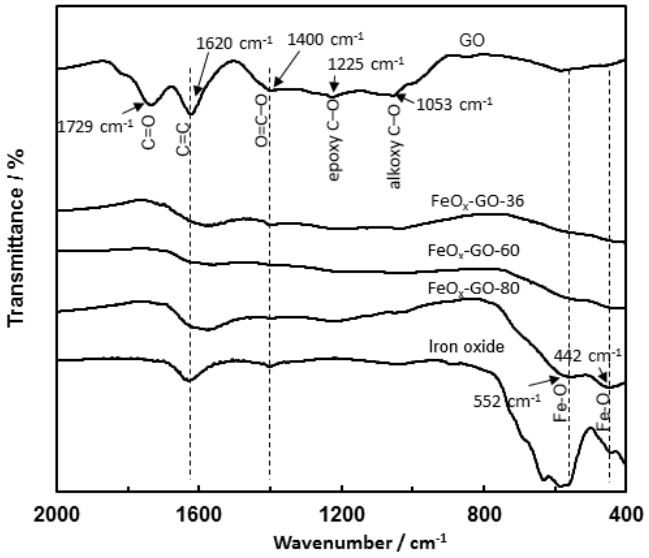

Figure 3.3. FTIR spectra of GO, FeO_x-GO composites, and the iron oxide control sample.

Two composites, FeO_x-GO-36 and FeO_x-GO-80, as well as GO and the iron oxide control sample, were also characterized with XPS (see Figure 3.4). From the survey scan (Figure 3.4(a)), the surface of GO contains 40.4 atom% of C and 55.0 atom% of O (see Figure 3.4(b)). After loading the amorphous iron oxide at the increasing content, the counts of O_{1s} and C_{1s} in the composites decrease (34.5 atom% of C and 36 atom% of O for FeO_x-GO-36, 13.1 atom% of C and 27.7 atom% of O for FeO_x-GO-80) whereas the counts of Fe increase dramatically (25.2 and 57.7 atom% for FeO_x-GO-36 and FeO_x-GO-80, respectively). Two photoelectron peaks located at 711.1 ($Fe_{2p3/2}$) and 724.6 eV ($Fe_{2p1/2}$) are found in the Fe_{2p} spectra of the composites and the iron oxide control sample (Figure 3.4(c)–(e)).[23] Each peak is deconvoluted to the constituting peaks attributable to Fe^{3+} and Fe^{2+}, respectively, as well as their satellite peaks.[49,50] The Fe^{3+}/Fe^{2+} molar ratio in the iron oxide control sample is estimated to 2.03 according to the deconvoluted $Fe_{2p3/2}$ peaks, which is nearly identical to the theoretical value of 2 for Fe_3O_4. This also confirms

that the pure iron oxide control sample is in the form of Fe_3O_4 nanoparticles. The Fe^{3+}/Fe^{2+} molar ratio in FeO_x-GO-36 and FeO_x-GO-80 is estimated to be 2.92 and 1.87, respectively. While the latter for FeO_x-GO-80 is close to the expected theoretical value for Fe_3O_4, the former for FeO_x-GO-36 at a lower iron oxide loading deviates significantly from the theoretical value. This may result from the stronger complexation of Fe^{3+} than Fe^{2+} ions with oxygen functionalities on GO during the preparation and thus the higher incorporation within the composite.[24]

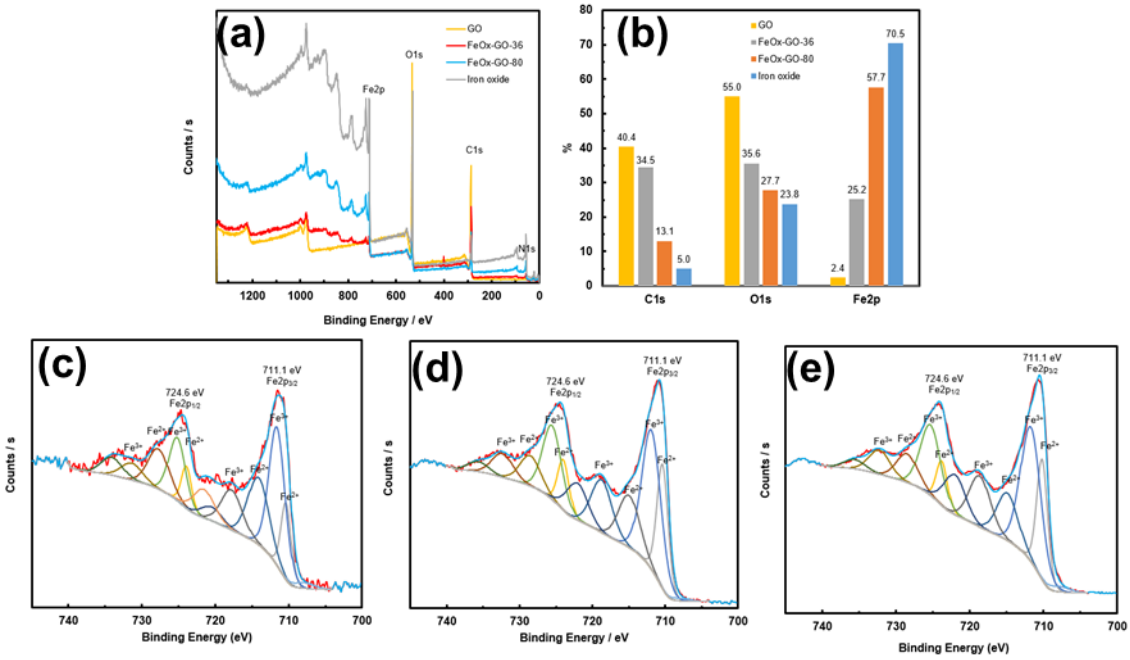

Figure 3.4. (a) XPS survey scan of GO, FeO_x-GO-36, FeO_x-GO-80, and the iron oxide control sample, (b) the content of C, O, and Fe in the samples measured by XPS, (c)–(e) Fe_{2p} spectra in FeO_x-GO-36, FeO_x-GO-80, and the iron oxide control sample, respectively.

The O_{1s} spectra of the samples are shown in Figure S3.2(b). In the spectra of the two nanocomposites, three deconvoluted peaks at 530.3, 531.6, and 533.6 eV are attributed to the oxygen atoms bonded to O–Fe, carboxyl O=C, and hydroxyl O–H, respectively.[23] In the spectrum of pure iron oxide, the former one is predominant with the negligible presence of the latter two. On the contrary, the former one is absent in GO. In the C_{1s} spectra (Figure S3.2(a)), three deconvoluted peaks at 284.8, 286.9, and 288.8 eV, can be found in the composites, assignable to the C atoms in C–C, C–O, and C=O groups in GO. By comparing the deconvoluted peaks, it appears that, after loading iron oxide onto GO, the relative intensity of the peak for C–O bonds has been significantly reduced while with the increasing intensity of that for C–C bonds, suggesting the partial reduction of GO in the composites possibly by Fe^{2+}. This may also contribute to the above noted deviation of Fe^{3+}/Fe^{2+} ratio from the expected theoretical value of 2 in the composites.

Figure 3.5 shows and compares the XRD spectra of GO, FeO_x-GO-80, and the iron oxide control sample. In the spectrum of GO, there is a strong peak at 12º arising from the interlayer spacing between stacked GO sheets.[43] This peak is absent in FeO_x-GO-80 due to the complete exfoliation of GO sheets by iron oxide. In addition, a very weak and broad peak is also noticed near 43º (indicated by arrows) in the spectrum of GO, which is attributed to the (100) peak of graphitic structures.[51] The iron oxide control sample shows sharp strong diffraction peaks matching well those of Fe_3O_4 (JCPDS Card #75-0033). Along with the above TEM and XPS evidence, we can thus confirm that the iron oxide control sample is indeed in the form of crystalline Fe_3O_4 nanoparticles. The average crystallite size (L) is evaluated from the full width at half maximum of the (311) peak at $2\theta = 35.5$º according to the Scherrer equation:

$$L = \frac{K\lambda}{\beta cos\theta} \qquad (7)$$

where K is the shape factor usually assigned as 0.9, λ is the wavelength used (1.54 Å), and β is the full width at half-maximum (in rad) of the diffraction peak. The resulting L is 16.4 nm, in good agreement with the Fe_3O_4 nanoparticle size range (10–20 nm) found above from the TEM image (Figure 3.2(g)). Despite its high content of iron oxide, FeO_x-GO-80 instead shows only some very weak diffraction peaks, which match the diffraction pattern of α-Fe_2O_3 (JCPDS Card #88-2377). In agreement with its TEM images, this indicates that the iron oxide in the composites is primarily in the amorphous form without a significant presence of crystalline nanoparticles. Due to the primarily amorphous nature of the iron oxide, the three FeO_x-GO composites synthesized herein were found only weakly magnetic.

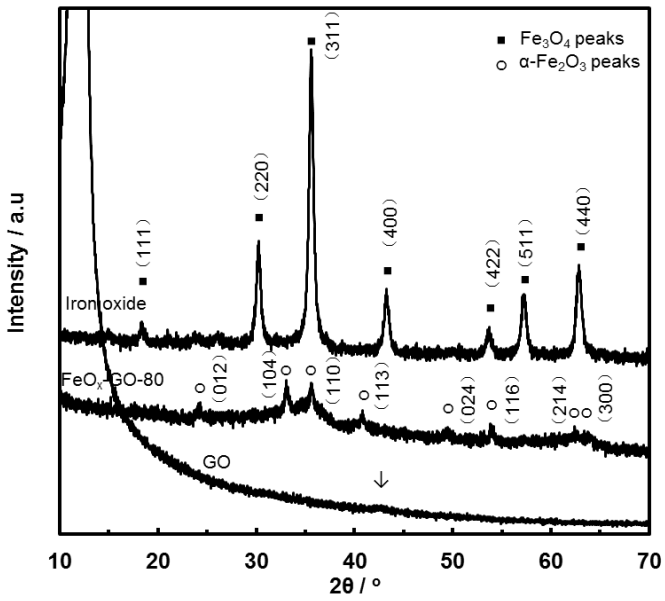

Figure 3.5. Wide-angle XRD patterns of GO, FeO_x-GO-80, and the iron oxide control sample.

The FeO_x-GO nanocomposites, along with GO and the iron oxide control sample, were further characterized with N_2 sorption analysis at 77 K for their textural properties. Table 3.1 summarizes the characterization data, including surface area, pore volume, and average meso-/macro-pore size. Figure 3.6(a) shows their N_2 adsorption-desorption curves. Both FeO_x-GO-80 and the iron oxide control sample show type IV adsorption isotherms, with the clear presence of a hysteresis loop. The other samples generally show type I isotherms with only very small hysteresis loops observed, indicating they are primarily microporous. The iron oxide control sample shows a slight uptake at the low relative pressure end ($P/P_0 < 0.05$), and a sharp uptake with a H1 type hysteresis loop at high relative pressure end ($P/P_0 > 0.9$),[52] indicating that the sample contains predominantly large mesopores and/or macropores (average size: 28 nm) as a result of the aggregation/packing of the crystalline Fe_3O_4 nanoparticles. GO and the iron oxide control sample have a surface area of 129 and 71 $m^2\ g^{-1}$, respectively, and a pore volume of 0.09 and 0.36 $cm^3\ g^{-1}$, respectively. On the basis of its surface area and magnetite density (5.18 $g\ cm^{-1}$),[10] the crystalline Fe_3O_4 nanoparticles in the iron oxide control sample have an estimated average diameter of 16 nm, which is nearly identical to the average size estimated above from XRD.

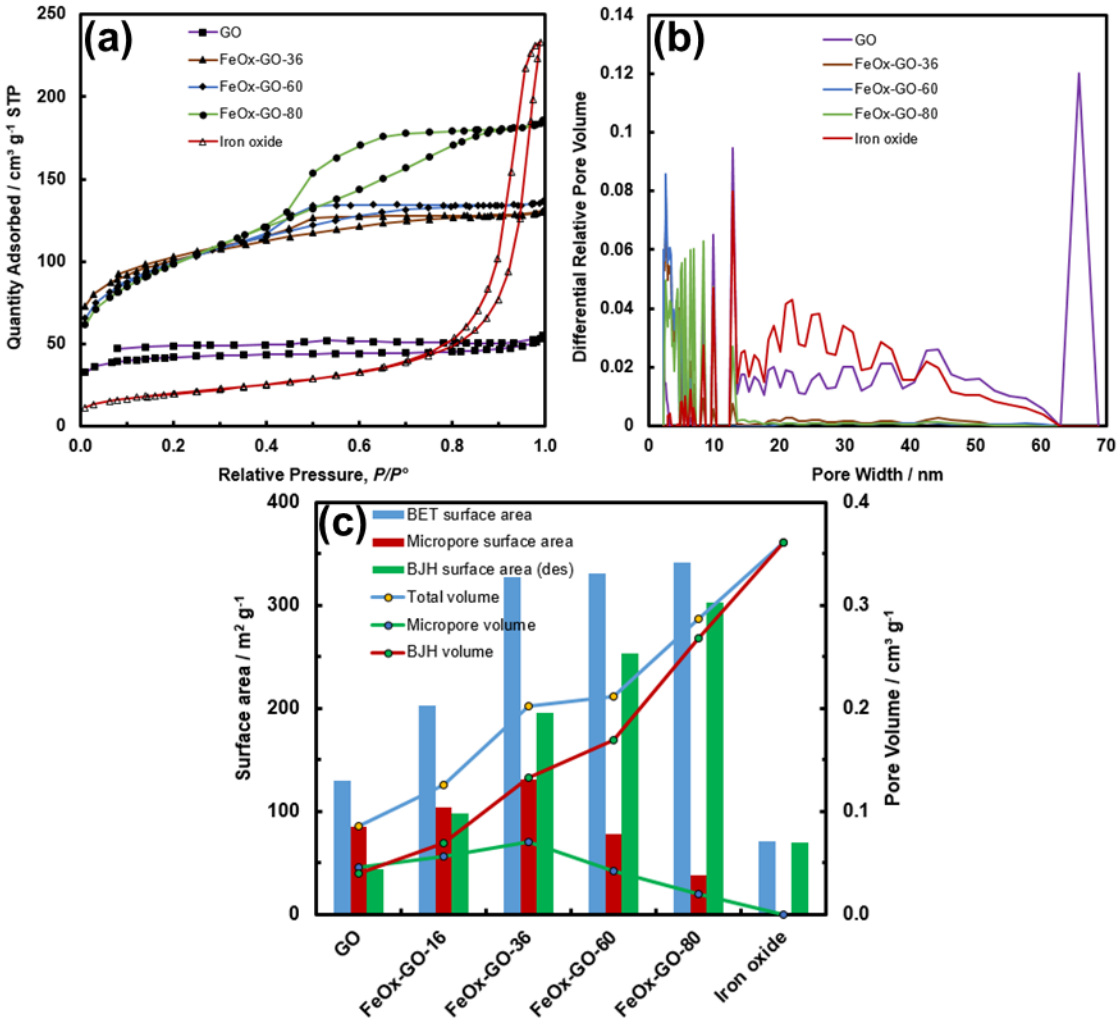

Figure 3.6. (a) N_2 adsorption-desorption isotherm of FeO_x-GO composites, GO, and the iron oxide control sample, (b) DFT meso-/macro-pore size distribution curves, (c) dependencies of surface area and pore volume data on the iron oxide content.

Table 3.1. Results from N_2 sorption characterization.

Samples	Surface Area ($m^2\ g^{-1}$)[a]					Pore Volume ($cm^3\ g^{-1}$)[b]					Average Meso-/Macro-pore Size (nm)[c]
	S_{BET}	$S_{d<20Å}$	$\%S_{d<20Å}$	$S_{d>20Å}$	$\%S_{d>20Å}$	V_{total}	$V_{d<20Å}$	$\%V_{d<20Å}$	$V_{d>20Å(des)}$	$\%V_{d>20Å}$	$D_{meso/macro}$
GO	129	85	66%	44	34%	0.09	0.05	53%	0.04	47%	27
FeO_x-GO-36	327	131	40%	196	60%	0.20	0.07	35%	0.13	65%	6
FeO_x-GO-60	331	78	24%	253	76%	0.21	0.04	20%	0.17	80%	6
FeO_x-GO-80	341	38	11%	303	89%	0.29	0.02	7%	0.27	93%	7
Iron Oxide	71	1.4	2%	69.6	98%	0.36	0.00	0%	0.36	100%	28

a) BET surface area (S_{BET}), surface area of micropores (S_d<20 Å) and surface area of meso-/macro-pores (S_d>20 Å) determined with t-plot method. The percentage data denote the percentage of surface area of micropores or meso- and macro-pores relative to the total surface area. b) Total pore volume (V_{total}), micropore volume (V_d<20 Å) determined with t-plot method. The percentage data denote the percentage of pore volume of micropores relative to the total pore volume. c) Average meso-/macro-pore size ($D_{meso/macro}$) determined from the N_2 desorption data with NLDFT model.

Relative to GO and the crystalline Fe_3O_4 control sample, the three composites show significantly enhanced surface area (from 327 to 341 $m^2 g^{-1}$) and pore volume (from 0.20 to 0.29 $cm^3 g^{-1}$). Meanwhile, both surface area and pore volume show slight increases with the increase of the iron oxide content from FeO_x-GO-36 to FeO_x-GO-80. From the data in Table 3.1 and the pore size distribution in Figure 3.6(b), the enhanced surface area and pore volume arise mainly from the generation of more mesopores with sizes ≤ 12 nm. Both the micropore surface area and micropore volume of the composites show a trend of decrease with the increase of iron oxide content (see Figure 3.6(c) and Table 3.1). Relative to the value of about 27 nm for both GO and the iron oxide control sample, the average meso-/macro-pore size of the composites is about 7 nm, which is in the same range as the average size (ca. 5 nm) of the amorphous iron oxide nanoparticles seen above from the TEM images. This indicates that the generated mesopores are primarily inter-particle pores resulting from the packing/aggregation of the amorphous iron oxide nanoparticles. The surface area data of the three composites are also significantly higher than those of other iron oxide-GO/RGO nanocomposites[23,30] and various iron oxide nanostructures[13-21] reported in the literature. Clearly, the loading of the amorphous iron oxide nanoparticles on GO renders enhanced surface area and pore volume through the creation of more mesopore structures, which is beneficial to arsenic adsorption due to the increased active sites for the adsorption as shown below.

Unlike the composites herein, the iron oxides present in other iron oxide-GO/RGO composites reported in the literature for arsenic adsorption are often in the form of crystalline nanoparticles, despite very similar synthesis procedures and conditions as we used herein.[23-33] Though precise mechanism is not known, we reason that this results from

the different GO/RGO substrates employed, which affects the morphology of the loaded iron oxides. The exclusive formation of crystalline Fe_3O_4 nanoparticles in the control sample prepared in the absence of GO herein supports this hypothesis. The GO substrate synthesized herein via the improved method should be more oxidized than those commonly synthesized via the Hummers or modified Hummers method for the preparation of composites in the literature. The higher level of oxidation likely improves the complexation of iron species with GO, inhibits the formation of crystallization nuclei, and thus promotes the formation of amorphous iron oxide nanoparticles. Detailed precise mechanism is to be explored in future investigations.

3.3.2 Arsenic Adsorption with FeO_x-GO Nanocomposites

The performance of the FeO_x-GO nanocomposites for batch adsorption of both As(III) and As(V) has been systematically investigated, along with GO and the iron oxide control sample for comparison. The effect of the dosage (0.1–1 mg mL^{-1}) of FeO_x-GO-80 on the adsorption of As(III) (at pH = 7) and As(V) (at pH = 3) was first studied at the initial concentration of 1200 and 350 mg L^{-1}, respectively. The pH values were so chosen as to achieve optimum adsorption as shown below in the study on the effects of pH. Figure S3.5 shows the dependencies of the equilibrium adsorption amount (q_e) on the adsorbent dosage. In general, q_e changes only marginally across the whole adsorbent dosage range, with highest values obtained at the dosage of 0.8 mg mL^{-1} for both As(III) and As(V). The adsorbent dosage of 0.8 mg mL^{-1} was thus chosen for all subsequent investigations.

Figure 3.7 shows the arsenic adsorption isotherms of the various composite adsorbents as well as with GO and the iron oxide control sample in a broad equilibrium concentration range. The initial arsenic concentrations are 25–1200 mg L^{-1} for As(III) at pH = 7 and 25–350 mg L^{-1} for As(V) at pH = 3. All the isotherms have been found to follow the Langmuir adsorption model (Equation 2) with the high correlation coefficients ($R^2 \approx 1$, see Table S3.1 for fitting results) found. This suggests that the adsorption of both As(III) and As(V) with the adsorbents herein can be regarded as monolayer adsorption processes.

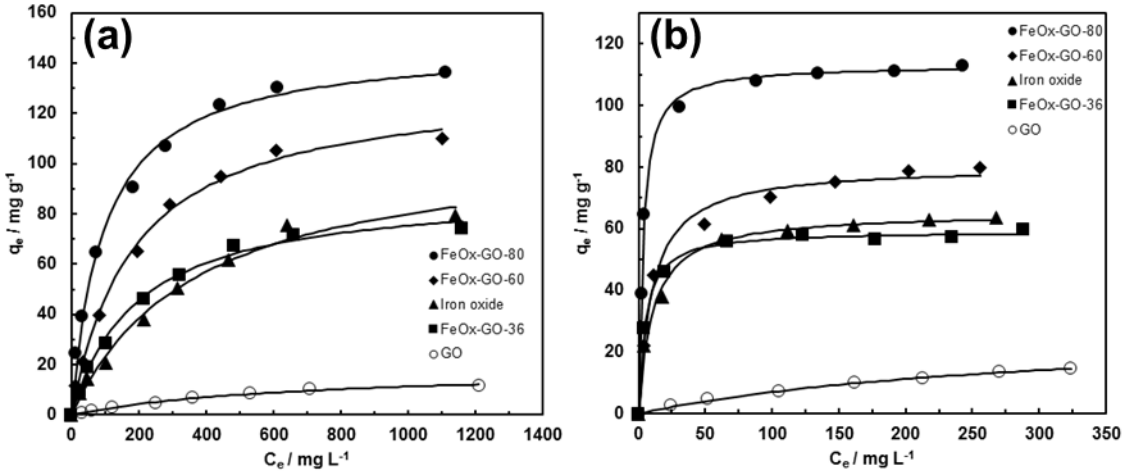

Figure 3.7. (a) As(III) adsorption isotherms (at pH = 7) and (b) As(V) adsorption isotherms (at pH = 3) of FeO_x-GO nanocomposites, GO, and the iron oxide control sample. All the isotherms are well fitted with the Langmuir model (solid line).

Among the adsorbents, GO shows the poorest adsorption performance with the lowest isotherms. Its maximum/saturated adsorption capacity (q_{max}) is only 19 and 28 mg g^{-1} for As(III) and As(V), respectively. The iron oxide control sample (q_{max} values of 110

and 65 mg g^{-1}) has its isotherms nearly overlapping with those of FeO_x-GO-36 (q_{max} values of 90 and 59 mg g^{-1}), indicating their similar adsorption performance. Despite its lower surface area, the much higher q_{max} values found with the iron oxide control sample than GO confirms the significantly higher affinity of the iron oxide surface for the arsenic species. With the increase of iron oxide content from FeO_x-GO-36 to FeO_x-GO-80, the isotherms for both As(III) and As(V) are continuously shifted upward, indicating the improved adsorption. FeO_x-GO-80 is featured with highest q_{max} values of 147 and 113 mg g^{-1} for As(III) and As(V), respectively, among all the adsorbents. While the surface area of three composites are only slightly different, the significant increase in q_{max} from FeO_x-GO-36 to FeO_x-GO-80 indicates the generation of significantly more iron oxide active sites of higher adsorption affinity per unit area with the increase of iron oxide content. Meanwhile, the increase in the more accessible mesopore surface area, along with the reduction in micropore surface area, upon the increase of iron oxide content as shown above also endows the improved accessibility of the active sites.

The q_{max} values found with FeO_x-GO-80 herein are the highest among all the iron oxide-GO/RGO composite adsorbents reported to date. Table 3.2 compares the arsenic adsorption capacity achieved with various iron oxide-GO/RGO composite adsorbents. Meanwhile, all the FeO_x-GO nanocomposites and the iron oxide control sample show higher q_{max} for As(III) than for As(V), while opposite for GO. This suggests the different interactions of the arsenic species with the adsorbents. It is desirable because of the prevalence of As(III) in groundwater and wastewater, which has higher toxicity than As(V).

Table 3.2. Comparison of maximum arsenic adsorption capacities achieved with iron oxide-GO/RGO nanocomposites.

Adsorbent	Iron oxide content	S_{BET} (m^2/g)	q_{max} (mg g^{-1})		Reference
			As(III)	As(V)	
Amorphous iron oxide-GO nanocomposites	**80 wt% of amorphous iron oxide**	**341**	**147**	**113**	**this study**
Fe_3O_4-RGO composites	75 wt% of Fe_3O_4	117	13.10	5.83	23
$Fe(OH)_3$-GO composites	54 wt% of $Fe(OH)_3$			23.78	24
Fe_3O_4-GO-LDH composites	21.1 wt% of Fe_3O_4	123.3		73.14	25
Fe_3O_4-GO composites	80% of Fe_3O_4			59.6	26
Fe-Fe_2O_3-graphene nanoplatelet composites			11.34		27
Fe-GO nanocomposites		165		3.26	30
Fe_3O_4-RGO nanocomposites			7.5	16	31
α-Fe_2O_3-Fe_3O_4-GO composite	51.7 wt% of iron oxide		26.76	54.18	32
Fe_3O_4-RGO composite				3.36	33

Not only featured with high adsorption capacity in the high arsenic concentration range, FeO_x-GO-80 also exhibits superior arsenic removal efficiency at the low arsenic concentration range. At the initial arsenic concentration of 118 (for As(III)) or 108 $\mu g\ L^{-1}$ (for As(V)) (at pH = 6.5, which is typical in natural waters), the equilibrium arsenic concentration after adsorption with FeO_x-GO-80 at the dosage of 0.8 mg mL^{-1} can be reduced to lower than 0.02 $\mu g\ L^{-1}$ for both As(III) and As(V), which is much lower than the maximum arsenic level of 10 $\mu g\ L^{-1}$ suggested by World Health Organization (WHO) for drinking water.[53] This corresponds to >99.98% of arsenic removal. No other iron oxide-GO nanocomposite adsorbents have been previously demonstrated to remove arsenic to such a low concentration. It also well competes with the high-performance γ-Fe_2O_3-macroporous silica composite adsorbent reported by Yu et al.,[38] which was shown to reduce the arsenic concentration to < 2 $\mu g\ L^{-1}$ with the same initial arsenic concentration of 100 $\mu g\ L^{-1}$.

Figure 3.8(a) shows the adsorption kinetics curves with FeO_x-GO-80 as the adsorbent at initial arsenic concentration of 400 and 350 mg L^{-1} for As(III) and As(V), respectively. For both As(III) and As(V), the adsorption can be divided into two stages, a rapid uptake within the first 15 min of contact and a slow uptake thereafter until equilibrium is reached. In particular, the majority of the arsenic uptake, 70 and 77% for As(III) and As(V), respectively, occurs within the first 15 min, indicating the very fast adsorption rate. The pseudo-second-order kinetic model (Equations 3 and 4), widely used to fit the kinetic process of metal ion adsorption at the solid/water interfaces, is employed to fit the curves. Excellent fitting of the experimental data is achieved with the model,

with the correlation coefficients of 0.9998 and 0.9992, respectively (see Figure 3.8(b) and Table S3.1), indicating the adsorption process occurs through the chemical interaction.[54] Meanwhile, the adsorption rates for both As(III) and As(V) are similarly high, with the same rate constant k_2 of 0.001 g mg^{-1} min^{-1} achieved. The k_2 value is very high, in particular for As(III), when compared to other superior adsorbents reported in the literature. For example, the high-performance γ-Fe_2O_3-macroporous silica composite adsorbent reported by Yu et al. has the k_2 values of 0.00015 and 0.0014 g mg^{-1} min^{-1} for As(III) and As(V), respectively, under similar conditions.[38] Therein, the adsorption rate for As(III) is 10 times slower than for As(V). The significantly high adsorption rate found with FeO_x-GO-80 for more toxic As(III) is thus remarkable, confirming its superior kinetics performance.

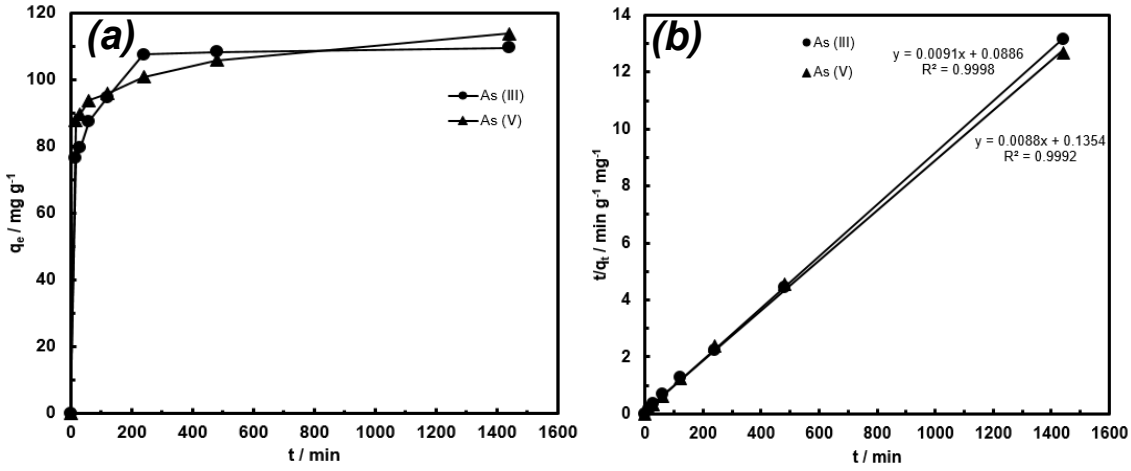

Figure 3.8. (a) As(III) and As(V) adsorption kinetic curves with FeO_x-GO-80 (initial arsenic concentration of 400 and 350 mg L^{-1} for As(III) (pH = 7) and As(V) (pH = 3), respectively; (b) fitting of the kinetic curves with the pseudo-second-order model.

The effects of the pH of the medium on arsenic adsorption have also been investigated since it changes the surface charge of FeO_x-GO composites and arsenic species distribution.[1-4] Figure 3.9(a) shows q_e as a function of pH (within 2–10) with FeO_x-GO-80 at the initial As(III) and As(V) concentration of 350 mg L^{-1}. With the increase of pH from 2 to 10, q_e for As(V) keeps dropping from 118 mg g^{-1} at pH = 2 to 55 mg g^{-1} at pH = 10. On the contrary, q_e for As(III) stays nearly at a plateau (105 mg g^{-1}) within the pH range of 7–10 and shows a steady drop to 70 mg g^{-1} with the decrease of pH from 7 to 2. Similar trends of the effects of pH have commonly been observed with iron oxide-based adsorbents and can be explained by the changes in surface charge of the adsorbents and the arsenic speciation.[7-9,12,21-24,26,32,34,37,38] Figure 3.9(b) shows the dependence of surface charge of FeO_x-GO-80 on pH. Increasing pH leads to a continuous decrease of its surface charge, with the point of zero charge (pH_{PZC}) being about 5.9. Its surface is positively charged at pH < pH_{PZC}. Under most pH conditions, As(V) is present in negative ionic form ($H_2AsO_4^-$ at pH 2.2–6.5, $HAsO_4^{2-}$ at pH 6.5–11.5), whereas As(III) is in a neutral form (H_3AsO_3 at pH below 9.2).[2] The electrostatic interactions between positively charged FeO_x-GO-80 and negatively charged As(V) species result in the strong adsorption of FeO_x-GO-80 when pH < pH_{PZC}. The surface of FeO_x-GO-80 is negatively charged at pH > pH_{PZC}, repulsing the negatively charged As(V) species. As such, increasing the pH leads to continuous reductions in q_e for As(V).

However, the adsorption mechanism of As(III) on FeO_x-GO-80 is different given the opposite trend of change. We first suspected that the lower As(III) uptake at the acidic conditions (2–6) might result from the dissolution and leaching of the iron oxide species from FeO_x-GO-80 into the solution.[23] This was, however, ruled out. No Fe species was

detected within the detection limit (< 0.5 ppm) of atomic absorption spectroscopy in the equilibrium solutions even at the highly acidic condition with pH = 2, demonstrating the strong binding of the iron oxide species on GO. The results indicate that As(III) is adsorbed onto FeO_x-GO-80 through a surface complexation mechanism, rather than electrostatic interactions.[23] The adsorption capacity increase with increasing pH may be attributed to the enhanced surface hydroxyl groups at higher pH values for complexation.[37]

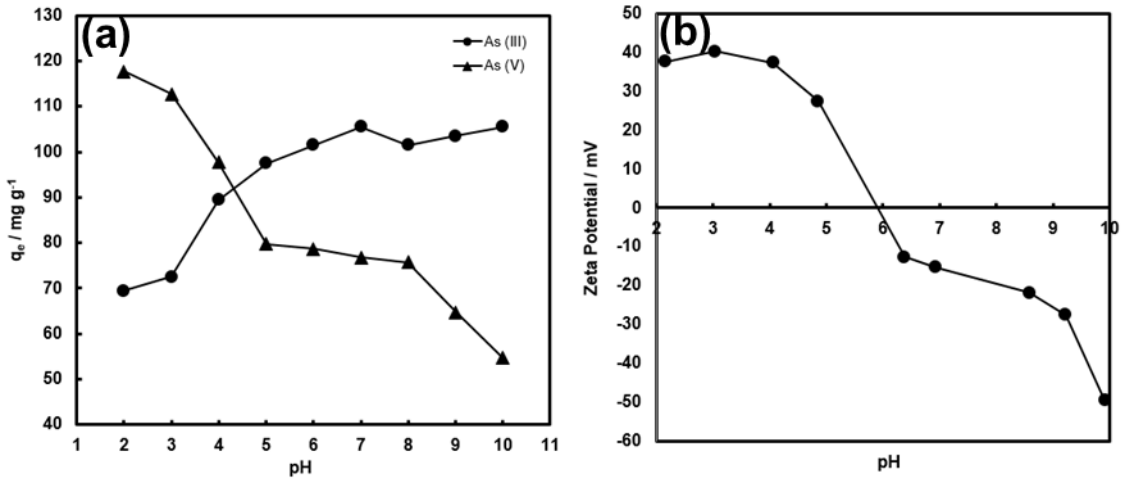

Figure 3.9. (a) Arsenic uptake of FeO_x-GO-80 as a function of pH (initial arsenic concentration of 350 mg L^{-1}); (b) Zeta potential of FeO_x-GO-80 as a function of pH.

We have also examined the effects of coexisting anions (SO_4^{2-}, CO_3^{2-}, and PO_4^{3-}) on the arsenic adsorption with FeO_x-GO-80 (dosage: 0.8 mg mL^{-1}) at the low initial arsenic concentration of 118 (for As(III)) or 108 μg L^{-1} (for As(V)) and at the initial pH of 6.5 (i.e., mimicking drinking water). To simulate the extreme situations, the concentration of the coexisting anions is set excessively high, with molar concentration

being 1,000 times that of arsenic. In the presence of SO_4^{2-}, CO_3^{2-}, and PO_4^{3-}, As(III) concentration is effectively reduced to < 0.02, < 0.02, and 10 μg L^{-1}, respectively, and As(V) concentration is correspondingly reduced to < 0.02, 22, and 76 μg L^{-1}, respectively. Clearly, the presence of SO_4^{2-} has no appreciable effect on the adsorption of both As(III) and As(V). CO_3^{2-} shows negligible impact on As(III) adsorption but slightly reduces the adsorption of As(V). Its effect on As(V) adsorption may be explained by an increase in pH after its dissolution in the arsenic solution.[32] Though causing only a small reduction in the adsorption of As(III), PO_4^{3-} shows the expected most intense reduction in the adsorption of As(V). PO_4^{3-} is a known strong competing anion for arsenic adsorption and can strongly compete with arsenic for adsorption sites.[26,32,34] Its effect can be explained by the similar tetrahedral structure formed by As(V), As(III), and phosphate.[32] Despite the excessive presence of the coexisting anions, these results confirm that the concentration of more toxic As(III) can be effectively removed with FeO_x-GO-80 to the level (10 μg L^{-1}) meeting the WHO guidelines for drinking water. However, in extreme situations where the drinking water contains large quantities of SO_4^{2-} and PO_4^{3-}, particularly the latter, a higher adsorbent dosage will be required to in order to reduce As(V) concentration to the required level.

3.4 Conclusion

Amorphous iron oxide-GO nanocomposite adsorbents (FeO_x-GO-36, FeO_x-GO-60, FeO_x-GO-80) having different iron oxide content (36, 60, and 80 wt%, respectively) have been synthesized and investigated for arsenic removal. Detailed characterization of

the nanocomposites has been undertaken systematically with TGA, TEM, FTIR, XPS, XRD, and N_2 sorption. In particular, the evidence from XRD and TEM confirms that the iron oxide is primarily in the form of amorphous iron oxide nanoparticles (ca. 5 nm in size), which distribute uniformly in the nanocomposites. The nanocomposite adsorbents show significantly high arsenic adsorption capacities relative to GO and the iron oxide control sample. Increased arsenic adsorption capacities are found with the increase of iron oxide content due to the increase in surface area and the generation of more accessible active sites. In particular, FeO_x-GO-80 shows high q_{max} values of 147 and 113 mg g^{-1} for As(III) and As(V), respectively. Meanwhile, FeO_x-GO-80 has been demonstrated to remarkably reduce the arsenic concentration from 118 (for As(III)) or 108 μg L^{-1} (for As(V)) to < 0.02 μg L^{-1} for both As(III) and As(V). In addition, the kinetic study also confirms the fast uptake of arsenic with FeO_x-GO-80. With the superior performance, this class of FeO_x-GO nanocomposites has high potential for arsenic removal in water treatment given that GO can be produced cost-effectively from abundant natural graphite.

3.5 References

(1) B. K. Mandal and K. T. Suzuki, *Talanta*, 2002, **58**, 201–235.

(2) P. L. Smedley and D. G. Kinniburgh, *Appl. Geochem.*, 2002, **17**, 517–568.

(3) T. S. Y. Choong, T. G. Chuah, Y. Robiah, F. L. G. Koay and I. Azni, *Desalination*, 2007, **217**, 139–166.

(4) D. Mohan and C. U. Pittman Jr., *J. Hazard. Mater.*, 2007, **142**, 1–53.

(5) S. C. N. Tang and I. M. C. Lo, *Water Res.*, 2013, **47**, 2613–2632.

(6) M. L. Pierce and C. B. Moore, *Water Res.*, 1982, **16**, 1247–1253.

(7) K. P. Raven, A. Jain and R. H. Loeppert, *Environ. Sci. Technol.*, 1998, **32**, 344–349.

(8) S. Dixit and J. G. Hering, *Environ. Sci. Technol.*, 2003, **37**, 4182–4189.

(9) S. Luther, N. Borgfeld, J. Kim and J. G. Parsons, *Microchem. J.*, 2012, **101**, 30–36.

(10) S. Yean, L. Cong, C. T. Yavuz, J. T. Mayo, W. W. Yu, A. T. Kan, V. L. Colvin and M. B. Tomson, *J. Mater. Res.*, 2005, **20**, 3255–3264.

(11) C. T. Yavuz, J. T. Mayo, W. W. Yu, A. Prakash, J. C. Falkner, S. Yean, L. Cong, H. J. Shipley, A. Kan, M. Tomson, D. Natelson and V. L. Colvin, *Science*, 2006, **314**, 964–967.

(12) T. Tuutijärvi, J. Lu, M. Sillanpää and G. Chen, *J. Hazard. Mater.*, 2009, **166**, 1415–1420.

(13) L.-S. Zhong, J.-S. Hu, H.-P. Liang, A.-M. Cao, W.-G. Song and L.-J. Wan, *Adv. Mater.*, 2006, **18**, 2426–2431.

(14) F. Mou, J. Guan, Z. Xiao, Z. Sun, W. Shi and X.-A. Fan, *J. Mater. Chem.*, 2011, **21**, 5414–5421.

(15) F. Mou, J. Guan, H. Ma, L. Xu and W. Shi, *ACS Appl. Mater. Interfaces*, 2012, **4**, 3987–3993.

(16) C.-Y. Cao, J. Qu, W.-S. Yan, J.-F. Zhu, Z.-Y. Wu and W.-G. Song, *Langmuir*, 2012, **28**, 4573–4579.

(17) B. Wang, H. Wu, L. Yu, R. Xu, T.-T. Lim and X. W. Lou, *Adv. Mater.*, 2012, **24**, 1111–1116.

(18) T. Wang, L. Zhang, H. Wang, W. Yang, Y. Fu, W. Zhou, W. Yu, K. Xiang, Z. Su, S. Dai and L. Chai, *ACS Appl. Mater. Interfaces*, 2013, **5**, 12449–12459.

(19) Z. Wei, R. Xing, X. Zhang, S. Liu, H. Yu and P. Li, *ACS Appl. Mater. Interfaces*, 2013, **5**, 598–604.

(20) G. K. Das, C. S. Bonifacio, J. De Rojas, K. Liu, K. van Benthem and I. M. Kennedy, *J. Mater. Chem. A.*, 2014, **2**, 12974–12981.

(21) M. Jang, S.-H. Min, T.-H. Kim and J. K. Park, *Environ. Sci. Technol.*, 2006, **40**, 1636–1643.

(22) Z. Gu, J. Fang and B. Deng, *Environ. Sci. Technol.*, 2005, **39**, 3833–3843.

(23) V. Chandra, J. Park, Y. Chun, J. W. Lee, I.-C. Hwang and K. S. Kim, *ACS Nano*, 2010, **4**, 3979–3986.

(24) K. Zhang, V. Dwivedi, C. Chi and J. Wu, *J. Hazard. Mater.*, 2010, **182**, 162–169.

(25) X.-L. Wu, L. Wang, C.-L. Chen, A.-W. Xu and X.-K. Wang, *J. Mater. Chem.*, 2011, **21**, 17353–17359.

(26) G. Sheng, Y. Li, X. Yang, X. Ren, S. Yang, J. Hu and X. Wang, *RSC Adv.*, 2012, **2**, 12400–12407.

(27) J. Zhu, R. Sadu, S. Wei, D. H. Chen, N. Haldolaarachchige, Z. Luo, J. A. Gomes, D. P. Young and Z. Guo, *ECS J. Solid State Sci. Techn.*, 2012, **1**, M1–M5.

(28) J. Zhu, S. Wei, H. Gu, S. B. Rapole, Q. Wang, Z. Luo, N. Haldolaarachchige, D. P. Young and Z. Guo, *Environ. Sci. Technol.*, 2012, **46**, 977–985.

(29) Y. Wang, Q. He, H. Qu, X. Zhang, J. Guo, J. Zhu, G. Zhao, H. A. Colorado, J. Yu, L. Sun, S. Bhana, M. A. Khan, X. Huang, D. P. Young, H. Wang, X. Wang, S. Wei and Z. Guo, *J. Mater. Chem. C*, 2014, **2**, 9478–9488.

(30) G. Gollavelli, C.-C. Chang and Y.-C. Ling, *ACS Sustainable Chem. Eng.*, 2013, **1**, 462–472.

(31) B. Paul, V. Parashar and A. Mishra, *Environ. Sci.: Water Res. Technol.*, 2015, **1**, 77–83.

(32) F. Yu, S. Sun, J. Ma and S. Han, *Phys. Chem. Chem. Phys.*, 2015, **17**, 4388–4397.

(33) J. Ding, B. Li, Y. Liu, X. Yan, S. Zeng, X. Zhang, L. Hou, Q. Cai and J. Zhang, *J. Mater. Chem. A*, 2015, **3**, 832–839.

(34) X. Yu, S. Tong, M. Ge, J. Zuo, C. Cao and W. Song, *J. Mater. Chem. A*, 2013, **1**, 959–965.

(35) Z. Wu, W. Li, P. A. Webley and D. Zhao, *Adv. Mater.*, 2012, **24**, 485–491.

(36) M. Baikousi, A. B. Bourlinos, A. Douvalis, T. Bakas, D. F. Anagnostopoulos, J. Tucek, K. Safarova, R. Zboril and M. A. Karakassides, *Langmuir*, 2012, **28**, 3918–3930.

(37) B. Chen, Z. Zhu, J. Ma, Y. Qiu and J. Chen, *J. Mater. Chem. A*, 2013, **1**, 11355–11367.

(38) J. Yang, H. Zhang, M. Yu, I. Emmanuelawati, J. Zou, Z. Yuan and C. Yu, *Adv. Funct. Mater.*, 2014, **24**, 1354–1363.

(39) H. Chang and H. Wu, *Energy Environ. Sci.*, 2013, **6**, 3483–3507.

(40) J. Zhu, M. Chen, Q. He, L. Shao, S. Wei and Z. Guo, *RSC Adv.*, 2013, **3**, 22790–22824.

(41) K. C. Kemp, H. Seema, M. Saleh, N. H. Le, K. Mahesh, V. Chandra and K. S. Kim, *Nanoscale*, 2013, **5**, 3149–3171.

(42) R. K. Upadhyay, N. Soin and S. S. Roy, *RSC Adv.*, 2014, **4**, 3823–3851.

(43) D. C. Marcano, D. V. Kosynkin, J. M. Berlin, A. Sinitskii, Z. Sun, A. Slesarev, L. B. Alemany, W. Lu and J. M. Tour, *ACS Nano*, 2010, **4**, 4806–4814.

(44) W. S. Hummers and R. E. Offeman, *J. Am. Chem. Soc.*, 1958, **80**, 1339.

(45) C. P. Huang and L. M. *J.* Vane, *Water Pollut. Control Fed.*, 1989, **61**, 1596–1603.

(46) S. Stankovich, D. A. Dikin, R. D. Piner, K. A. Kohlhaas, A. Kleinhammes, Y. Jia, Y. Wu, S. T. Nguyen and R. S. Ruoff, *Carbon*, 2007, **45**, 1558–1565.

(47) W. Zhang, X. Shi, Y. Zhang, W. Gu, B. Li and Y. Xian, *J. Mater. Chem. A*, 2013, **1**, 1745–1753.

(48) S. Park, J. An, I. Jung, R. D. Piner, S. J. An, X. Li, A. Velamakanni and R. S. Ruoff, *Nano Lett.*, 2009, **9**, 1593–1597.

(49) H. Kong, J. Song and J. Jang, *Chem. Commun.*, 2010, **46**, 6735–6737.

(50) G. Bhargava, I. Gouzman, C. M. Chun, T. A. Ramanarayanan and S. L. Bernasek, *Appl. Surface Sci.*, 2007, **253**, 4322–4329.

(51) L. Xu, J.-W. McGraw, F. Gao, M. Grundy, Z. Ye, Z. Gu and J. L. Shepherd, *J. Phys. Chem. C*, 2013, **117**, 10730–10742.

(52) K. S. W. Sing, D. H. Everett, R. A. W. Haul, L. Moscou, R. A. Pierotti, J. Rouquerol and T. Siemieniewska, *Pure Appl. Chem.*, 1985, **57**, 603–619.

(53) World Health Organization, *Guidelines for Drinking Water Quality*, 2011.

(54) Y. S. Ho and G. Mckay, *Water Res.*, 2000, **34**, 735–742.

3.6 Supporting Information

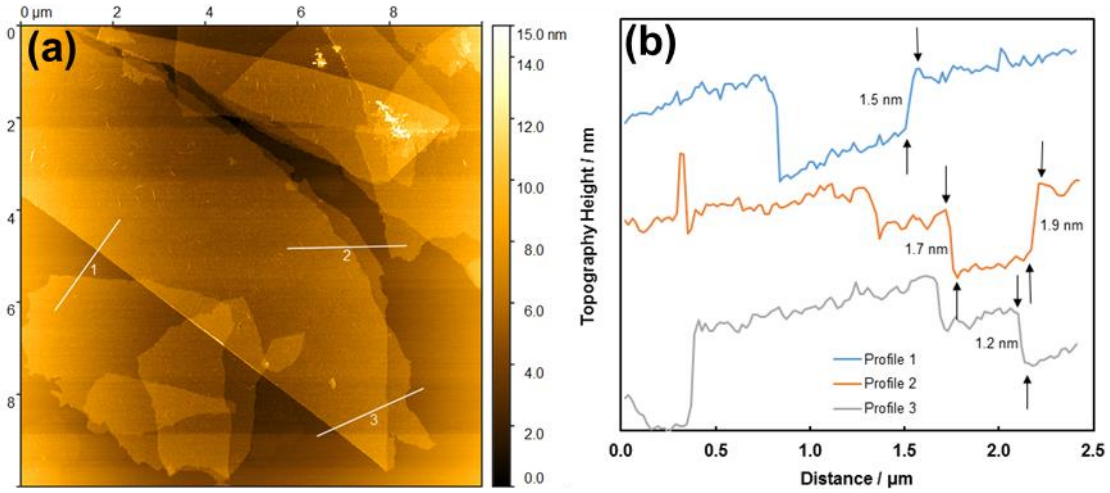

Figure S3.1 (a) AFM height image of GO; (b) height profiles across three profiles denoted in (a).

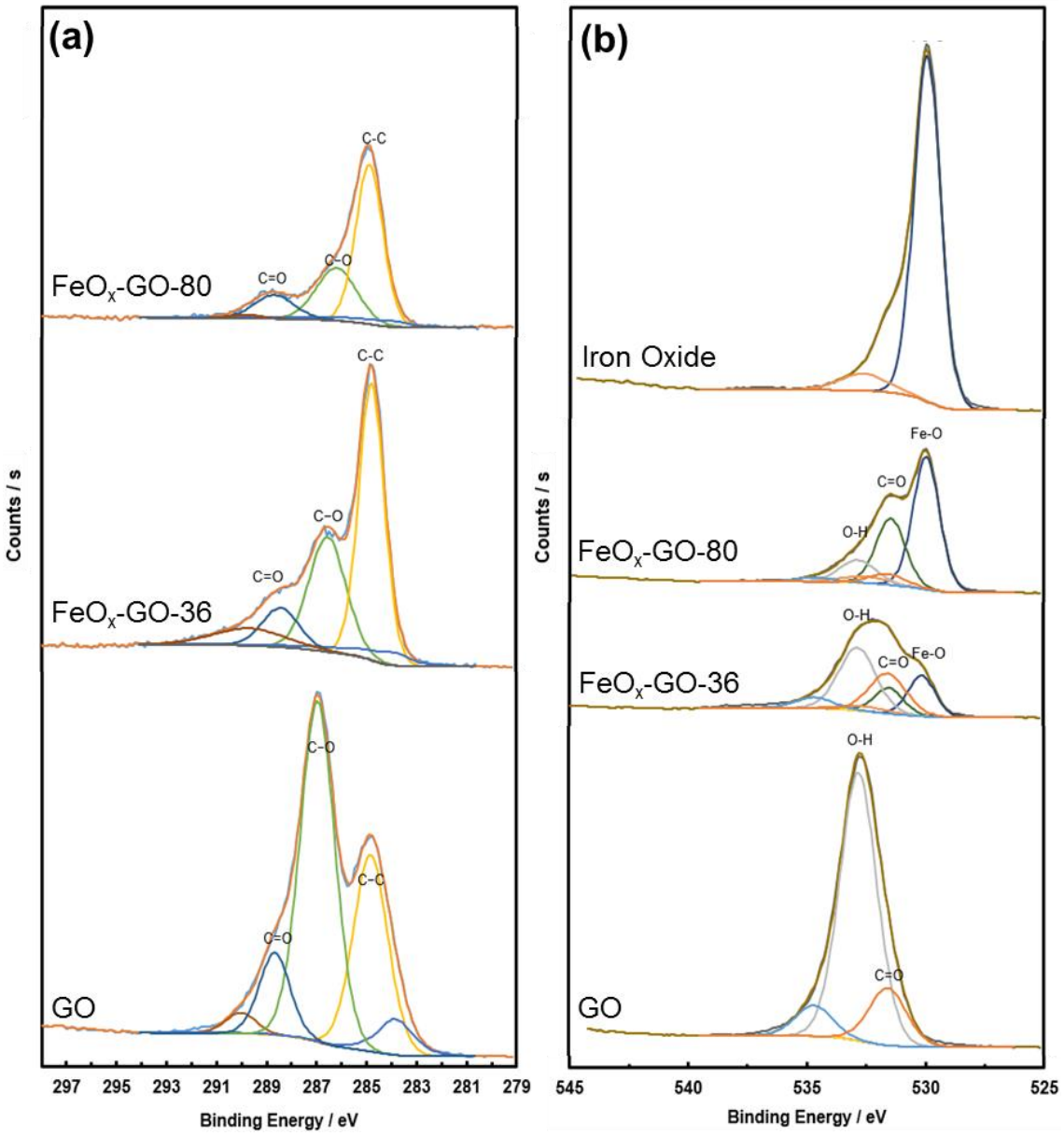

Figure S3.2. The C_{1s} (a) and O_{1s} (b) scan results of GO, FeO_x-GO-36, FeO_x-GO-80 and the iron oxide control sample.

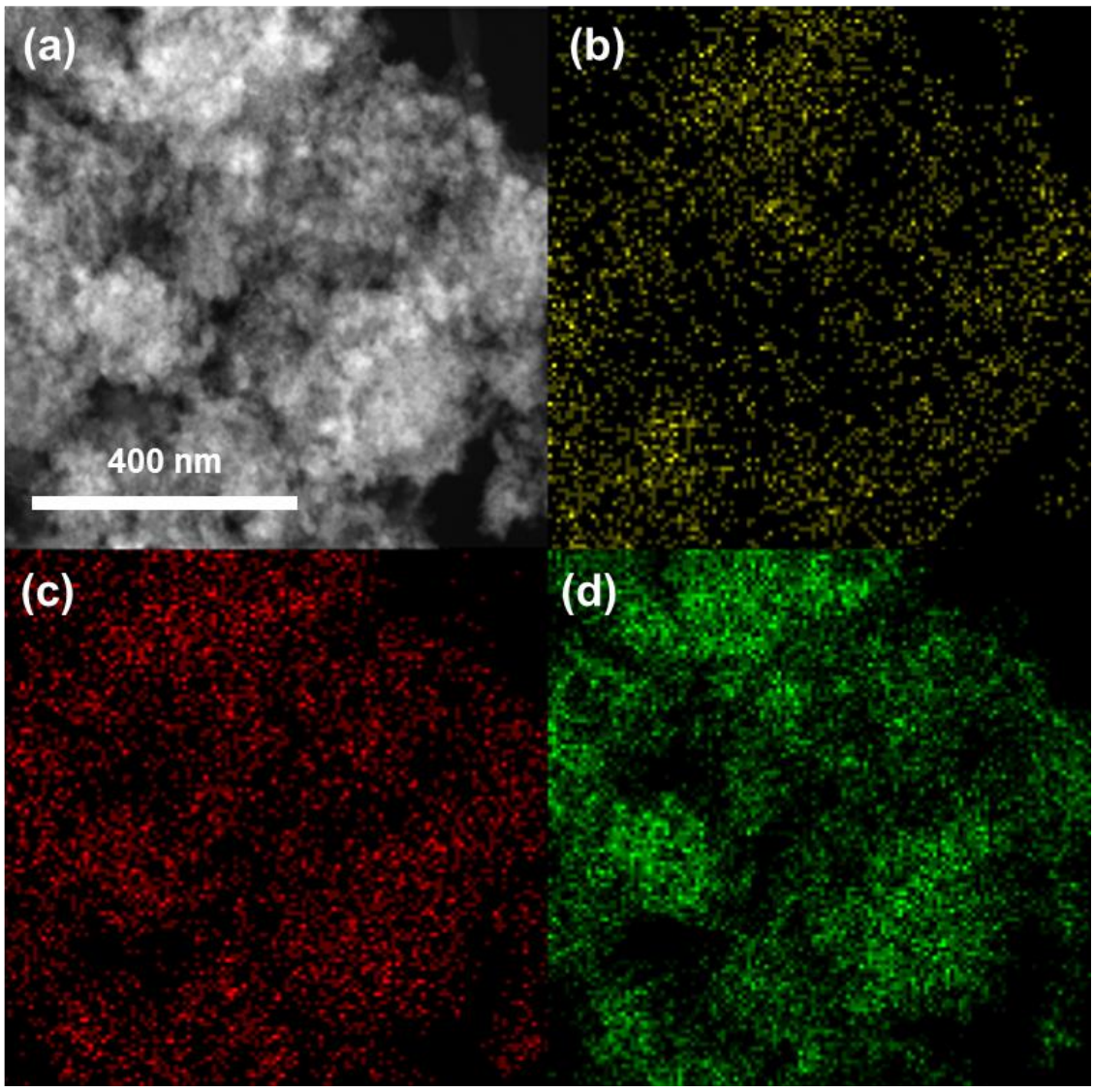

Figure S3.3. DF-STEM image (a) and the corresponding C (b), O (c), and Fe (d) elemental maps of FeO_x-GO-80.

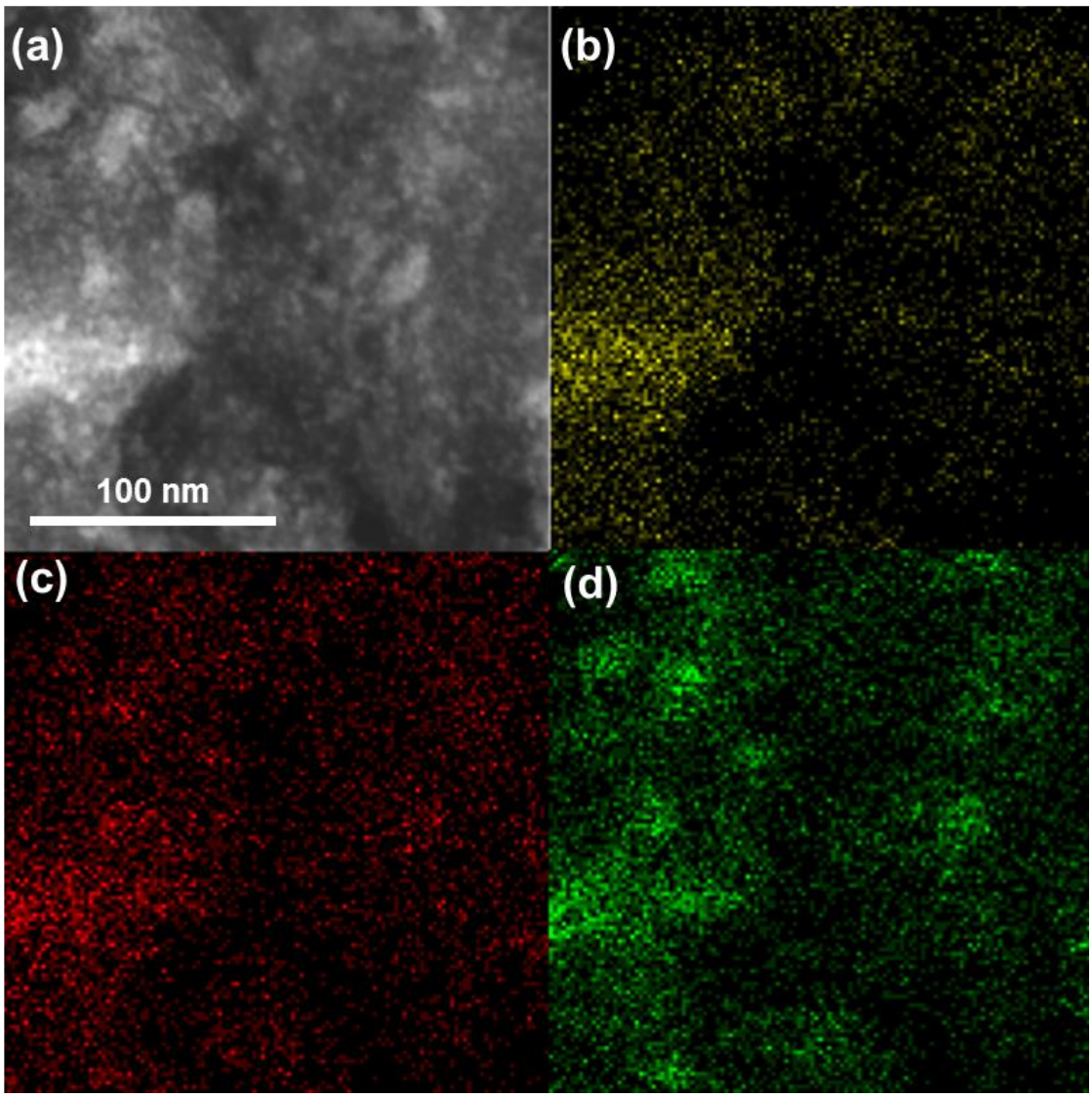

Figure S3.4. DF-STEM image (a) and the corresponding C (b) O (c) and Fe (d) elemental maps of FeO_x-GO-36.

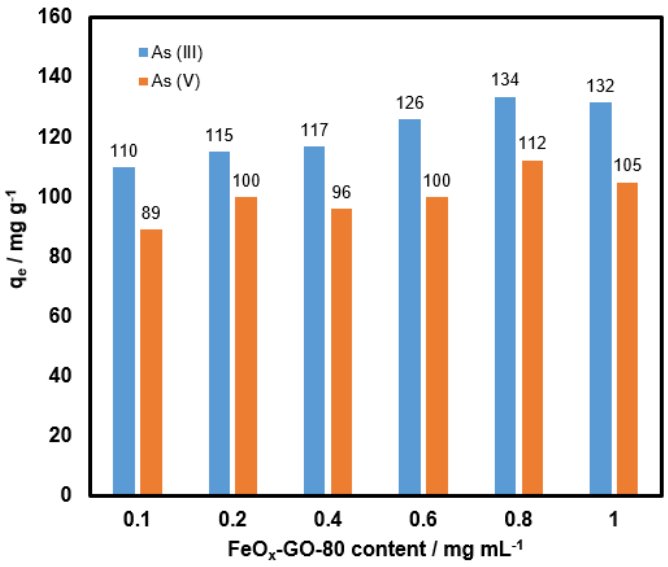

Figure S3.5. Arsenic adsorption with FeO_x-GO-80 at different dosages (0.1–1 mg mL^{-1}). Initial arsenic concentration: 1200 and 350 mg L^{-1} for As(III) (at pH = 7) and As(V) (at pH = 3), respectively.

Table S3.1. A summary of the fitting parameters of arsenic adsorption isotherms and kinetics with FeO_x-GOs, GO, and the iron oxide control sample.

Samples	Langmuir model			Pseudo-second-order kinetic model			
As(III)	R^2	q_{max} (mg g^{-1})	b (L mg^{-1})	R^2	k_2 (g mg^{-1} min^{-1})	V_0 (mg g^{-1} min^{-1})	q_{eq} (mg g^{-1})
GO	0.983	19	0.001				
FeO_x-GO-36	0.993	90	0.005				
FeO_x-GO-60	0.994	132	0.005				
FeO_x-GO-80	0.991	147	0.011	1.000	0.001	11.3	110
Iron oxide	0.987	110	0.003				

Samples	Langmuir model			Pseudo-second-order kinetic model			
As(V)	R^2	q_{max} (mg g^{-1})	b (L mg^{-1})	R^2	k_2 (g mg^{-1} min^{-1})	V_0 (mg g^{-1} min^{-1})	q_{eq} (mg g^{-1})
GO	0.989	28	0.003				
FeO_x-GO-36	0.991	59	0.208				
FeO_x-GO-60	0.981	80	0.098				
FeO_x-GO-80	0.994	113	0.295	1.000	0.001	7.4	114
Iron oxide	0.981	65	0.097				

Chapter 4: Conclusions and Outlooks

This thesis presents the synthesis and characterization of two sets of iron oxide-containing nanocomposites (i.e., FeO_x-CNS and FeO_x-GO sets) as efficient arsenic adsorbents. Two different carbon nanomaterials, i.e., CNS and GO, were employed as the matrices for the loading of the iron oxide. A systematic investigation on their performance for arsenic adsorption and the dependencies on their structural parameters has been undertaken.

In the set of FeO_x-CNS nanocomposites, FeO_x-CNS-13 having the iron oxide content of 13 wt% shows the highest arsenic adsorption capacities, 416 mg g^{-1} for As(III) and 201 mg g^{-1} for As(V), which are comparable to or even higher than the best values reported in the literature. Reducing or increasing the iron oxide content leads to reduced arsenic adsorption capacities. The uniform dispersion of the active iron oxide species on the CNS matrix with the maximized adsorption sites is believed to be the reason leading to the best adsorption performance at this iron oxide content.

In the set of FeO_x-GO nanocomposites, increasing iron oxide content is found to lead to enhanced arsenic adsorption capacities, with FeO_x-GO-80 showing the highest capacities of 147 mg g^{-1} for As(III) and 113 mg g^{-1} for As(V). These capacity data are among the highest reported to date with iron oxide-GO nanocomposite adsorbents. The increasing surface area and pore volume as well as the narrowed mesopores with the

increase of iron oxide content are reasoned to maximize the active sites for arsenic adsorption.

With their superior performance, the two sets of nanocomposite adsorbents designed and synthesized in this thesis research may have potential for industrial applications for arsenic adsorption from wastewater streams. Meanwhile, the fundamental results obtained in this thesis research may also benefit the future research in the design of the new adsorbents of improved performance for arsenic adsorption.

Based on this thesis research, further exploration into arsenic adsorption in the presence of other metals and anions could provide better understanding of the effects of coexisting anions and metals on the adsorption performance. Meanwhile, the further study the arsenic removal in real wastewater and groundwater systems, which are more complicated systems with abundant metals and anions, is also important prior to their commercial applications. In addition, the FeO_x-CNS and FeO_x-GO nanocomposite adsorbents can also be used potentially on removal of heavy metals (such as Pb, Cu, Hg, Co, and Cr, etc.), anions and organic pollutants. Besides the CNS and GO matrices, nanocomposites based on other economic matrices, such as FeO_x-cellulose, are also interesting for industrial usage.